A multi-faceted approach to characterize acid-sulfate alteration processes in volcanic hydrothermal systems on Earth and Mars

by

Emma Cordts Marcucci

B.S., Johns Hopkins University, 2008

A thesis submitted to the

Faculty of the Graduate School of the

University of Colorado in partial fulfillment

of the requirement for the degree of

Doctor of Philosophy

Department of Geological Sciences

2013

This thesis entitled:
A multi-faceted approach to characterize acid-sulfate alteration processes in volcanic hydrothermal systems on Earth and Mars
written by Emma Cordts Marcucci
has been approved for the Department of Geological Sciences

_____

Dr. Brian M. Hynek

_____

Dr. Lang Farmer

_____

Dr. Tom McCollom

_____

Dr. Alexis Templeton

_____

Dr. Steve Schmidt

Date: _____

The final copy of this thesis has been examined by the signatories, and we find that both the content and the form meet acceptable presentation standards of scholarly work in the above mentioned discipline.

Marcucci, Emma Cordts (Ph.D., Geological Sciences)

A multi-faceted approach to characterize acid-sulfate alteration processes in volcanic hydrothermal systems on Earth and Mars

Thesis directed by Associate Professor Brian M. Hynek

Abstract

Acid-sulfate alteration is a dominant weathering process in high temperature, low pH, sulfur-rich volcanic environments. Additionally, hydrothermal environments have been proposed as locations where life could have originated on Earth. Based on the extensive evidence of flowing surface water and persistent volcanism, similar locations and processes could have existed on early Mars. Globally observed alteration mineral assemblages likely represent relic Martian hydrothermal settings. Yet the limited understanding of environmental controls, limits the confidence of interpreting the paleoconditions of these hydrothermal systems and assessing their habitability to support microbial life. This thesis presents a series of laboratory experiments, geochemical models, analog fieldwork, and Martian remote sensing to characterize distinguishing features and controls of acid-sulfate alteration. The experiments and models were designed to replicate alteration is a highly acidic, sulfurous, and hot field sites. The basaltic minerals were individually reacted in both experimental and model simulations with varying initial parameters to infer the geochemical pathways of acid-sulfate alteration on Earth and Mars. It was found that for a specific starting material, secondary mineralogies were consistent. Variations in pH, temperature and duration affected the abundance, shape, and size of mineral products. Additionally evaporation played a key role in secondary deposits; therefore, both alteration and evaporitic processes need to be taken into consideration. Analog volcanic sites in Nicaragua were used to supplement this work and highlight differences between natural

and simulated alteration. *In situ* visible near-infrared spectroscopy demonstrated that primary lithology and gas chemistry were dominant controls of alteration, with secondary effects from environmental controls, such as temperature and pH. The spectroscopic research from the field was directly related to Mars observations in Noctis Labyrinthus, Terra Sirenum, Syrtis Major, and Mawrth Vallis to help interpret ancient conditions in those settings. To further apply the results from experiments, models, and fieldwork, Coprates Chasma in eastern Valles Marineris was studied using mineralogical and morphological data. Emplacement of alteration minerals indicated both pre- and post-rifting hydrothermal activity. Smaller southern grabens appeared to have experienced a unique alteration. In summary, this dissertation presents research that contributes to the understanding of the geological evolution of Mars and potentially habitability.

Acknowledgements

I would most like to thank my advisor, Brian Hynek, for his guidance through this project and his patience reading and re-reading many drafts of my articles. I would also like to thank Tom McCollom for use of his laboratory for experimental work and advice on geochemical modeling. The fieldwork component of this research would not have been possible without the in-country assistance of INETER and the spectral interpretation help from Kathryn Young and Mikki Osterloo. I would also like to thank Karyn Rogers for introducing me to field techniques for biological samples. Chapters 2-5 have been or will be submitted for publication in scientific journals and have benefitted greatly from: Brian Hynek, Tom McCollom, Mikki Osterloo, Stuart Robbins, Karyn Rogers, and Kathryn Young. A number of friends and family provided insightful comments on the introduction of this these, including Barbara Cordts, Grace Cordts, Elizabeth Frank, Ulyana Horodyskyj, Kristin Lucas, Andrea Marcucci, Dan Marcucci, Olivia Marcucci, Macy Marcucci, Michael O'Keefe, Mikki Osterloo, Ernesto Perez, Stuart Robbins, and Nadine Semer. Finally, I would like to thank my family and friends, the wonderful actors and technical crew of Centerstage Theater Company and the instructors at FAC for helping me remain sane and healthy through the intense process to obtain a Ph.D.

The science chapters 2-4 presented in this thesis have been submitted or will soon be submitted to journals. Acknowledgements for each section follow:

Chapter 2: We would like to acknowledge the Laboratory for Environmental and Geological Studies (LEGS) at the University of Colorado at Boulder's (UCB) Department of Geological Sciences for completing the fluid analysis. The XRD instrument used is also at UCB's Department of Geological Sciences. The SEM/EDS instrument is housed at the Nanomaterials Characterization Facility on the UCB campus. Additionally, we thank the

Nicaraguan government agency Instituto Nicaragüense de Estudios Territoriales for logistical support in Nicaragua. This work was supported by NASA NESSF Grant # NNX10AU39H. Thank you to T. McCollom for insight comments on experiment and model design and analysis, as well as, use of laboratory space and manuscript edits. Many thanks to M. Osterloo, S. Robbins, and D. Marcucci for editorial comments that greatly improved this manuscript.

Chapter 3: We would like to thank Analytical Spectral Devices, Inc. in Boulder, CO for the use of the TerraSpec4 instrument used during this field campaign, particularly those individuals who worked hard to facilitate the loan and training in a limited timeframe. Additionally, we thank the Nicaraguan government agency Instituto Nicaragüense de Estudios Territoriales for in country support of this study. Thanks to Mikki Osterloo for useful discussions regarding this manuscript. This work was supported by NASA NESSF Award #NNX10AU39H, the CU Department of Geological Sciences Longley-Wahlstrom-Werner Graduate Research Award, and NASA Exobiology Award #NNX08AQ11G and NASA Early Career Award #NNX12AF20G to B. M. Hynek.

Chapter 4: We would like to thank Kathryn Kierein-Young for the custom ENVI/IDL spectra clean program and support in CRISM analyses. We would like to thank Mikki Osterloo for assistance with the analysis of THEMIS spectral data. We thank the CRISM, THEMIS, HiRISE, and CTX teams for the acquisition of data used in this study. This work was supported by NASA NESSF Grant # NNX10AU39H.

Table of Contents

List of Tables

List of Figures

unless otherwise stated. Library spectra are scaled to match the general reflectance levels of field spectra by a simple linear multiple, for example 0.5. This does not change the spectral shape, but lowers the absolute reflectance of the library spectra for easier comparison to field samples. (A) Gypsum (Gypsum HS333.3B) is identified in a white deposit from the 'Monkey Face' feature in Figure 7. Gypsum is often identified by itself. (B) Example of an iron mineral, hematite (Hematite GDS27) measured as a rock coating on 'Gorilla Head' with additional hydration from hydrated silica (Siliceous Sinter BKR1JB329C). (C) Spectrum from the cave in Figure 7 that is dominated by gypsum, but also contains a band at 0.43 μm, normally indicative of Fe^{3+} in the jarosite mineral family (Jarosite JR2501K), but it lacks longer wavelengths features. This could be from mixing of several phases, such that a small amount of a jarosite family mineral is masked by gypsum. This feature may also be from an Fe-rich natroalunite (see text for details). (D) Spectra of hexahydrite (Hexahydrite LASF56A), an evaporitic mineral, for a drainage site in the topographic lows of Figure 7. (E) Goethite (USGS Goethite WS220) and silica signals match the spectrum from the orange portion of this highly altered rock. (F) Spectrum from the brown portion of 'Gorilla Head' in B with goethite (USGS Goethite WS219) and kaolinite+smectite (USGS Kaolin/Smect506 95%K). 48

Figure 12. Example field spectra for Momotombo volcano. Library spectra are scaled to match the general reflectance levels of field spectra as described in Figure 11. (A) Example of a bright yellow deposit showing sulfur (USGS Sulfur GDS94 Reagent) and hydrated silica from a float crystal in Figure 8. (B) An example of pure hydrated silica in a rock with several layers of weathering (right panel in Figure 8). (C) Red clay material identified as hematite and kaolinite (USGS Kaolinite CM7), with additional hydrated silica in a soil formation. (D) Weathering rind, which contains gypsum and goethite (USGS Goethite WS220), example of when gypsum is not found alone (right panel of Figure 8). (E) Red clay area with a mixture of kaolinite+smectite, hematite, and a member of the alunite family (USGS Alunite GDS82 Na82) minerals. (F) Lowest exposed surface of a large weathered rock (same at D) with alunite and goethite. 50

Figure 13. Example field spectra from Telica volcano. Library spectra are scaled to match the general reflectance levels of field spectra as described in Figure 11. The jarosite and alunite spectra presented here may be Fe-rich natroalunite and natroalunite for reasons discussed in text. (A) Jarosite detection from the edge of the crater (right panel Figure 9). (B) Combination of jarosite and alunite family members, which are in the same mineral family from a float rock. (C) Goethite and alunite in an orange deposit near the crater rim (left panel Figure 9). (D) White surface deposit on a float rock measured as hydrated silica. (E) Goethite and alunite in a brown rim deposit near C. (F) Hematite and kaolinite+smectite identification from the surface of a red float rock. 52

Figure 14. Example field spectra from the San Jacinto Mudpots on the flank of Telica volcano. Library spectra are scaled to match the general reflectance levels of field spectra as described in Figure 11. (A) Possible match to pickeringite (CRISM Pickeringite LASF54A), with additional hydrated silica from the white deposits of an area with rings of color alteration (top right panel Figure 10). (B) Identification of the brown material for the same location is a mixture of montmorillonite (USGS Montmorillonite SAz-1), saponite (USGS SapCa-1.AcB) with hydrated silica. (C) Detection of jarosite (or potentially Fe-rich natroalunite, see text), slightly depressed by mixing with hydrated silica in a yellow deposit (bottom left panel Figure 10). (D) Combination of kaolinite+smectite clay, hematite, and hydrated silica to explain the spectra of a

1. Introduction

1.1 Historical Observations

Mars, named after the Roman god of war, has fascinated humans since early Egyptian astronomers watched it travel across the night sky. For millennia, stargazers contemplated the idea that the red planet could be Earth-like enough to host life. During the 19th century the rapidly advancing field of optics made the first detailed studies of the Martian surface possible. From this came the first speculations that water may have flowed on Mars. In 1877 Giovanni Schiaparelli observed his *canali*, (literally Italian for "channels" but often mistranslated to "canals") [*Manara and Trinchieri*, 2011]. Additionally, periodic changes in Mars' surface brightness were interpreted by some to be agricultural seasons. The concept of agriculture coupled with connotation provided by Schiaparelli's "canals" perpetuated the avid belief that there was or had been intelligent civilization on Mars. Indeed, Percival Lowell, founder of Lowell Observatory, believed this story until death in 1916 [*Manara and Trinchieri*, 2011]. In reality, the Schiaparelli *canali* features were likely optical illusions from the inferior telescopes of the day or enhanced albedo (reflected surface brightness) differences caused by dust storms on the Martian surface. Nevertheless, Mars remained a place of mystery and intrigue.

It is only in the past several decades that detailed study has decoded this captivating planet. Due to its proximity to earth, Mars is a relativity easy mission destination. With the advent of space travel, the results of scientific missions transformed the image of Martian life from an intelligent civilization to a microbial world. The first landed mission to Mars, *Viking 1* and *2*, whose explicit goals were to assess whether life existed on Mars, did not find conclusive evidence of life but presented chemically interesting information about the planet for the first time. When missions returned to the planet two decades later, technological advancements and

new instruments provided novel insights into Martian chemistry, thus, the focus of study shifted again.

Recent studies have shown that conditions on Mars are extremely cold, with an average temperature of -63°C and a very thin atmosphere that is about 0.6% of Earth's (in terms of surface pressure), composed primarily of carbon dioxide (~95%). These conditions make stable liquid water impossible on the surface contributing to the cold climate and dryness of present-day Mars. However, numerous morphological and mineralogical features of the Martian surface are best explained by widespread, flowing water in the distant past. These morphological indicators of sustained water drive a debate on early Mars climate [e.g. *Haberle*, 1998]. Some believe that Mars always had a thin atmosphere that resulted in cold and dry surface conditions much like the present-day [*Kasting*, 1991]. Others argue that the atmosphere was once capable of sustaining a warm, wet planet, but has since been lost [*Craddock and Howard*, 2002]. The water-related features on Mars support the latter atmospheric hypothesis. Mars is now a place of particular interest to those who study the origin of life and/or life on other planets because it may have been habitable before Earth early in solar system history [*Nisbet and Sleep*, 2001].

Much recent research has been guided by the principle: "follow the water". In particular, many scientists are focused on the idea that life originated in a hydrothermal volcanic environment, where fresh rock interacts with high-temperature water, combining heat, chemical elements, water, and energy needed for the existence of life. There is ample evidence that at the time when Mars had active volcanoes it also hosted a milder environment and liquid surface water, such as valley networks. The work presented in this dissertation focuses on characterizing mineral deposits of hydrothermal areas with a focus on high-temperature, low pH, sulfur-rich

volcanic zones. The results of this work will aid in the identification of potential hydrothermal areas active in the past on Mars.

This dissertation delves into this particular water-rock interaction. The goal of this body of work is to increase understanding of the following questions: What minerals comprise the secondary mineral assemblages in a volcanic environment? Are there characteristics of volcanic, hydrothermal alteration that distinguish it from other acid-sulfate weathering environments? How may such environments be identified on Mars? Answering such questions helps interpret the geological evolution of Mars; however, before explaining the details of this dissertation, it is crucial to have a context of water and volcanism on Mars.

In the following sections, I will briefly outline the mission data relevant to this study of Mars and summarize the global trends for context (Section 1.2). I will then describe the evidence for water on Mars in detail in terms of morphological and then mineralogical aspects (Sections 1.3 and 1.4). Within the morphological section (5 subsections), I will first introduce the evidence for ancient surface water on Mars based on orbiter data and the implications of these features for climate (Section 1.3.1). The next subsection will discuss the orbital evidence of water retreating to the subsurface, or evidence for ancient subsurface water (Section 1.3.2), then the orbital evidence of transient modern water (Section 1.3.3). After discussing the global features of water from orbiter data, I will describe the water-related findings of the Martian landers (Section 1.3.4). The last subsection will briefly mention the observations of modern ground ice (Section 1.3.5).

After presenting the morphological data, I will discuss the chemical and mineralogical evidence of water (4 subsections), subdivided by mineral type: iron minerals (Section 1.4.1), phyllosilicates (clay) (Section 1.4.2), salts (sulfates and chlorides) (Section 1.4.3), and hydrated

silica (Section 1.4.4). Concurrent with the presence of water on Mars was active volcanism. Thus, the types and history of volcanoes on Mars will be the focus of the next section (Section 1.5). With an understanding of water and volcanism on Mars, I will introduce the interacting nature of these two in hydrothermal systems (Section 1.6). These systems produce heavily altered rock with a variety of sulfates, along with some clays, iron minerals, and silica. My dissertation focuses on these volcanic, hydrothermal interactions and will be outlined in the last section of this chapter (Section 1.7).

1.2 Spacecraft Exploration

Ever advancing instrument technique has provided new volumes of data with which to explore the properties and features of Mars. In 1971, *Mariner 9* went into orbit around Mars and returned detailed images of the Martian surface that challenged the concept of a persistent cold, dry climate on ancient Mars [*Masursky*, 1973; *Baker*, 2001]. Most images had a pixel scale of 1-3 kilometers showing large-scale features of the surface, but numerous others had a resolution of several hundred meters showing many surface water features. The *Viking* missions in 1975-80 had orbiting cameras with a pixel size of about 100 meters [*Carr et al.*, 1976]. They also took the first images with landers from the surface. The missions that took place over the next few decades, including *Mars Global Surveyor* (1999-2006), *Mars Odyssey* (*MO*) (2001-present), and *Mars Reconnaissance Orbiter* (2006-present), use(d) imaging technology that had improved dramatically. The *Mars Global Surveyor* (*MGS*) had both the Mars Orbiter Camera (MOC) [*Malin and Edgett*, 2001] and Mars Orbiter Laser Altimeter (MOLA) [*Smith et al.*, 2001]. The combined morphology and topography information added details to surface maps never previously observed. By the mid-2000s, the *Mars Reconnaissance Orbiter* (*MRO*) cameras, the High Resolution Imaging Science Experiment (HiRISE) and the Context Camera (CTX), gave an

unprecedented view of the Martian surface. As implied by the name, CTX takes larger-scale images at pixel scales of ~5.5 meters to provide context for the detailed work of other *MRO* instruments [*Malin et al.*, 2007]. HiRISE takes pictures of the surface with a resolution of 0.25 to 1.3 meters per pixel [*McEwen et al.*, 2007]. Over time, advances in technology have allowed detailed study of water-related features that cover sizes ranging from centimeter-scale textures [e.g. *Squyres et al.*, 2006b, 2007] to valley networks and sinuous channels spanning thousands of kilometers long [e.g. *Hoke and Hynek*, 2009; *Hynek et al.*, 2010].

Mineralogical and chemical evidence complements morphological evidence to support the hypothesis of water on Mars. Chemical data has been analyzed on Mars since the *Viking* landers. This mission tested soil and rock chemistry and detected mineralogy in discrete locales by performing the first ever chemical experiments of the Martian surface [e.g. *Binder et al.*, 1977; *Mutch et al.*, 1977; *Clark et al.*, 1982]. The results of these experiments showed that Mars has a diverse chemistry. Further evidence was gathered by one of the most scientifically productive missions to Mars, the *Mars Exploration Rovers*. Originally scheduled for a 90-day mission, one rover is still in operation almost 10 years later and the second only recently stopped working. The pair of rovers, *Opportunity* and *Spirit*, bounced to a stop in Meridiani Planum and Gusev crater, respectively. The landing sites were chosen for the evidence of liquid water activity observed in previous missions. Meridiani Planum was chosen for mineralogical water evidence [*Arvidson et al.*, 2003] and Gusev for morphological evidence of water [*Cabrol et al.*, 2003]. A variety of instruments capable of determining elemental composition of soil and rock were used. Chemical trends could be correlated to suggest certain minerals.

Direct detection of global mineralogy on Mars is a more recent discovery as technical developments have increased the miniaturization and portability of instruments that could be

used for missions. The most recent orbiters (*MGS, MO*, *MRO*) have detected numerous deposits of minerals associated with aqueous alteration across the planet [e.g. *Gendrin et al.*, 2005; *Bibring et al.*, 2006; *Ehlmann et al.*, 2009a; *Murchie et al.*, 2009a]. *Mars Global Surveyor* was the first mission to Mars after the almost two-decade hiatus between 1980 and 1998 and the first with an instrument that could measure mineralogy. The Thermal Emission Spectrometer (TES) measured thermal infrared (6-50 μm) wavelengths of the light spectrum to identify mineralogy [*Christensen et al.*, 2001]. The Thermal Emission Imaging System (THEMIS) on Mars Odyssey had both visible wavelength and thermal infrared capabilities [*Christensen et al.*, 2003]. Such data can be used to produce images of the surface and collect spectral data for mineralogical and soil property analyses.

The most recent orbiter missions to Mars are the European Space Agency's *Mars Express* and NASA's *Mars Reconnaissance Orbiter*, both of which have spectrometers that measure reflected light in a wavelength range important for identifying minerals [e.g. *Gendrin et al.*, 2005; *Bibring et al.*, 2006; *Bishop et al.*, 2009; *Ehlmann et al.*, 2009, 2011; *Murchie et al.*, 2009; *Wray et al.*, 2009]. Characteristic reflectance patterns can be used to identify minerals, although sometimes spectra are not unique to a single mineral. The *Mars Express* instrument OMEGA (Observatoire pour la Minéralogie, l'Eau, les Glaces et l'Activité) arrived at Mars at the end of 2003 and has mapped the surface at a scale ranging from 300 meters to 4.8 kilometers per pixel [*Bibring et al.*, 2006; *Poulet et al.*, 2007]. The *MRO* instrument, Compact Reconnaissance Imaging Spectrometer for Mars (CRISM), arrived in 2006 and improved the resolution of surface mineral detections. The global mapping mode has a 200 meter pixel scale with approximately 20 meter pixels for targeted locations [*Murchie et al.*, 2009b]. Guided by larger-scale OMEGA data and interesting morphological features in imagery data, CRISM has taken targeted measurements

across the planet, including craters, deep canyons, and varied terrain types. Minerals in these areas were similar to the mineral classes from OMEGA, but the higher resolution showed more complex relationships and distinction of unique minerals from which more detailed formation environments may be inferred. These orbiting instruments have shown and increasingly diverse planet in terms of morphological and mineralogic water features.

1.2.1 Brief History of Water and Alteration Environments

Both morphological and mineralogical data suggest how water on Mars changed over time (Figure 1). Morphology shows that water flowed over the surface in large quantities for sustained periods of times (discussed in detail below) and that the atmosphere was thick enough to support large bodies of liquid water and surface flow [e.g. *Craddock and Howard*, 2002]. Over time, water was sequestered underground and frozen, though it occasionally erupted to the surface in large catastrophic floods. Currently, the surface is dry enough that only transient small flows of water occur periodically.

Detailed understanding of the mineral layers and relative ages is also a means to hypothesize past conditions on Mars. OMEGA scientists used mineral detections and relationships to suggest three dominant mineral forming environments on Mars [*Bibring et al.*, 2006] (Figure 1). Some of the oldest minerals on Mars are proposed to be phyllosilicates, or clays, that formed in aqueous environments early in the planet's history when it was still cooling and had more persistent surface water. As Mars lost water, the planet became arid and the remaining water became more acidic, forming mainly sulfates. Today, due to an oxidizing atmosphere, iron oxides are the main alteration mineral.

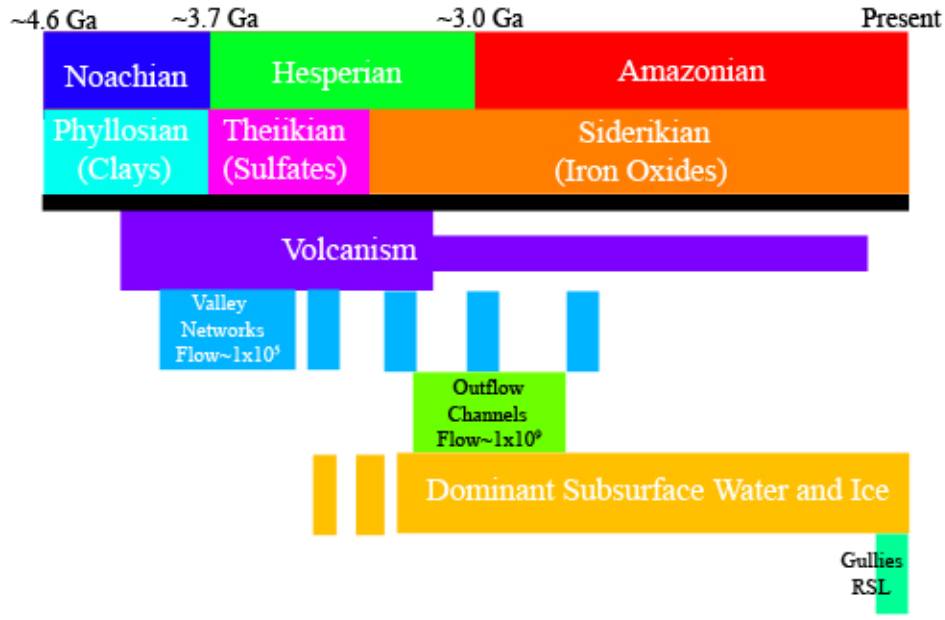

Figure 1. Timeline of Mars history. The first row lists the geological periods on Mars. The second row lists the dominant alteration environments. Boxes below the black line show the approximate periods of volcanic and water-related activity relevant to this dissertation. The period of valley networks is also the time of paleolake and delta formation. The average flow values are the average peak discharge in meters cubed per second (m^3/s) of these outflows. Adapted from [*Ehlmann et al.*, 2011b] with [*Baker*, 2001; *Bibring et al.*, 2006; *Hoke et al.*, 2011; *Robbins et al.*, 2011].

The traditional mineral sequence based on decreasing water content and increasing acidity and oxidation state (i.e., from oldest to youngest), should be Fe/Mg-clays, Al-clays, sulfates, and then iron oxides. However, CRISM's highly detailed data gave an unprecedented view of Martian mineralogy and established that mineral relationships were more complicated than phyllosilicate-sulfate-iron oxide. For example, studies have shown areas of inversion with sulfates as the oldest unit, such as in northern Meridiani Planum and Noctis Labyrinthus (Figure 2) [*Anderson and Bell*, 2008; *Wray et al.*, 2010; *Weitz et al.*, 2011; *Thollot et al.*, 2012]. The CRISM images for mineral identifications are often correlated to HiRISE pictures that reveal textures and morphologies of individual rock units. The complex relationship of mineralogies suggests that Mars had an intricate climate as well as localized geological activity.

Figure 2. Inverted sequence of CRISM–detected minerals, where sulfates appear to be older than phyllosilicates [*Wray et al.*, 2010].

1.3 Morphological Evidence

1.3.1 Orbital Evidence for Ancient Surface Water

When viewed from orbit, Earth's river systems resemble long winding channels or branched networks of smaller systems. Martian research suggests that the previously branched systems will merge and form larger channels that are typical of river systems on Earth. On Earth, these systems are strongly influenced by precipitation, and the morphological features of channels on Mars suggest a similar formation mechanism [*Masursky*, 1973; *Hoke and Hynek*,

2009]. Such systems on Earth are called river valleys, however, the Martian systems are called "valley networks," following the standard guidelines to name features without any formation implications (i.e., "river valleys" would clearly imply that flowing water created them). Valley networks are widespread on Mars, and most are 3.5-3.8 billion years old [*Fassett and Head III*, 2008a; *Hoke and Hynek*, 2009] (Figure 1). The atmosphere of present-day Mars is too thin to support this kind of extensive surface flow of water, so the networks are evidence that the early Martian climate was much different. Moreover, the determined ages of valley networks suggests that, over the course of Mars's history, different areas of the planet experienced precipitation at different times [*Hoke and Hynek*, 2009]. Thus, Mars appears to have had an active and complex hydrological cycle in its past. Should this widespread and stable water have occurred on Mars, it would have been beneficial to the origin and survival of life.

High volumes of rain and surface runoff water erode the ground, forming many small channels that grow in width and depth downstream. An alternative formation mechanism is the release of groundwater that continually erodes away at the release point, creating more uniform channels. Terrestrial groundwater-derived valleys often have theater-head (uniform box-shaped) starting points, hanging valleys, low junction angles, irregular widening and narrowing, and indistinct ends [*Baker*, 2001]. It has been suggested that valley networks transitioned from precipitation/runoff formation to groundwater seepage formation [*Carr and Head III*, 2010]. However, there is evidence from valleys in Hawai'i that shapes similar to groundwater release can form from waterfall erosion and are not distinguishing characteristics [*Lamb et al.*, 2007]. Therefore, there is debate regarding the determination of Martian valley network formations based on morphology.

Mariner 9 was the first spacecraft to image a number of sinuous channels and branched systems [*Masursky*, 1973]. The combination of MOC (Mars Orbiter Camera) and MOLA (Mars Orbiter Laser Altimeter) data from *MRO* greatly improved the detail of what we could see in the valley networks and showed that they are much more extensive and complex than previously observed in *Viking* images [*Hynek et al.*, 2010] (Figure 3). In the original images, the many isolated single channels resembled groundwater erosion, but the high-resolution images are more indicative of the precipitation-driven formations. These images demonstrated a greater extent of small channels in Martian valley networks and morphological features similar to terrestrial river valleys. Valley networks were measured from updated imagery to be ≤10 kilometers in width and with lengths up to thousands of kilometers [*Baker*, 2001; *Hynek et al.*, 2010]. One way to quantify valley networks is with drainage density, which is the total length of channels divided by the area of the drainage system. Most Martian drainage densities are smaller than those on Earth, but some, near volcanoes and localized Noachian-aged (older than 3.7 billion years) networks, are more comparable [*Gulick*, 2001; *Hynek et al.*, 2010].

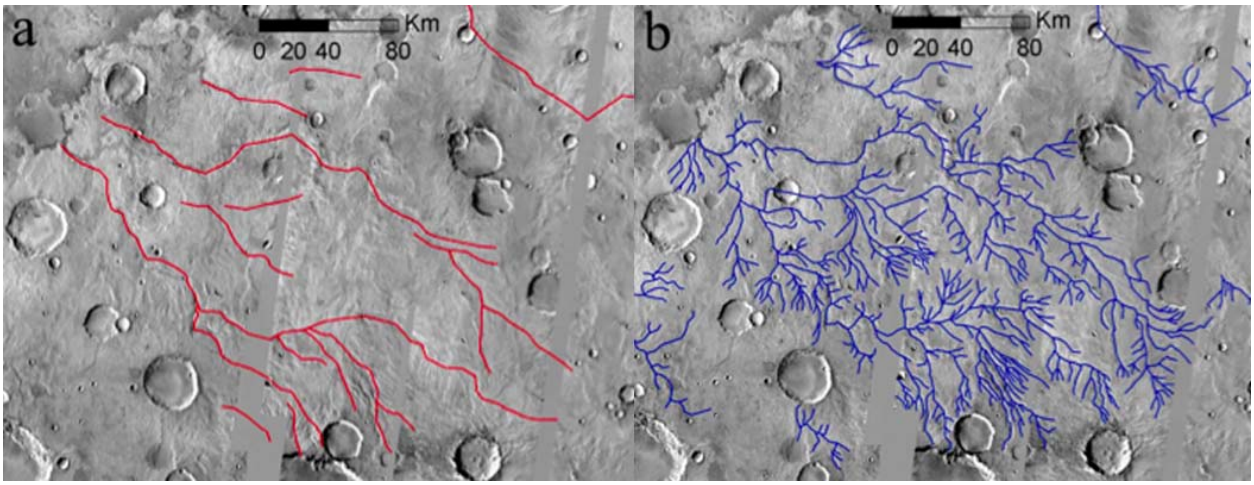

Figure 3. Comparison map of Valley Network extent between A) Viking data and B) THEMIS/MOLA data. From [*Hynek et al.*, 2010].

In larger valley formations, some channels had inner channels, indicating a resurgence of water that eroded a second, smaller channel within an older one, such as Nanedi Valles [Figure 1 in *Malin and Carr*, 1999]. The flow of water can also "cement" valley floors, ultimately making them more resistant to erosion. With time, the surrounding materials were eroded more quickly leaving these floors in higher relief. A more distinct reversal of topography is inverted channels, where the channel floor is now a ridge. For example, inverted channels exist in Medusae Fossae Formation, Miyamoto crater, and Juventae Plateau [*Malin*, 2010].

On Mars, paleolakes can be inferred from terraces, strandlines, and deltas and represent areas where surface runoff may have collected. Terraces are flat platforms along the edge of a lake that form due to the motion of waves or from the collapse of lake edge material [*Ori et al.*, 2000]. Strandlines are evidence of a shoreline caused by lowering water levels. To represent water level, a continuous strandline needs to be along the same elevation similar to those observed on Earth. Hundreds of strandlines have been observed to form in crater basins [*Cabrol and Grin*, 1999; *Fassett and Head III*, 2008b]. *Viking* images showed that closed crater basins had both terraces and Gilbert-style deltas (defined below), which would have formed elevated plains in lakes [*Ori et al.*, 2000]. More recent HiRISE data of Shalbatana Vallis, for example, showed evidence of a paleolake, including a delta and shorelines [*Di Achille et al.*, 2009]. Shorelines are also evident by color or texture differences. Lakes form in closed basins, which sometimes contain outlet channels [*Fassett and Head III*, 2008b]. An outflow channel is formed when enough water accumulates in the basin and drains from that area.

Within these basins, deltas are highly indicative of standing water, which occur at the termination of water flow into bodies of water. On Earth, deltas require persistent, low-energy water to form. The most complex deltas have multiple branches and channels that result from

variability in the flow of water and sediment with time. Gilbert deltas form semicircular platforms at the ends of channels where they open into a basin. Advanced imaging data added detail of these features, demonstrating that complex deltas formed with multiple lobes and branches [*Malin*, 2010] (Figure 4D). As on Earth, these Martian deltas demonstrate many stages of persistent water activity on the Martian surface [*Malin and Edgett*, 2003]. Fluvial activity erodes the surface, forming the valley networks and transporting the eroded sediment downstream. If the channel terminates in a standing body of water, deposition can occur to form

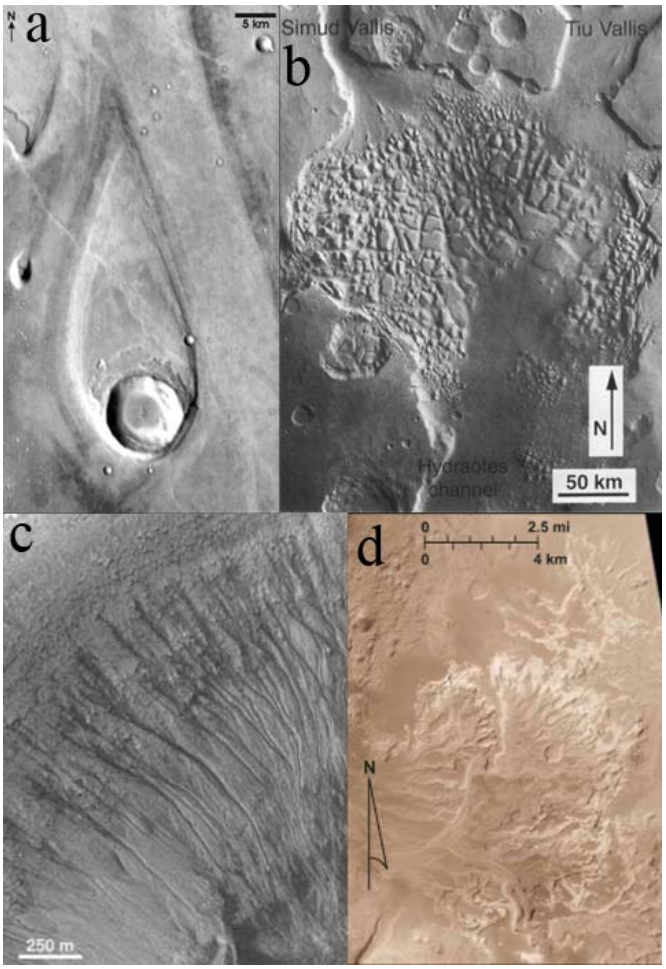

Figure 4. Images of water-related morphological features. A) Streamlined or teardrop island formation in a large outflow channels [*Leverington*, 2004]. B) Chaos terrain, leading to large outflow channels [*Ori and Mosangini*, 1998]. C) Gullies in a crater [*Malin and Edgett*, 2000]. D) Eberswalde delta, representing a complex delta form [*Wood*, 2006].

deltas. As the river flow changes, different lobes of the delta will build into an elaborate form, such as the Eberswalde delta. There is even evidence supporting an ocean-sized body of water about 3.5 billion years ago, through the presence of deltas and shorelines that have a consistent elevation loosely circling the northern hemisphere [*Parker et al.*, 1993; *Di Achille et al.*, 2008]. Numerous deltas in basins with terrestrial-like complexity, sometimes with connecting inflow and outflow channels, are strong evidence for large standing bodies of water.

1.3.2 Orbital Evidence for Ancient Subsurface Water

Morphological features on the surface of Mars indicate water flow. Streamlined islands also support the idea of flowing water [*Masursky*, 1973]. These are teardrop shaped islands in the channels that form when water is forced to flow around an obstacle and are observed in outflow channels (Figure 4A). Large-scale water flow (150 kilometers wide and 2000 kilometers long), floods, create regional extents of chaotic erosion, such as the Channeled Scablands in Washington state that were formed millions of years ago [*Baker and Milton*, 1974]. The Scablands are more analogous to the large outflow channels carved by erosion, rather than the source "chaos" terrains, which formed through erosion rather than collapse. On Mars, there are areas characterized as "chaos" terrains leading into large outflow channels [*Masursky*, 1973; *Malin and Edgett*, 2001]. Chaos terrains are areas of blocky, collapsed materials that transition into channels and can be ten times larger than the valley networks [*Baker*, 2001] (Figure 4B). The suggested cause of such formations is a sudden melting and release of subsurface ice/water, which leads to catastrophic collapse of the overlaying rocks along with a rapid surge of a large flood channel. The trigger for such an event can be a pressurized aquifer, dike intrusion, volcanic influences, and/or gas hydrates [*Baker*, 2001 and references therein]. Each scenario melts and releases the water differently, but they all result in a catastrophic outflow and collapse

of surface rocks. These features are younger than the valley networks and paleolakes, ranging from about 2.8 to 3.4 billon years [*Tanaka*, 1997] (Figure 1). The age difference of these features suggests that as the planet evolved and lost atmosphere, surface water retreated to the subsurface. The Mars climate was no longer able to support sustained surface water, but massive quantities of water could be released by subsequent periodic heat pulses independent of the climate on Mars.

1.3.3 Orbital Evidence for Modern Water

Evidence for water can also be found on a much smaller scale than the evidence left behind by catastrophic flooding. For example, gullies are v-shaped cross-section channels 10s of meters wide. These features are observed on Earth in the perennially cold environments of Canada, Iceland, and Greenland. When soil ice melts or subsurface water is released, it creates flows that erode deep channels on steep slopes [*Malin and Edgett*, 2000; *Costard et al.*, 2001]. These are the youngest features of water on Mars, which represent transient present-day flow of liquid water on the Martian surface [*Mellon and Phillips*, 2001; *Malin et al.*, 2006] (Figure 1). Martian gullies are thin, eroded channels, often found on steep walls of craters and within certain latitude limits [*Malin and Edgett*, 2001] (Figure 4C). Gullies often have a broad starting area about 100 meters, which narrows to a 10 meter-wide v-shaped channel, terminating in a debris fan at the basis of the slope [*Mellon and Phillips*, 2001]. HiRISE images of Terra Sirenum and Centauri Montes, taken about a year apart, showed the appearance of new gullies [*Malin et al.*, 2006]. Although some argue that these gullies are dry formations [*Treiman*, 2003], most proposed formation mechanisms focus on water-carved erosion, given the fluvial nature of the gully properties, including sinuosity, alcove heads, and channels in basal aprons. As with chaos terrains, the source of the liquid water released is debatable. Some suggested explanations

include water with a higher salt concentration or a liquid of CO_2 composition that remains liquid at cold Martian temperatures, a confined subsurface water layer that was released when freezing expansion breaks through the slope wall, and periodic ice melting by geothermal heat [*Malin and Edgett*, 2000; *Mellon and Phillips*, 2001]. Considering that gullies may host contemporary liquid water and that liquid water is critical for life, gullies have the potential to be locations where life could exist presently.

Additional features that are suggestive of transient present-day water flow on Mars are recurrent slope lineae (RSL). In Antarctica, dark streaks that are up to tens of meters wide and several kilometers long form on slopes as a result of water flowing downhill through the soil [*Levy et al.*, 2009; *McEwen et al.*, 2011]. The southern hemisphere of Mars has similar dark streak features that form on steep walls and grow with time. Their appearance and growth are linked to seasonal warming as they disappear in the winter. Brines, or water with salts, have a lower freezing point than water, which may allow them to remain stable on the Martian surface in the cold, dry climate [*McEwen et al.*, 2011]. This seasonality and downhill growth is suggestive of temporary near-surface water, although dry flow has been suggested as well [*McEwen et al.*, 2011].

1.3.4 *In situ* Evidence for Ancient Water

With the deployment of more advanced rovers that could land safely, navigate across the Martian terrain, and carry multiple instruments, detailed studies of the surface were possible. The first fine-scaled textural clues of water observed on Mars resulted from the rover missions. The *Mars Exploration Rover*, *Opportunity*, imaged weathering rinds, dissolution pits (Figure 5A), and cross-bedded deposition layers (Figure 5C) at Meridiani Planum [e.g. *Squyres et al.*, 2004, 2006b]. Within the bedrock, hollow elongated voids appeared to form from the

preferential dissolution of water-soluble minerals. Some of these voids had subsequent mineral fillings, possibly sulfates that often have an aqueous origin [*Squyres et al.*, 2004]. Another textural feature is overlapping sediment layers with crosscutting relations and length-scales that support the hypothesis of subaqueous deposition. A region named "Home Plate" in Gusev crater, where the Spirit rover landed, was characterized by fine strata (Figure 5D) and a bomb sag (Figure 5B), supporting a volcanic deposition [*Squyres et al.*, 2007].

Other observed deposits are alluvial fans that are long (>10 kilometer) debris deposits that are the results of sediment transportation from the flow of water from higher elevations.

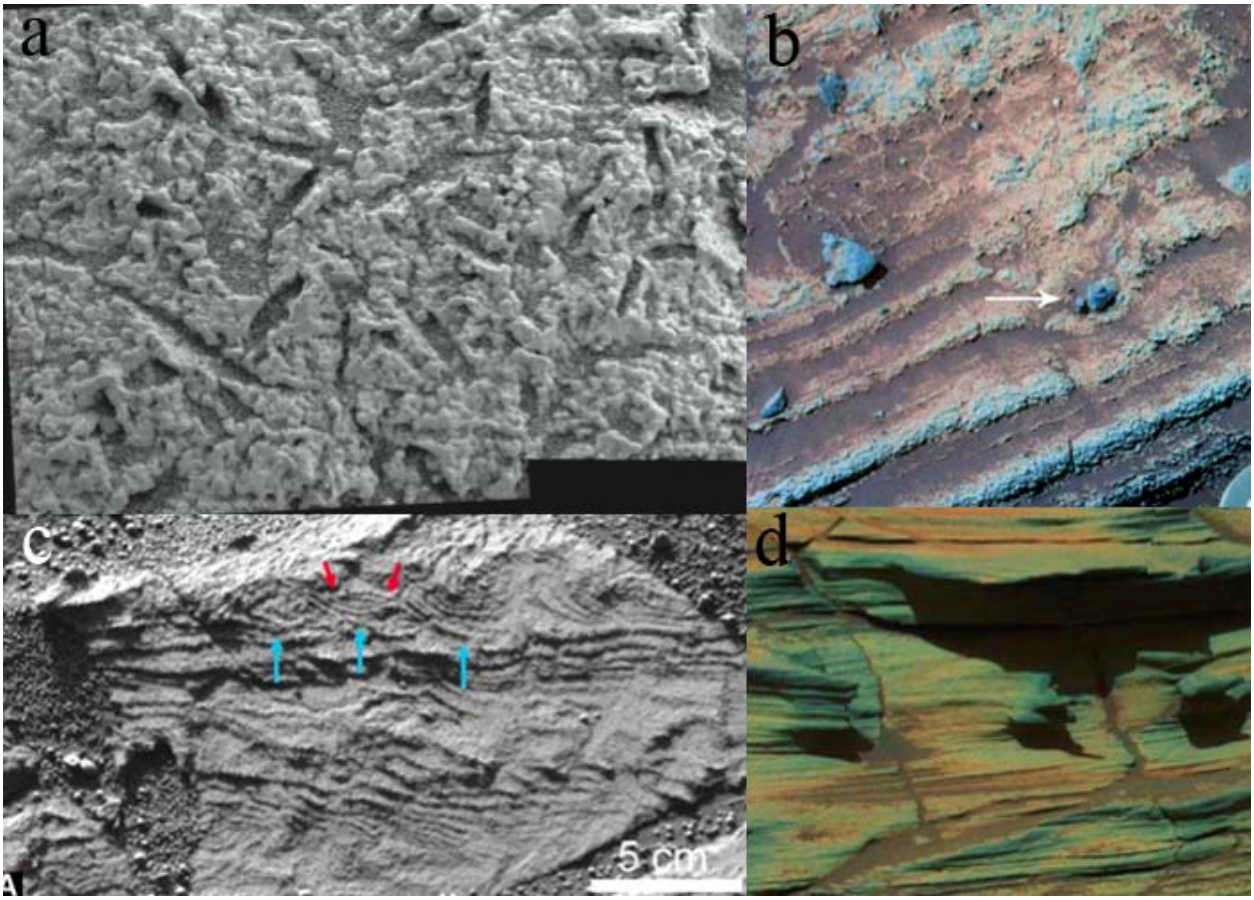

Figure 5. Fine-scale textural features from the Mars Exploration Rovers. A) Voids from preferential dissolution of minerals at Meridiani Planum [*Squyres et al.*, 2004]. B) Volcanic bomb sag at Gusev crater [*Squyres et al.*, 2007]. C) Cross-bedding at Meridiani Planum [*Squyres et al.*, 2006b]. D) Final layers suggestive of pyroclastic deposit [*Squyres et al.*, 2007].

They are often found with distributary channels [*Howard et al.*, 2005; *Moore and Howard*, 2005]. On Earth, they typically form at mountain drainage outlets and build over time with repeated fluid flow. Numerous alluvial fans have been observed in Martian craters and formed around a similar time as the valley networks [*Howard et al.*, 2005]. The slope and shape of Martian fans are similar to Earth river deposits [*Moore and Howard*, 2005]. An alluvial fan located in Gale crater will be explored in detail as the *Mars Science Laboratory Curiosity* [*Grotzinger et al.*, 2012] continues its traverses across the crater [*Palucis et al.*, 2013]. Peace Vallis is the source of this fan and may control the morphology differences between its east and west sides. The west slope is steeper, which may be due to age, material, or flow differences. There is also evidence of inverted channels (as discussed in Section 0), like previously discussed. The fan, its shapes, and its channels are independent lines of evidence for flowing water that likely occurred later in the period of sustained water. Gale crater itself contains evidence of a paleolake [*Irwin et al.*, 2005; *Wray*, 2013]. The preservation of the fan indicates it formed after the lake [*Palucis et al.*, 2013].

Deposits within these types of fans and those that form in terrestrial rivers are unique and can easily be classified as river rocks. In river systems, rocks start at their source as angular, rough pieces. As they travel in energetic waters and/or long distances, sharp corners are broken off until the rocks become rounded. Graded bedding, a feature in which a layer of sediment is sorted by particle size, is also indicative of a former river or channel setting. Novel features observed by *Curiosity* on the Martian surface are conglomerates and the most well-rounded pebbles seen to-date on Mars, which are characteristic of river deposits [e.g. *Grotzinger et al.*, 2013; *Mangold et al.*, 2013; *Williams et al.*, 2013]. The deposits also represent a variety of rock types collected along the entire river. Continued work at Gale crater will characterize the

minerals in the central Gale crater mound [*Milliken et al.*, 2010] with the goal of constraining the geological evolution of the area.

1.3.5 Modern Ground Ice

As Mars lost its early atmosphere, which was capable of supporting the large volumes of surface water as evidenced by the valley networks, it became much colder and drier. Some water was lost to space, by various solar processes and some water retreated to the subsurface. Ground ice was observed by *Phoenix* mission and was exposed when modern mid-latitude craters excavate surface material. *Phoenix* landed in the northern region of Mars equipped with a trench digging arm and scientific instruments [*Arvidson et al.*, 2009]. Almost immediately, it discovered a compact ground ice table averaging 4.6 centimeters below the surface [*Mellon et al.*, 2009]. The most recent orbiter cameras, CTX and HiRISE from *MRO*, also found ground ice exposed by new craters. Subsequent imaging of the fresh impacts showed that the ice had sublimated [*Byrne et al.*, 2009; *Dundas and Byrne*, 2010].

1.4 Chemical and mineralogical evidence

1.4.1 Iron minerals

Mars is an iron-rich planet. Different iron mineralogies (both primary and alteration phases) can highlight the absence or presence of water as well as help identify former environmental conditions. For example, the Mössbauer spectrometer on the *Mars Exploration Rovers* is sensitive to iron, and was able to detect jarosite ($KFe_3(OH)_6(SO_4)_2$) [*Clark et al.*, 2005]. Jarosite is an iron sulfate mineral that is particularly interesting because it forms in acidic environments. In another example, olivine is a primary iron mineral that is sensitive to the presence of water. Water-olivine reactions chemically produce iron-rich minerals, such as hematite, goethite, smectite, and others. The TES (Thermal Emission Spectrometer) instrument

measured olivine, along with an array of other primary minerals [*Christensen et al.*, 2001]. Its presence may indicate areas that did not have much water interaction [e.g. *Hoefen et al.*, 2003].

However, TES did identify aqueous mineralogy in the form of hematite at other locations [*Christensen et al.*, 2000b, 2001]. Hematite is a mineral that can form in several ways, with water playing a key role in most, such as standing water, hydrothermal fluids, and groundwater leaching [*Christensen et al.*, 2000b]. An alternative method is oxidation, but it generally produces a red hematite not observed at this location on Mars. TES measured grey hematite throughout the Meridiani Planum area, which was a driving factor in site selection for the *Opportunity* rover. Confirming orbital data for hematite, *Opportunity* imaged and measured spherical concretions (Figure 6A). Their diameter was smaller than any instrument spot size, but comparison of spherule-covered rocks and spherule-free rocks confirmed a hematite composition [e.g. *Squyres et al.*, 2004, 2006b]. Analyses from the partner rover *Spirit* found both iron sulfates and iron oxides at the Home Plate area of Gusev crater [*Squyres et al.*, 2007; *Lane et al.*, 2008; *Ruff et al.*, 2011].

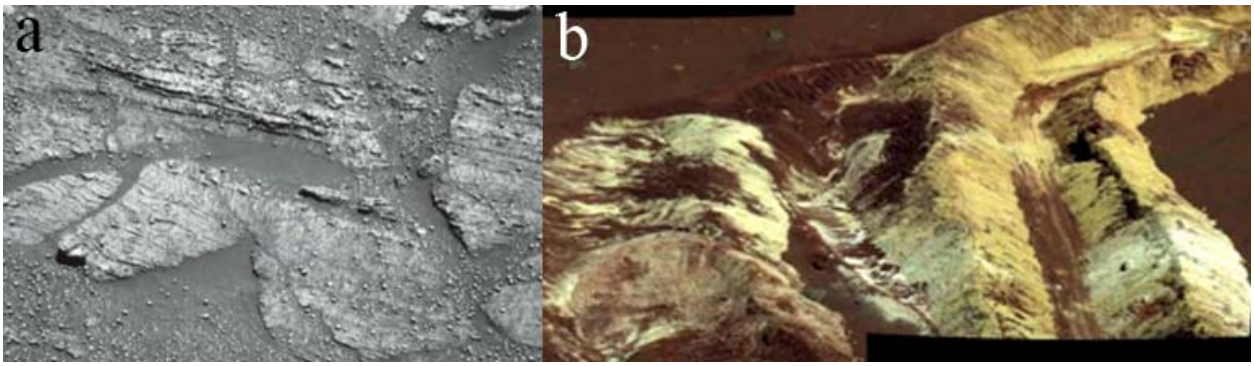

Figure 6. Evidence of water activity at the Mars Exploration Rover landing sites based on mineralogy. A) Meridiani Planum hematite spherules, which often form in water [*Squyres et al.*, 2004]. B) Amorphous silica rich soil overturned by the rover wheel in Gusev crater [*Yen et al.*, 2008].

1.4.2 Phyllosilicates

Phyllosilicates are clay minerals that form more readily in high water environments [*Tosca and Knoll*, 2009], incorporating water into their mineral structure. Although the rovers cannot directly detect these minerals, there is rover-based chemical data suggestive of an aluminum-rich clay. *Spirit* used chemical instruments to analyze a rock class that was enriched in aluminum and silica, probably derived from clay minerals [*Clark et al.*, 2007a]. OMEGA and CRISM have provided the most extensive evidence for phyllosilicates across Mars [*Bibring et al.*, 2006; *Mustard et al.*, 2008; *Ehlmann et al.*, 2009a, 2011b]. Unfortunately, due to resolution difficulties and error in spectral data, specific identification of minerals is not always possible, but minerals can often be assigned to a class of minerals using the most prominent features. The general classes of iron/magnesium-clays and aluminum-clays have been detected in numerous locations, including Valles Marineris and Nili Fossae [e.g. *Ehlmann et al.*, 2011b]. In addition to suggesting the presence of water, the specific type of clay can provide insight into other environmental conditions. For example, aluminum-clays are generally more stable in hydrothermal and acidic environments than Fe/Mg-clays [*Amram and Ganor*, 2005; *Altheide et al.*, 2010; *Gavin and Chevrier*, 2010; *Che and Glotch*, 2012]. This clay, in conjunction with other minerals, may be a diagnostic mineral of acidic and hydrothermal environments.

As opposed to the indirect evidence of water provided by clays, direct measurement of water came from soil samples heated for chemical analysis by *Viking* lander instruments. It is estimated that heated samples tested were about 5% water by weight [*Arvidson et al.*, 1989]. *Phoenix* also heated samples and measured water at two elevated temperatures indicating the presence of multiple water-rich minerals [*Smith et al.*, 2009], which may be related to different types of clay minerals, or the sulfates discussed in the next section.

1.4.3 Salts (Sulfates and Chlorides)

"Salt" is a general term for minerals that form from acidic and basic components forming neutral fluid. Salt compounds found on Mars include sulfates (sulfur chemistry), chlorides or chlorates (chlorine chemistry), and carbonates (carbon chemistry). Salts are associated with formation in water and are often hydrated, meaning water is incorporated into the mineral structure. These minerals can include tens of water molecules within a single mineral unit. Gypsum (a calcium sulfate) and calcium carbonate are examples of minerals that commonly form directly from fluid. Volcanic gas-rock interactions produce many types of salts and such environments may be responsible for some sulfate or chloride deposits on Mars [e.g. *Hynek et al.*, 2012]. Chlorides were also found on a global scale and for the first time using THEMIS data [*Osterloo et al.*, 2008]. Other minerals form from evaporation or very low water-rock interactions.

The first indication of salt chemistry was from the sulfur and chlorine in soils measured by *Viking*. Harder soil crust had 50% enrichment in chlorine and sulfur, which can occur from cementation by water-related salts [*Clark et al.*, 1982]. The *Phoenix* mission in the northern latitudes took images of droplets that formed on the lander struts and appeared to move, merge, and change sizes as coalescing water does [*Smith et al.*, 2009]. Arguments against the occurrence of water droplets include the extremely cold temperature on Mars. However, chemical experiments measured salt perchlorate, which absorbs minute amounts of water vapor and condenses it to liquid by significantly lowering the freezing temperature [e.g. *Hecht et al.*, 2009; *Gough et al.*, 2011].

In addition to perchlorates, soil salt chemistry at the *Phoenix* landing site is dominated by calcium carbonate, which often forms in aqueous environments, particularly oceans [*Boynton et*

al., 2009]. *Phoenix* detected ~2 times less sulfate in soils when comparing the S:Cl ratio at Viking landing site soils [*Kounaves et al.*, 2010]. The discrepancy may be due to differences in analysis technique or simply a difference in the soils. By comparison, *Opportunity* used chemical measurements to infer that soils at Meridiani Planum were rich in sulfates [*Clark et al.*, 2005; *Squyres et al.*, 2006b]. The *Spirit* rover tested materials in an area called Columbia Hills. Soils and rocks at that site had sulfur enrichments, likely from calcium and magnesium sulfates [*Ming et al.*, 2006; *Squyres et al.*, 2006a].

Orbiting instruments showed that sulfates occur globally. Large extents of sulfates have been observed in Valles Marineris chasmata, including gypsum, kieserite (a monohydrated magnesium sulfate), and unidentified polyhydrated sulfates [e.g *Bishop et al.*, 2009; *Wray et al.*, 2009b; *Flahaut et al.*, 2010; *Roach et al.*, 2010b]. Sulfates are also suggested to be indicators of acidic formation environments [e.g. *Golden et al.*, 2005; *McCollom and Hynek*, 2005]. Thus, the presence of sulfates on Mars is one of the strongest mineralogical evidences of acidic and hydrothermal alteration.

1.4.4 Hydrated silica

Hydrated silica comes in many forms, including opal, amorphous phases, and various crystalline phases. Silica frequently forms in volcanic environments or precipitates in hot springs on Earth, and can be used as an indicator of hydrothermal activity and acidity. THEMIS found discrete silica-rich deposits [*Bandfield*, 2008], some of which were up to 80% silica, concentrations that occur in aqueous or volcanic environments. Opaline silica was also detected at Meridiani Planum [*Glotch et al.*, 2006]. Soil and rocks in the Home Plate area of Gusev crater had abundant amorphous silica (Figure 6B) [*Squyres et al.*, 2007; *Lane et al.*, 2008; *Ruff et al.*,

2011]. Given these geographically distinct deposits of hydrated silica, it is reasonable to speculate that some of them may have formed in volcanic hydrothermal conditions.

1.5 Volcanism and Impacts on Mars

In addition to water, volcanism plays a key role in the evolution and habitability of Mars. Mars still had internal heat from accretion and differentiation following its formation, resulting in high volcanic activity. The most obvious sign of sustained volcanism on Mars is the 21 kilometer high Olympus Mons, the largest volcano in the solar system [*Carr*, 1976; *Carr et al.*, 1977; *Robbins et al.*, 2011]. Southwest of this giant volcano is a distinct linear chain of three smaller volcanoes named the Tharsis Montes. Together these four volcanoes and numerous smaller cones form the Tharsis region. Other large volcanic areas are the Elysium region, Alba Patera, and Syrtis Major. Dating the volcanoes using crater counting indicated that volcanism activity occurred as early as ~3.9 billion years and ended recently in geologic history [*Robbins et al.*, 2011] (Figure 1), with the largest volcanic regions having been emplaced by ~3.5 billion years ago [*Phillips et al.*, 2001]. Once established, volcanoes could be periodically active for billions of years [*Robbins et al.*, 2011]. Some volcanoes have multiple summit craters, indicating a restart of volcanic activity in that area.

Based on the morphological features of Martian volcanoes, there was a general transition from explosive eruptions to effusive flows around 3.2 billion years ago [*Robbins et al.*, 2011]. These styles are generally a consequence of volatiles, mainly water, in the erupting magma. Therefore, this transition may be influenced by the loss of water from Mars. As Mars lost internal heat, volcanism slowed considerably and ceased approximately 100-150 million years ago [*Robbins et al.*, 2011]. Also, in general, the surface of Mars is also largely composed of basalt rocks that form from large lavas flows. Many areas on the surface can be characterized as

volcanic flood plains [*Carr et al.*, 1977]. The long period of volcanism and sustained surface water flow suggests that heat and water could have interacted to form the sustained volcanic, hydrothermal systems that are germane to this dissertation.

Transient hydrothermal systems can also occur through heat influx from meteorite impacts. Although impacts presently occur on Mars, there is strong evidence that they occurred more frequently ~3.9 billion years ago due to an event called the Late Heavy Bombardment [*Wetherill*, 1975; *Abramov and Kring*, 2005; and references therein]. Ancient impacts are also much larger, for example the Hellas Basin on Mars. The combination of groundwater or ice and the heat generated by these impacts would have caused impact-induced hydrothermalism. The heat produced during an impact would remain for tens of thousands of years to tens of millions of years depending on the size of the impactor [*Abramov and Kring*, 2005]. Heat could also penetrate into the crust, supplying a warm, moist subsurface environment. Such areas are important for the habitability of a planet.

1.6 Understanding acid-sulfate weathering

With a broad context of the extent of water and volcanism on Mars, the specific reaction progress that is the focus of this dissertation can be understood. Specifically this dissertation concentrates on acid-sulfate weathering in areas of hydrothermal activity on early Mars. There are a number of instances where this type of interaction may have occurred on Mars. At Gusev crater, Home Plate is likely a volcanic deposit. As mentioned previously, amorphous silica is abundant here, which is especially suggestive of hydrothermal activity. However, whether the silica was formed from precipitation out of a hot spring or leaching and removal of all elements except silica in a steam environment is still debated. Mg- and Fe-sulfates are similar to those found at the volcanoes in Nicaragua on Earth that are used as analogs for early Mars [*McCollom*

and Hynek, 2005; *Hynek et al.*, 2012]. *Skok et al.* [2010] demonstrated a correlation of hydrated silica deposits around cone-like structures at Syrtis Major, representing potential fumarole vents. Other volcanic areas, such as Elysium Planitia and Syria Planum, contain smaller cone constructs and probably hosted active hydrothermal activity in the past [e.g. *Baptista et al.*, 2008; *Lanz and Saric*, 2009]. HiRISE also showed some of the first hot spring type vents in Vernal crater [*Allen and Oehler*, 2008]. Another area of magma-rock interaction is Athabasca Valles, which formed from a catastrophic outflow of water that subsequently was covered by some of the youngest lava flows on Mars related to the Cerberus volcanic plains [*Werner et al.*, 2003; *Jaeger et al.*, 2007]. Hydrothermal activity likely occurred in Valles Marineris, a giant rift valley [*Chojnacki and Hynek*, 2008; *Ehlmann et al.*, 2011a]. On Earth, hydrothermal vents are known to occur in rift valleys [e.g. *Tiercelin et al.*, 1993]. These locations on Earth and Mars are environments where acid-sulfate weathering occurs.

Acid-sulfate weathering of basalt commonly occurs in volcanic areas. In this process, high temperature, low pH (acidic), and sulfur-rich vapor interact with water vapor to form sulfuric acid (Eq. 1 and 2). This then condenses on fresh volcanic rock surfaces following these reactions.

$$4SO_2 + 4H_2O = 3H_2SO_4 + H_2S \quad (1)$$

$$H_2S + 2O_2 = H_2SO_4 \quad (2)$$

The acid dissolves the rock and forms a variety of secondary minerals, sulfates, amorphous silica, and Al-clays. However, acid-sulfate alteration as a general weathering process can occur in multiple environments, including volcanic hydrothermal alteration [*Gendrin et al.*, 2005; *McCollom and Hynek*, 2005; *Squyres et al.*, 2007; *Hynek et al.*, 2012], briny evaporitic lakes [*Squyres et al.*, 2004], "dirty" ice [*Niles and Michalski*, 2009], regional acid fog [*Banin et al.*,

1997; *Tosca et al.*, 2004], and impact-induced heat flow [*Knauth et al.*, 2005]. A common factor in all of these mechanisms is the presence of water, although the amount and form vary. Work remains to distinguish these formation environments to more confidently interpret observations from Mars and understand its geological evolution.

1.7 Dissertation Research

The previous discussion outlines the history of water and volcanism on Mars to provide context for this dissertation related to acid-sulfate alteration in a hydrothermal volcanic system. This dissertation research was performed in three parts described in Chapters 2-4. Chapter 2 presents the results from fieldwork completed in August 2012. During this field campaign, I visited three volcanic centers and one hydrothermal site in Nicaragua. These areas are analogs to volcanic hydrothermal systems that may have existed on early Mars. The fieldwork centered around *in situ* visible-near infrared reflectance spectroscopy, a technique that measures the light reflected from a material in the visible to near infrared wavelengths of light (0.35-2.5 μm). The reflected light signal forms a spectrum resulting from chemical bonds within the material. In many but not all cases, this is unique and can be used to identify the minerals present. Having information from the experiments and models from the previous chapter allowed a deeper understanding of the patterns observed here to identify environmental controls of alteration.

Chapter 3 describes a series of laboratory experiments and corollary geochemical models that were designed to examine whether there are distinguishing characteristics of acid-sulfate alteration. I broke basalt into its primary mineral components and reacted them with sulfuric acid (H_2SO_4) under conditions of varying duration, temperature, and fluid:rock ratio. Both laboratory experiments and reproducing the experiments in geochemical models yielded insight into the reaction pathways.

The final portion of my project, Chapter 4, is a remote sensing spectroscopic analysis of an area on Mars where hydrothermal activity is thought to have occurred, Coprates Chasma, a particular area in Valles Marineris. An examination of this area using mineral spectra from CRISM and THEMIS and imagery from HiRISE and CTX, along with the knowledge gleaned in the work described in Chapters 2 and 3, was used to create a hypothesis for the alteration in this canyon. The chapters presented here are in the order in which the work was done and upon completion each segment of the work was (or will be-Chapter 4) submitted for publication in peer-reviewed scientific journals.

To reiterate the driving questions of this dissertation, they are: What minerals comprise the secondary mineral assemblage in a volcanic environment? Are there characteristics of volcanic hydrothermal alteration that distinguish it from other acid-sulfate weathering environments? How may such environments on Mars be identified? By understanding the geological evolution of Mars and comparing that information to Earth's evolution, there is a greater sample size with which to study how planets evolved in the solar system. Additionally, it has been proposed that life on Earth first arose in hydrothermal volcanic environments [*Nisbet and Sleep*, 2001]. Similar environments on Mars may have also been favorable environments for life. Determining the geologic state of ancient Mars in the past would help assess the habitability of red planet, and thus provide astrobiologists with important information to focus their attention on distant locations that are most likely to be able to host life. One of the ultimate goals of astrobiology is finding evidence of life on another planet, and with technological advancements and an understanding of the evolution of Mars, our nearest neighbor, we are coming closer than ever to achieving this goal.

2. Visible-near infrared reflectance spectroscopy of volcanic acid-sulfate alteration in Nicaragua: Analogs for early Mars

Note: This chapter was submitted to the Journal of Geophysical Research-Planets as: Marcucci, E.C., B.M. Hynek, K.S. Kierein-Young, and K.L. Young. "Visible-near infrared reflectance spectroscopy of volcanic acid-sulfate alteration in Nicaragua: Analogs for early Mars." It is cited in the reference list and other chapters as "Marcucci et al., submitted." Sections have been re-numbered and figures are in text to match the formatting of the dissertation. References for this paper have been combined with others at the end of dissertation. Acknowledgements have been combined at the beginning of the dissertation.

Abstract: Acid-sulfate weathering at Nicaraguan sites Cerro Negro, Momotombo, and Telica volcanoes, and the Hervidores de San Jacinto Mudpots was characterized as an analog for similar processes that likely operated on early Mars. *In situ* mineralogical analyses were conducted with a field portable visible near-infrared spectrometer for direct comparison to similar Martian datasets. Three classes of alteration minerals were identified: sulfates, oxides/hydroxides, and phyllosilicates, as well as sulfur and abundant hydrated silica phases. The four sites had similar suites of minerals, but frequencies and variety within each class varied based on visible near-infrared spectrometer. Alteration minerals at Cerro Negro were primarily gypsum, hematite, and goethite, with minor amounts of clays and other sulfates such as hexahydrite and members of the jarosite-alunite family. Momotombo alteration phases were composed largely of hydrated silica and sulfur with fewer sulfates, iron oxides, and clays. Alunite-jarosite group members and goethite dominated the Telica alteration phases, and few other phases were identified. At most locales, a kaolinite+smectite mixture was observed in the acidic systems. The mudpots had an additional clay mixture, montmorillonite and saponite, with minor and trace amounts of sulfates and oxides. The results allow inferences regarding the paleoenvironmental conditions that were likely present at similar relic hydrothermal sites identified on Mars. In particular, spectra from Noctis Labyrinthus, Valles Marineris, and Gusev crater contain the same mineral classes we observed in Nicaragua and likely formed under similar conditions. Acid-sulfate alteration at active basaltic volcanic sites in Nicaragua may represent similar processes that operated on early Mars.

2.1 Introduction

Recent missions have been revealing increasingly detailed mineralogy of the Martian surface using rover instruments and hyperspectral remote sensing data. Sulfates were observed at the Spirit and Opportunity landing sites [*Squyres et al.*, 2004, 2007] and placed into a global context by orbiting instruments [*Bibring et al.*, 2006; *Murchie et al.*, 2009b]. Using visible to short wavelength infrared reflectance spectroscopy (0.37 to 3.92 μm), the Compact Reconnaissance Imaging Spectrometer for Mars (CRISM) and Observatoire pour la Minéralogie,

l'Eau, les Glaces et l'Activité (OMEGA) instruments on board the Mars Reconnaissance Orbiter and Mars Express, respectively, have detected several mineral families, including sulfates, phyllosilicates, and iron oxides in discrete locales across the planet [e.g. *Gendrin et al.*, 2005; *Poulet et al.*, 2005; *Bibring et al.*, 2006; *Bishop et al.*, 2009; *Ehlmann et al.*, 2009b, 2011b; *Murchie et al.*, 2009b; *Wray et al.*, 2009a]. Many of the observations of secondary mineral assemblages imply aqueous alteration of the mafic crust of Mars over long timescales, high temperatures, and acidic conditions.

2.1.1 Secondary Mineralogy of Mars

The Mars Exploration Rovers (MER) Spirit and Opportunity identified sulfates in rocks and soils with the alpha particle x-ray spectrometer (APXS), which measured elemental abundances at the landing sites [*Clark et al.*, 2005; *Squyres et al.*, 2006b]. Mg- and Ca-sulfates at Meridiani Planum were determined by the correlation of S, Mg, and Ca concentrations [*Clark et al.*, 2005]. Additional data from the Mössbauer spectrometer indicated the presence of iron as a jarosite family mineral ($KFe_3(OH)_6(SO_4)_2$) and hematite (Fe_2O_3) [*Squyres et al.*, 2006b], suggesting acidic and oxidizing conditions. In the Columbia Hills region of the Gusev crater landing site, sulfur was detected in several rock classes, including Ca- and Mg-sulfates in the Clovis class and high S enrichments in the Peace class [*Ming et al.*, 2006; *Squyres et al.*, 2006a]. This area also hosts the Independence rock class, which may have a low Fe, high Al/Si phyllosilicate, such as montmorillonite [*Wang et al.*, 2006; *Clark et al.*, 2007a]. Amorphous silica was also abundant, as well as iron phases including magnetite (Fe_3O_4) and nanophase oxides [*Squyres et al.*, 2007]. The rover wheels exposed additional opaline silica and ferric sulfates [*Lane et al.*, 2008; *Ruff et al.*, 2011]. Home Plate in Gusev crater is another area with abundant amorphous silica and sulfates suggesting hydrothermal precipitation from a hot spring

or volcanic gas emissions (i.e. fumaroles) [e.g. *Squyres et al.*, 2007; *Yen et al.*, 2008; *Ruff et al.*, 2011].

Using CRISM and OMEGA hyperspectral reflectance data, additional water-altered mineralogy has been identified across Mars. In particular, a number of sulfates and phyllosilicates have been identified in the Valles Marineris chasmata [e.g. *Gendrin et al.*, 2005; *Bishop et al.*, 2009; *Ehlmann et al.*, 2009b, 2011b; *Murchie et al.*, 2009b; *Wray et al.*, 2009a; *Flahaut et al.*, 2010; *Roach et al.*, 2010b]. Some areas have Fe- (szomolnokite $FeSO_4 \cdot H_2O$) and Mg-monohydrated sulfates (kieserite $MgSO_4 \cdot H_2O$) (e.g., Juventae Chasma) or kieserite and polyhydrated sulfates (e.g., Ius Chasma). Other areas have only a single mineral class detectable from orbit, such as gypsum in Iani Chaos or polyhydrated sulfates in Ophir Chasma. Spectral signatures of polyhydrated sulfates are often non-unique in the wavelength ranges used by CRISM and OMEGA, but may include a variety of hydrated Mg-sulfates or complex Fe-sulfates [e.g. *Gendrin et al.*, 2005; *Poulet et al.*, 2008b; *Bishop et al.*, 2009; *Flahaut et al.*, 2010]. Mineral families are often observed independently of each other, but some association of sulfates and iron oxides or phyllosilicates have also been observed [*Bibring et al.*, 2007; *Poulet et al.*, 2008b; *Bishop et al.*, 2009; *Wray et al.*, 2009b, 2010]. For example, hematite, goethite (FeO(OH)), and ferrihydrite ($Fe_2O_3 \cdot 0.5H_2O$) are found near schwertmannite ($Fe_{16}O_{16}(OH)_{12}(SO_4)_2$) in Meridiani Planum and Margaritifer Terra [*Bibring et al.*, 2007; *Poulet et al.*, 2008b]. Additionally, Cross crater contains minerals in the alunite family ($KAl_3(SO_4)_2(OH)_6$) and kaolinite ($Al_2Si_2O_5(OH)_4$) and Columbus crater contains polyhydrated sulfates, jarosite family members, kaolinite, and some Fe/Mg-smectite. Gale crater also has a thick stack of layered sulfates superposed on top of phyllosilicates [e.g. *Milliken et al.*, 2010].

Understanding the formation environments for each of these mineral types has been a focus of significant research. One hypothesis suggests that phyllosilicates formed earliest in Mars' history, when it was likely warmer and wetter than present day, or in the subsurface from hydrothermal waters [*Bibring et al.*, 2006]. As the planet lost water and fluids became more acidic, sulfates would have formed, possibly in concert with volcanic outgassing. Finally, with continued loss of water, iron oxidation would be the dominant alteration process in the present day dry, oxidizing climate. The mineralogy of Valles Marineris has been the basis for discussions on changing climate regimes and the role of hydrothermalism in sulfate formation [*Clark et al.*, 2005; *Gendrin et al.*, 2005; *Chojnacki and Hynek*, 2008; *Ehlmann et al.*, 2009b, 2011a; *Murchie et al.*, 2009b; *Mangold et al.*, 2010].

2.1.2 Analog Studies

In this paper we focus on volcanic formation environments of secondary minerals from acid-sulfate conditions. Previous studies have used Hawai'i [e.g. *Schiffman et al.*, 2006; *Seelos et al.*, 2010], Rio Tinto, Spain [*Fernández-Remolar et al.*, 2005], and Iceland [*Ehlmann et al.*, 2012] as analogs for Mars. Kilauea on the big island of Hawai'i, emits sulfur-rich gases that form acid fog downwind of the summit [*Schiffman et al.*, 2006]. These areas are dominated by jarosite-natrojarosite sulfates, iron oxides, and amorphous silica in ground and rock coatings [*Schiffman et al.*, 2006; *Seelos et al.*, 2010]. The jarosite mineral family is a strong indicator of acidic and oxidizing conditions. This class is abundant at Rio Tinto in Spain, along with copiapite and iron oxides (i.e. hematite, goethite) [*Fernández-Remolar et al.*, 2005]. Rio Tinto is an acidic area sourcing from a pyrite-rich parent rock, which results in extremely high iron concentrations. The alteration mineralogy is thus dominated by iron sulfates and oxides. Rio Tinto mineral assemblages are also comprised of a number of phyllosilicates, including kaolinite,

montmorillonite, smectites, and illite [*Fernández-Remolar et al.*, 2011]. In Iceland there is a range of environments, including low temperature and sulfur, high temperature and sulfur, and low temperature and high sulfur [*Ehlmann et al.*, 2012]. This study examined mineralogy of the main volcanic centers and found abundant Al and Fe/Mg smectites, hematite, and hydrous silica phases.

We have been studying the Cerro Negro volcano, Nicaragua analog site to characterize a volcanic, hydrothermal acid-sulfate alteration environment [e.g. *Hynek et al.*, 2011]. Although acid-sulfate weathering is credited as the general formation mechanism of the sulfates on Mars, the specific environmental conditions have been heavily debated and hypothesized environmental conditions span a wide range of temperatures, fluid:rock ratios, and pH values [e.g. *Banin et al.*, 1997; *Squyres et al.*, 2004, 2007; *Tosca et al.*, 2004; *Knauth et al.*, 2005; *McCollom and Hynek*, 2005; *McLennan et al.*, 2005; *Ruff et al.*, 2011]. Early in Martian history, when the internal heat was greater and/or impacts were more frequent, hydrothermal areas were likely widespread on the planet [*Abramov and Kring*, 2005; *Hynek et al.*, 2011]. Cerro Negro was assessed to determine if there are diagnostic features of volcanic hydrothermal formation environments that can facilitate interpretation of lander and orbiting data from Mars.

There have been a number of field campaigns to Cerro Negro to collect rock, soil, gas, and biological samples [e.g. *Hynek et al.*, 2011]. Collected soil and rock samples were analyzed with x-ray diffraction (XRD), x-ray fluorescence (XRF), thin section petrography, and scanning electron microscopy/energy dispersive spectroscopy (SEM/EDS); inductively couple plasma-atomic emission spectroscopy was used for fluid samples that resulted from condensed steam [detailed in *Hynek et al.*, 2011]. Previous work at Cerro Negro demonstrated that generalized alteration mineralogies can be grouped into two categories: accumulation of amorphous silica

and deposition of sulfates, specifically Ca-sulfate [*Marcucci et al.*, 2010; *McCollom et al.*, 2010, submitted; *Hynek et al.*, 2011, submitted]. In general, complex sulfates, iron oxides/hydroxides, and phyllosilicates were found with less frequency than amorphous Si and Ca-sulfate.

Laboratory experiments and geochemical models were used to constrain potential reaction pathways at Cerro Negro [*Marcucci and Hynek*, submitted; *McCollom et al.*, 2013]. The experiments showed that the main control of secondary mineralogy is the primary rock composition. Formation conditions, such as temperature, fluid:rock ratio, and duration of alteration, have a greater effect on the size, abundance, and morphology of crystalline products than on the overall alteration assemblages. The contribution of fluid evaporation has also proven to be important for understanding the reaction pathways. For example Mg-sulfates are exclusively formed during evaporation in experiments [*Marcucci and Hynek*, submitted]. These experiments and models can improve our interpretation of field observations, and allow applications to Mars.

2.1.3 Motivation

The work presented in this paper examined *in situ* mineralogy of four hydrothermal volcanic areas in western Nicaragua using a field spectrometer that measured reflectance in the visible to near infrared (VNIR) wavelength range. This range is sensitive to electronic absorptions characteristic of the presence of minerals with transition metals, most commonly Fe [e.g. *Clark et al.*, 1990]. Sharper combination and overtone vibrational absorptions indicate the presence of H_2O, metal OH, and CO_3. Many alteration phases, both in the field and in experiments, occur in abundances too low for detection by XRD and require SEM/EDS for identification. Additionally, alteration commonly occurs in the field as a mixture of resultant sediments, thin surface coatings on rocks, or as broader encrustations. A field reflectance

spectrometer can quickly identify these less abundant phases. Furthermore, instruments that utilize reflectance in this wavelength range are commonly flown on orbiters and are a useful tool for investigating surface composition remotely. This ability to take measurements *in situ* is critical since minerals often change when removed from their natural environment. A common example is change in hydration state as relative humidity changes, which happens during transit and storage [e.g. *Steiger et al.*, 2008].

Here, we present results from our Nicaraguan field campaign in August 2012, which visited three sites in addition to the Cerro Negro field site, and focused on *in situ* analysis of alteration products with instruments similar to those used at Mars. Our spectroscopic investigations were conducted in conjunction with x-ray diffraction (XRD) and biological investigations in the field [*Hynek et al.*, submitted; *Rogers et al.*, 2011, respectively] and complementary laboratory experiments and geochemical modeling [*Marcucci and Hynek.*, submitted; *McCollom et al.*, 2013]. This paper focuses on the spectroscopy results for specific volcanic sites and compares our results to observations on Mars, while *Hynek et al.* [submitted] discusses regional context and environmental constraints, as well as the XRD results and *McCollom et al.* [submitted] focuses on more generalized chemical and mineralogical trends during acid-sulfate alteration in areas of diffuse vapor discharge. The goal of this work is to answer the following questions: What minerals form in these acid-sulfate environments based on field VNIR reflectance spectroscopy? What are the strengths and weaknesses of using VNIR reflectance spectroscopy? How do these field sites compare to specific locales on Mars and what can we conclude regarding the paleoconditions present during their formation?

2.2 Field Sites

This study focuses on three currently active volcanic areas, Cerro Negro, Momotombo, and Telica volcanoes, and one associated hydrothermal area, Hervidores de San Jacinto, in western Nicaragua to study the controls of acid-sulfate alteration (Figure 7 to Figure 10). The regional setting of these volcanoes and additional geologic context is discussed in detail in *Hynek et al.* [submitted], and salient details of the sites discussed here are summarized below. Due to the geographical proximity of the three volcanoes in our study, the magma sources are very similar. This translates to similar rock compositions of the erupted products, but key differences may influence secondary mineralogy [e.g. Carr et al., 1990, 2007; Patino et al., 2000]. While rock composition is similar (basalts to basaltic-andesites), there is more variation in the volcanic gas emissions [Elkins et al., 2006].

The primary field site for this study was Cerro Negro volcano, Nicaragua (Figure 7). This is a young volcanic complex with a well-documented eruption history, with the most recent eruption in 1999. Cerro Negro has been used for a number of years as an analog for early Mars, because the lithology of unaltered rock is similar to that of unaltered Martian basalt, with exceptions in the concentration of Fe and Al [*Hynek et al.*, 2011; submitted; *McCollom et al.,* submitted]. Recently erupted Cerro Negro basalt is primarily composed of large phenocrysts of plagioclase, pyroxene, and olivine with volcanic glass and titanian magnetite. This study investigated the alteration on the 1992 eruption crater wall and the rim of the 1995 eruption crater. The 1992 eruption crater wall consists of a number of localized fumaroles and more diffuse soil hotspots. We measured temperatures from 50°C (rocky areas) to >100°C (at the surface of fumaroles) to 400°C (several centimeters into vents). Similarly, pH ranged from ~6.5

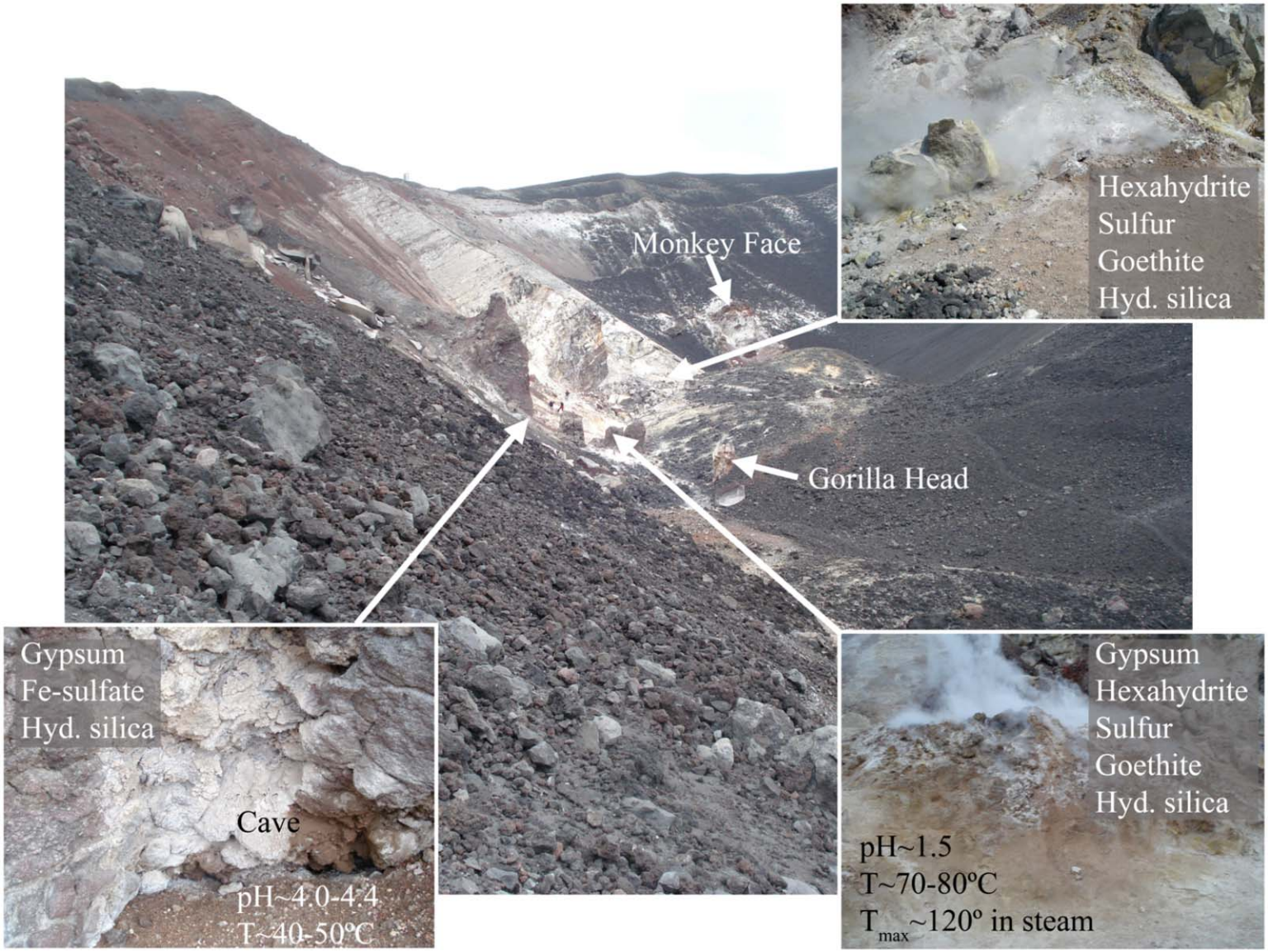

Figure 7. Field images of Cerro Negro with mineralogy identified by *in situ* VNIR reflectance spectroscopy and environmental parameters.

Figure 8. Field images of Momotombo with identified secondary mineralogy from *in situ* VNIR reflectance spectroscopy.

Figure 9. Field images of Telica with identified secondary mineralogy from *in situ* VNIR reflectance spectroscopy.

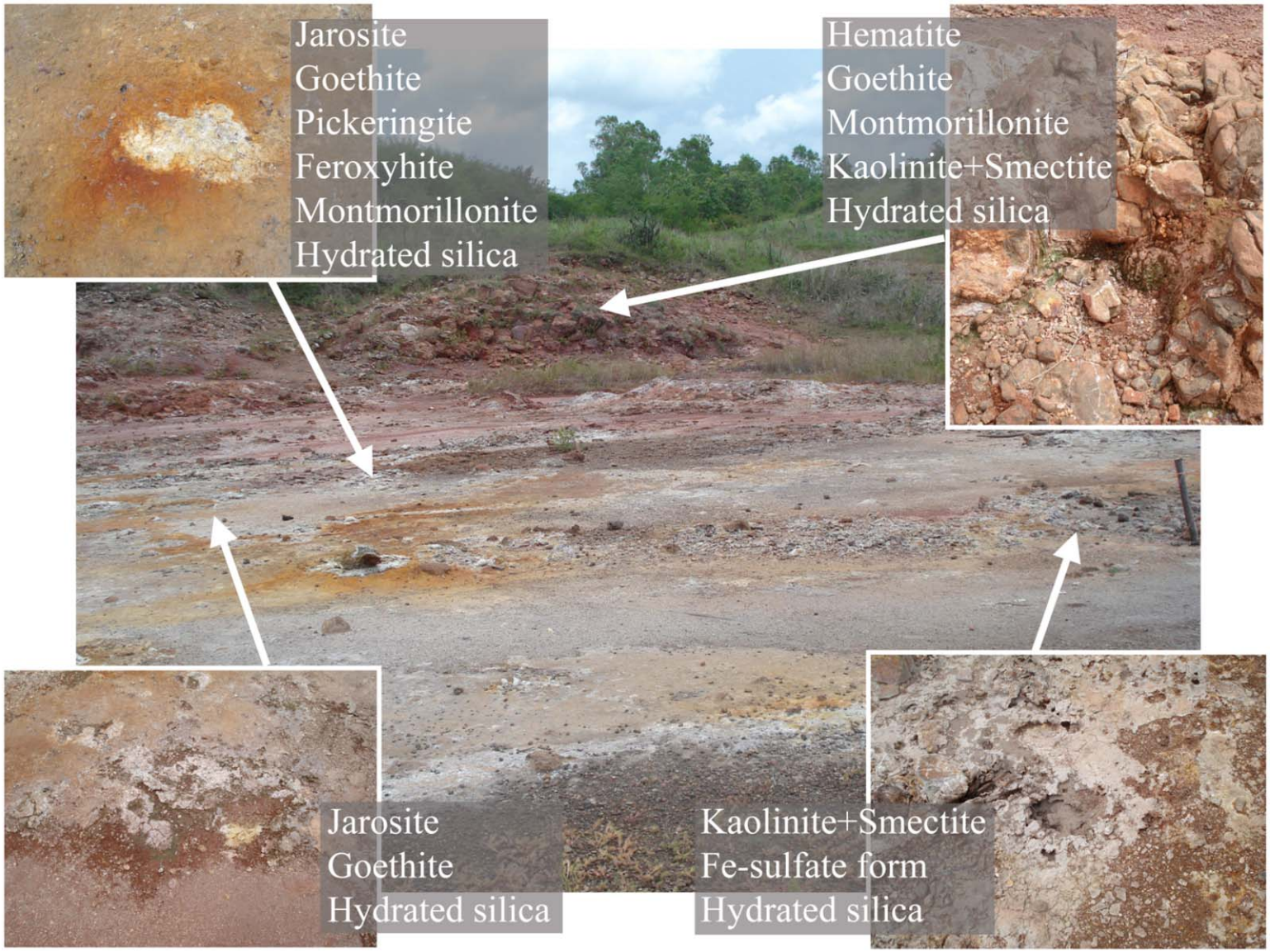

Figure 10. Field images of the San Jacinto Mudpots with identified secondary mineralogy from *in situ* VNIR reflectance spectroscopy.

to -1, with the lowest values measured at hot fumaroles near the center of the crater. See *Hynek et al.,* [submitted] for more detailed descriptions. We collected samples from fumaroles (arranged loosely in a grid), loose soil and drainage areas, and rocks that appeared altered or were situated in the fumarolic steam. Although no concentrated fumaroles occur on the 1995 crater rim, alteration was widespread from diffuse hot and acidic steam. The areas sampled here were generally cooler than the 1992 wall, at 50-90°C. Because this area was drier and had a more expansive hard surface crust, pH could not be easily measured. At two sites, there was enough surface moisture for measurements to be taken, which both had pH ~1.6.

Our campaign also investigated the neighboring volcanic systems of Momotombo and Telica. Momotombo volcano is a classic stratovolcano that last erupted in 1905 and that has a very hydrothermally active summit crater (Figure 8). Temperatures within parts of the crater were measured to be over 450°C, although sampling was mostly done on the fringes due to hazardous conditions. At this site, measurements were taken from both bedrock and on float samples. The *in situ* samples were accessible rocks and soils that appeared highly altered. To get a wider range of samples that were available at the sampling site, half a dozen float rocks, which formed in the crater, but may have been transported since then, were also measured.

The third volcano explored was Telica, an active stratovolcano with the most recent significant eruption in 2011 (Figure 9). Unlike Cerro Negro and Momotombo volcanoes, the heavily altered interior of the Telica crater was not accessible and our samples consisted of ejected blocks and altered rim materials. With the exception of two brightly colored rock alteration patches on the rim, all samples collected were from the surfaces of ejected rocks.

The final field site explored was the Hervidores de San Jacinto (or San Jacinto Mudpots), a geothermal area on the southwest flank of (but still part of the Telica volcanic center) (Figure

10). Here, hydrothermal waters circulate in the shallow subsurface producing steam vents and bubbling mudpots on the surface. The samples measured at this site include surface encrustations, dry and wet mud, and parts of a rock wall with diffuse steam.

2.3 Methods

2.1.1 Field Measurements

We employed a TerraSpec4 high resolution reflectance spectrometer developed by Analytical Spectral Devices, Inc. This portable field instrument measures reflectance from VNIR wavelengths, a range containing critical information for mineral identification, including water hydration bands. The high signal-to-noise allows for the accurate detection of dark minerals, such as volcanic basalt and glass, that have minimal reflectance. The TerraSpec4 has three detectors that measure a total wavelength range of 0.35-2.50 μm. The VNIR detector (0.35-1.00 μm) is a 512 element silicon array with a signal-to-noise ratio of 9000:1 and 3 nm resolution at 0.70 μm. There are two graded index InGaAs photodiode, TE cooled, short wavelength infrared detectors for the ranges of 1.001-1.80 μm and 1.801-2.50 μm. The signal-to-noise of these detectors is 9000:1 at 1.40 μm and 4000:1 at 2.10 μm, respectively, both with a spectral resolution of 6 nm.

For field measurements, a handheld contact probe (shown in Figure 9) with a broadband halogen light source was put in direct contact with the sample to be measured, essentially eliminating any atmospheric contributions. The contact probe had a 10 mm spot size. The reflected light was captured by a fiber optic cable, which was positioned next to the light source and connected to the instrument detectors. A second cylindrical light source with a spot size of 12 mm, the Muglite accessory, was used for loose field samples and operated by placing a sample holder packed tightly with enough material to avoid light escape on the top of the light

source. The instrument communicated with a linked laptop computer, on which the data can be viewed continuously in real time. Before field samples were measured, dark current, white balance, and optimization controls were run to calibrate the collected spectra. Spectrum collection took approximately 15 seconds to obtain and was checked for clarity in the field. Spectra were exported to an external software program for subsequent analysis. Potential errors result from light leak that can cause: 1) entering sunlight to artificially brighten the spectrum, or 2) the detector to capture light reflecting off of something behind the sample being measured. To avoid these issues, we choose samples that were at least as large as the spot size and kept a firm seal between the sample and instrument.

2.3.2 Spectral Identification

Spectra were analyzed and mineralogies identified using the IDL/ENVI software package. The spectra were grouped based on location and minerals were manually identified by matching features in the field spectra to those within reference library spectra. The libraries used were the United States Geological Survey mineral library [*Clark et al.*, 2007b] and the CRISM sulfate, rock, and oxide libraries that accompany the CAT Tools ENVI add-on [*PDS Geosciences Node and CRISM Spectral Library Working Group*]. Since reflectance spectra are influenced by factors such as grain size and solid solution contributions, which can cause small changes in band centers or depths, there is a certain degree of uncertainty associated with mineral identification [*Morris et al.*, 1985]. Reference libraries include spectra with both natural and laboratory samples and with variable grain sizes and a range of solid solutions that improve the confidence in identification. For the most accurate identification of the minerals within the field data, we examined each of the reference spectra within a library and between libraries from

Table 1. Characteristic spectral features used for identification[1].

	Characteristic Bands (μm)
Sulfates	
Gypsum	1.4 (triplet), 1.76, 2.2 (doublet)
Hexahydrite	slope at 1.3, 1.4, 1.9
Alunite mineral family	1.4 (doublet), 1.76, 2.1, 2.3
Jarosite mineral family	0.43, 0.7, 0.9, 1.4, 1.85, 2.2
Pickeringite	0.43, slope at 1.4
unidentified Fe^{3+} sulfate	0.43
Oxides/Hydroxides	
Hematite	0.65 (shoulder), ~0.87
Goethite	0.65 (shoulder), ~0.90
Phyllosilicates	
Kaolinite+Smectite	2.2 (asymmetric)
Kaolinite	2.2 (doublet)
Montmorillonite	2.2 (singlet)
Saponite	2.3 (singlet)
Miscellaneous	
Elemental Sulfur	~0.4 shoulder, flat
Hydrated Silica	1.4, 1.9, ~2.25

[1]See Figure 11 through Figure 14 and the text for additional discussion

different sources. To identify the mineralogy from the spectra, priority was placed on matching band locations and general spectral shape over band depth or slope (Table 1). We were confident in our fit when all major spectral bands from the reference spectrum matched with the field sample. Mixtures of minerals complicated the identification, but we matched the dominant features first, before adding other minerals to account for any additional spectral bands. We qualitatively assessed mineral occurrences as major, minor, or trace components. We identified the major mineral phases composing the upper few microns of surfaces. The bulk samples might not have total concordance with these surface coatings, but this is also the case for Mars. For a detailed comparison between mineralogy results obtained from VNIR spectroscopy versus XRD on the same field samples see *Hynek et al.,* [submitted].

2.4 Results

2.4.1 Mineral Classes

We collected approximately 60 spectra at Cerro Negro, 50 at Momotombo, 10 at Telica, and 20 at San Jacinto and included a few fresh basalt samples and a wide range of altered products. The types of samples measured were rocks, soils, coatings, and encrustations from particularly hot, acidic areas near fumaroles progressing to cooler and lower acidity areas on the aprons to ambient temperature surfaces of nearby altered boulders. Topographic lows where runoff water had previously pooled and evaporated were also measured.

Generally, the four sites studied in Nicaragua shared a variety of common alteration minerals (Table 2). Like Mars, dominant categories were sulfates, iron oxides/hydroxides, and phyllosilicates (Figure 11 to Figure 14). Virtually all spectra had very well defined 1.4 and 1.9 μm hydration bands. These features along with broader features at 2.25 μm are indicative of an amorphous silica component—most closely matching siliceous sinter and opal in the spectral libraries used and herein is referred to as hydrated silica (Figure 13D). In some cases a specific mineral could not be identified; however, the family of minerals could be matched. Below we discuss our results by grouping the spectra into four classes: 1) sulfates, 2) oxides/hydroxides, 3) phyllosilicates, and 4) miscellaneous. Generally, sulfates were the most frequent, followed by minor amounts of oxides/hydroxides, and minor to trace amounts of phyllosilicates (Table 2).

2.4.1.1 Sulfates

We detected mono-cation sulfates with Ca (gypsum) and Mg (hexahydrite); multiple cation sulfates: alunite-jarosite minerals and pickeringite ($MgAl_2(SO_4)_4 \cdot 22H_2O$); and an unidentifiable Fe^{3+} sulfate. Gypsum spectra were identified via comparison to the spectral libraries [*Clark et al.*, 2007b] and specifically by matching the triplet absorption band near 1.4

Table 2. Summary of spatial frequency of identified secondary mineralogy[1].

	Cerro Negro	Momotombo	Telica	Mudpots
Sulfates				
Gypsum	Major	Minor	--	Minor
Alunite (natroalunite)	Minor	Minor	Major	--
Jarosite (Fe-rich natroalunite)	Minor	Trace	Major	Minor
Hexahydrite	Minor	--	--	--
Pickeringite	--	Trace	--	Trace
Fe-sulfate	Trace	Minor	Minor	Trace
Oxides/Hydroxides				
Hematite	Major	Minor	--	Minor
Goethite	Major	Minor	Major	Major
Iron Oxide	Trace	--	--	--
Feroxyhite	Trace	--	--	Trace
Fe-oxide form	--			
Ferric oxide	--	Trace	--	--
Phyllosilicates				
Kaolinite	--	Trace	--	--
Kaolinite +Smectite	Trace	Trace	Minor	Minor
Montmorillonite	--	--	--	Minor
Saponite	--	--	--	Minor
Miscellaneous				
Hydrated silica	Major	Major	Major	Major
Sulfur	Minor	Major	--	--

[1]These are proportions of minerals relative to all of those identified at the site with VNIR reflectance spectroscopy, which does not necessarily reflect the actual distribution for the entire area or relative abundances from a single sample. These were categorized as major (>10%), minor (1% to 10%), or trace (<1%) mineral contributors.

μm, the band at 1.76 μm, and the doublet near 2.2 μm (Figure 11A and C; Figure 12D; Figure 14F). The *in situ* deposits were often monomineralic, generally white or off-white, and located near fumaroles of more moderate temperature and pH (Figure 7). White rock coatings were also commonly identified as gypsum often in more ambient conditions (Figure 8). Field spectra that included two hydration bands and a decreasing slope starting at about 1.3 μm best matched hexahydrite [*PDS Geosciences Node and CRISM Spectral Library Working Group*] (Figure 11D). This sulfate was often found in hot wet sediments associated with fumarole aprons at the

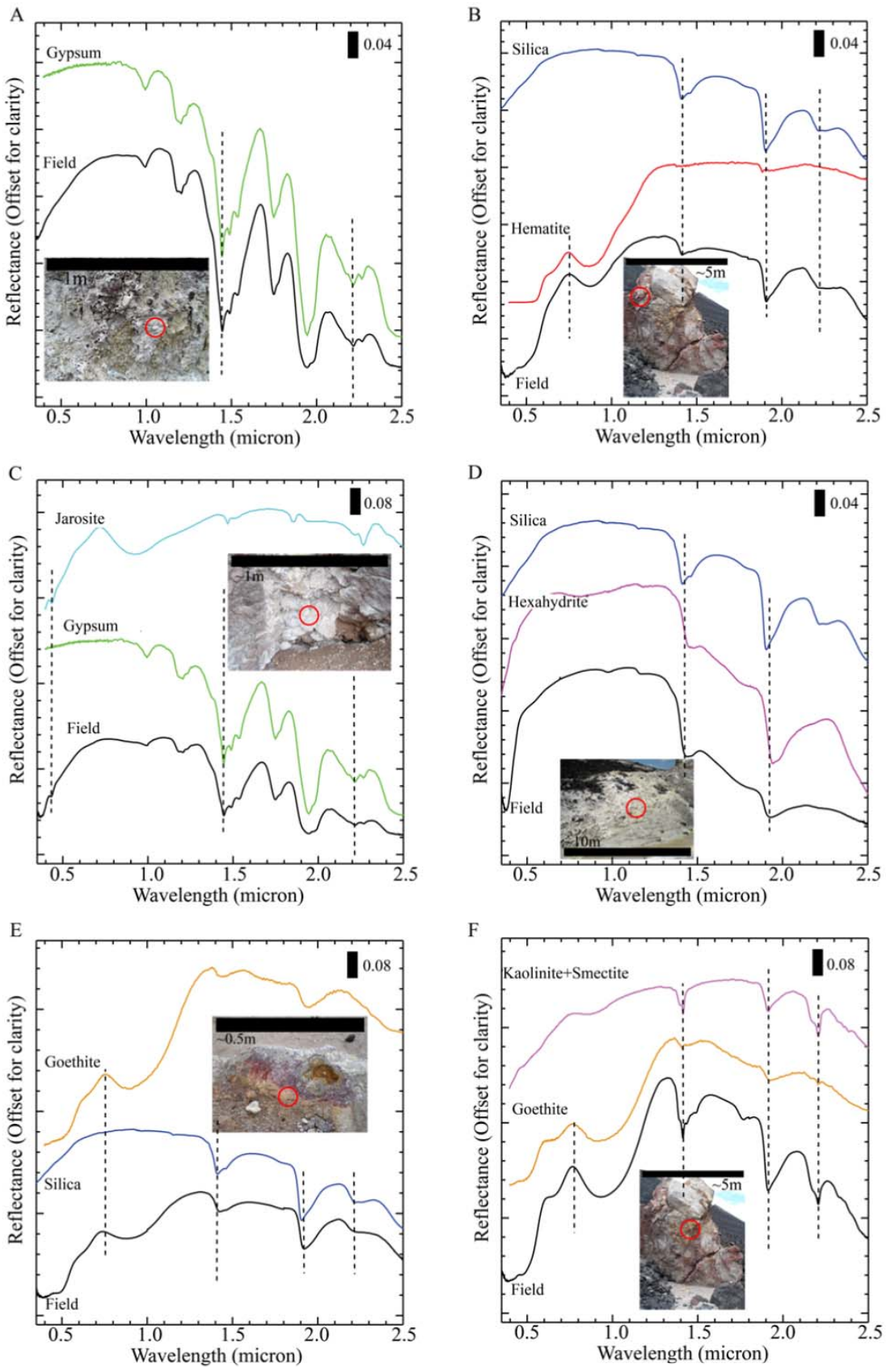
A
Gypsum
Field
0.04
~1m
Reflectance (Offset for clarity)
Wavelength (micron)
B
Silica
Hematite
Field
0.04
~5m
C
Jarosite
Gypsum
Field
0.08
~1m
D
Silica
Hexahydrite
Field
0.04
~10m
E
Goethite
Silica
Field
0.08
~0.5m
F
Kaolinite+Smectite
Goethite
Field
0.08
~5m
0.5
1.0
1.5
2.0
2.5

Figure 11. Example field spectra of sulfate, oxide/hydroxide, and phyllosilicate minerals present at Cerro Negro, Nicaragua. The label after each mineral is an indication of the library reference name. Each reference is labeled first time it is used; assume subsequent references are the same, unless otherwise stated. Library spectra are scaled to match the general reflectance levels of field spectra by a simple linear multiple, for example 0.5. This does not change the spectral shape, but lowers the absolute reflectance of the library spectra for easier comparison to field samples. (A) Gypsum (Gypsum HS333.3B) is identified in a white deposit from the 'Monkey Face' feature in Figure 7. Gypsum is often identified by itself. (B) Example of an iron mineral, hematite (Hematite GDS27) measured as a rock coating on 'Gorilla Head' with additional hydration from hydrated silica (Siliceous Sinter BKR1JB329C). (C) Spectrum from the cave in Figure 7 that is dominated by gypsum, but also contains a band at 0.43 μm, normally indicative of Fe^{3+} in the jarosite mineral family (Jarosite JR2501K), but it lacks longer wavelengths features. This could be from mixing of several phases, such that a small amount of a jarosite family mineral is masked by gypsum. This feature may also be from an Fe-rich natroalunite (see text for details). (D) Spectra of hexahydrite (Hexahydrite LASF56A), an evaporitic mineral, for a drainage site in the topographic lows of Figure 7. (E) Goethite (USGS Goethite WS220) and silica signals match the spectrum from the orange portion of this highly altered rock. (F) Spectrum from the brown portion of 'Gorilla Head' in B with goethite (USGS Goethite WS219) and kaolinite+smectite (USGS Kaolin/Smect506 95%K).

Cerro Negro crater or adjacent outwash areas (Figure 7). Sulfates in the alunite-jarosite mineral families were found in intimate mixtures with each other, as well as with iron oxides (Figure 12E and F; Figure 13C and E-F). Features of the alunite mineral family include a doublet around 1.4 μm, and bands at 1.76, 2.1, and 2.3 μm. These bands are similar to those of natroalunite and alunite identifications could actually be natroalunite (see further discussion below). Characteristic jarosite mineral family features occur at 0.43, 0.7, 0.9, 1.4, 1.85, and 2.2 μm. These minerals were identified using several reference spectra [*Clark et al.*, 2007b]. While fits to many of our field spectra included jarosite and alunite family members, analysis by SEM/EDS indicated that most of these samples have a composition corresponding to Fe-bearing natroalunite, with members of the jarosite family being very rare [*McCollom et al.,* submitted]. Accordingly, the spectral features we attribute to the alunite-jarosite mineral families mostly likely correspond to natroalunite and Fe-bearing natroalunite, respectively; however, reference library spectra for these intermediate composition solid solutions do not exist. Hereafter, we

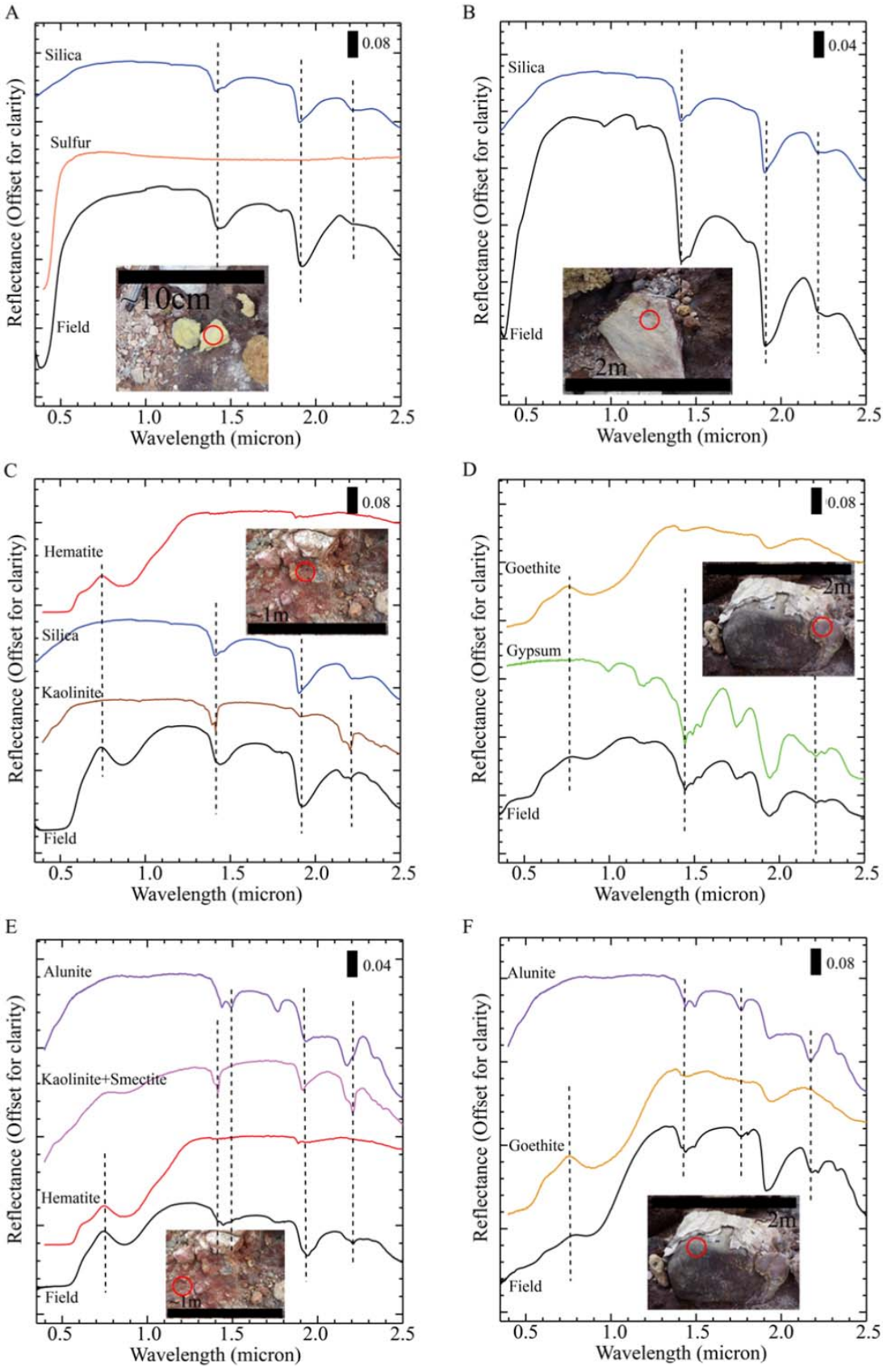
A
Silica
Sulfur
Field
0.08
~10cm
Reflectance (Offset for clarity)
Wavelength (micron)
B
Silica
Field
0.04
2m
C
Hematite
Silica
Kaolinite
Field
0.08
~1m
D
Goethite
Gypsum
Field
0.08
~2m
E
Alunite
Kaolinite+Smectite
Hematite
Field
0.04
~1m
F
Alunite
Goethite
Field
0.08
~2m

Figure 12. Example field spectra for Momotombo volcano. Library spectra are scaled to match the general reflectance levels of field spectra as described in Figure 11. (A) Example of a bright yellow deposit showing sulfur (USGS Sulfur GDS94 Reagent) and hydrated silica from a float crystal in Figure 8. (B) An example of pure hydrated silica in a rock with several layers of weathering (right panel in Figure 8). (C) Red clay material identified as hematite and kaolinite (USGS Kaolinite CM7), with additional hydrated silica in a soil formation. (D) Weathering rind, which contains gypsum and goethite (USGS Goethite WS220), example of when gypsum is not found alone (right panel of Figure 8). (E) Red clay area with a mixture of kaolinite+smectite, hematite, and a member of the alunite family (USGS Alunite GDS82 Na82) minerals. (F) Lowest exposed surface of a large weathered rock (same at D) with alunite and goethite.

refer to spectral identifications of alunite and jarosite as natroalunite and Fe-bearing natroalunite, respectively, to represent the range of compositions that may be present within the samples. At Cerro Negro and San Jacinto Mudpots, these mineral deposits were mixed in soils of moderate temperature and generally low pH (Figure 10); at Momotombo and Telica they composed rock coatings at ambient temperature (Figure 8; Figure 9). Occasionally, spectra shared key features with library references, but other prominent features were missing. This was most common with an Fe^{3+} near 0.43 μm, a very distinctive feature of jarosite mineral family spectra [*Cloutis et al.*, 2006]. However, the field spectra did not share longer wavelength features with this family (Figure 11C). For reasons discussed below, a determination of Fe-sulfate versus ferric oxide was chosen.

2.4.1.2 Oxides/Hydroxides

The predominate phases found in this class of minerals were hematite (Fe_2O_3) and goethite (FeO(OH)), based on similarities to the library spectra (Figure 11B and E-F; Figure 12C and E-F, D; Figure 13C and E-F; Figure 14D-E) [*Clark et al.*, 2007b]. Distinguishing features include a peak around 0.7 μm and a broad absorption band at a slightly longer wavelength. Hematite has a band at 0.87 μm and goethite has a broader band at 0.90 μm, which allows discrimination between the two minerals. These oxidized iron minerals were present in samples

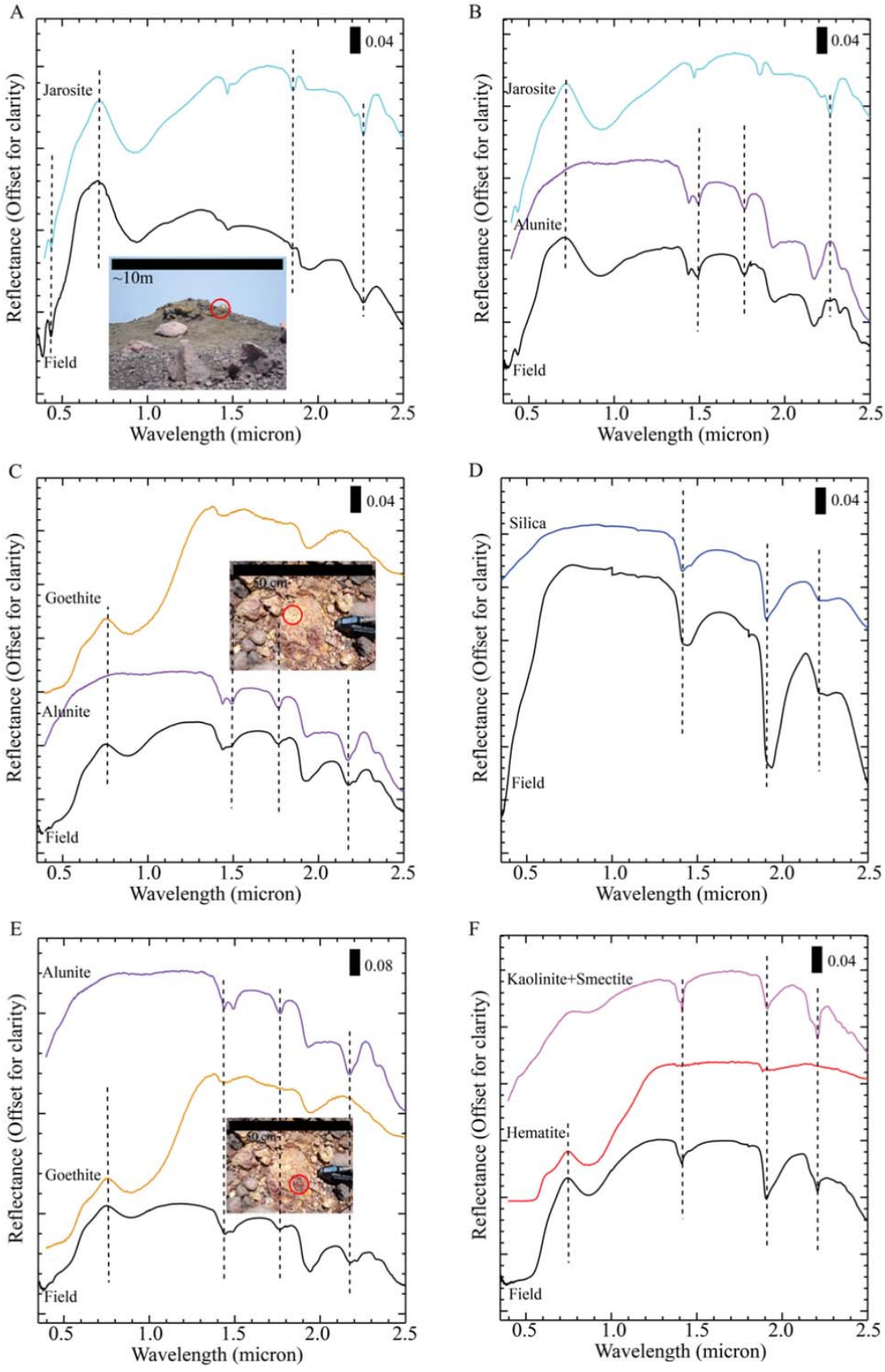
A
0.04
Jarosite
~10m
Field
Reflectance (Offset for clarity)
0.5
1.0
1.5
2.0
2.5
Wavelength (micron)
B
0.04
Jarosite
Alunite
Field
Reflectance (Offset for clarity)
0.5
1.0
1.5
2.0
2.5
Wavelength (micron)
C
0.04
Goethite
50 cm
Alunite
Field
Reflectance (Offset for clarity)
0.5
1.0
1.5
2.0
2.5
Wavelength (micron)
D
0.04
Silica
Field
Reflectance (Offset for clarity)
0.5
1.0
1.5
2.0
2.5
Wavelength (micron)
E
0.08
Alunite
Goethite
50 cm
Field
Reflectance (Offset for clarity)
0.5
1.0
1.5
2.0
2.5
Wavelength (micron)
F
0.04
Kaolinite+Smectite
Hematite
Field
Reflectance (Offset for clarity)
0.5
1.0
1.5
2.0
2.5
Wavelength (micron)

Figure 13. Example field spectra from Telica volcano. Library spectra are scaled to match the general reflectance levels of field spectra as described in Figure 11. The jarosite and alunite spectra presented here may be Fe-rich natroalunite and natroalunite for reasons discussed in text. (A) Jarosite detection from the edge of the crater (right panel Figure 9). (B) Combination of jarosite and alunite family members, which are in the same mineral family from a float rock. (C) Goethite and alunite in an orange deposit near the crater rim (left panel Figure 9). (D) White surface deposit on a float rock measured as hydrated silica. (E) Goethite and alunite in a brown rim deposit near C. (F) Hematite and kaolinite+smectite identification from the surface of a red float rock.

of altered red or orange rocks, as thin coatings (Figure 8 to Figure 10), and sometimes in sediments (Figure 7 to Figure 10). The iron oxides on rocks were generally several meters from active fumaroles, but some goethite was identified close to the high temperature Cerro Negro vents. There were a number of spectra that exhibited the broad wavelength features of iron oxides but did not match either hematite or goethite. Feroxyhite was a good fit two of these unknown spectra. This mineral frequently forms on the ocean floor, but can also result from the rapid oxidation of Fe^{2+} in iron-rich waters [*Carlson and Schwertmann*, 1980], which is consistent with Cerro Negro alteration conditions.

2.4.1.3 Phyllosilicates

Four types of phyllosilicates were identified at the four Nicaraguan field sites: kaolinite, a general, smectite, montmorillonite, and saponite. Al-phyllosilicates have bands in the 2.2 μm region due to the Al-OH bonds, but they vary slightly in shape, which is how specific clays can be distinguished [*Clark et al.*, 1990; *Ehlmann et al.*, 2009b]. Pure kaolinite was identified using the characteristic doublet band around 2.2 μm (Figure 12C). A kaolinite and smectite mixture was identified based on the asymmetrical band shape in the 2.2 μm region that results from mixing of the kaolinite doublet and flatter smectite spectrum in that area (Figure 11F; Figure 12E; Figure 13F; Figure 14D) [*Clark et al.*, 2007b]. Montmorillonite has a distinct singlet band at 2.2 μm (Figure 14B). Fe/Mg-smectites have metal-OH bands around 2.3 μm. Our spectra are

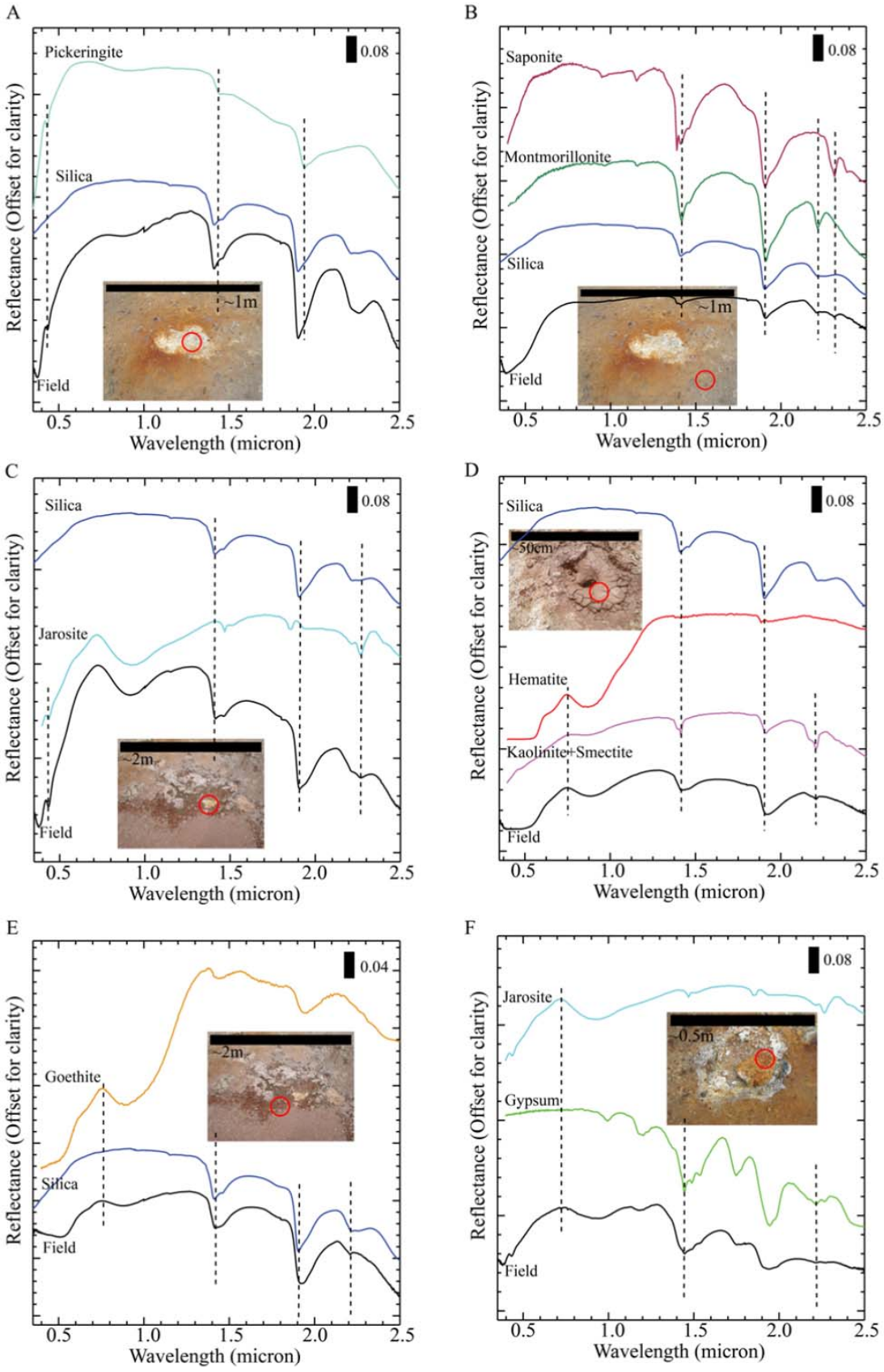
A
Pickeringite
0.08
Silica
~1m
Field
Reflectance (Offset for clarity)
0.5
1.0
1.5
2.0
2.5
Wavelength (micron)
B
Saponite
0.08
Montmorillonite
Silica
~1m
Field
Reflectance (Offset for clarity)
0.5
1.0
1.5
2.0
2.5
Wavelength (micron)
C
Silica
0.08
Jarosite
~2m
Field
Reflectance (Offset for clarity)
0.5
1.0
1.5
2.0
2.5
Wavelength (micron)
D
Silica
0.08
~50cm
Hematite
Kaolinite+Smectite
Field
Reflectance (Offset for clarity)
0.5
1.0
1.5
2.0
2.5
Wavelength (micron)
E
0.04
~2m
Goethite
Silica
Field
Reflectance (Offset for clarity)
0.5
1.0
1.5
2.0
2.5
Wavelength (micron)
F
0.08
Jarosite
~0.5m
Gypsum
Field
Reflectance (Offset for clarity)
0.5
1.0
1.5
2.0
2.5
Wavelength (micron)

Figure 14. Example field spectra from the San Jacinto Mudpots on the flank of Telica volcano. Library spectra are scaled to match the general reflectance levels of field spectra as described in Figure 11. (A) Possible match to pickeringite (CRISM Pickeringite LASF54A), with additional hydrated silica from the white deposits of an area with rings of color alteration (top right panel Figure 10). (B) Identification of the brown material for the same location is a mixture of montmorillonite (USGS Montmorillonite SAz-1), saponite (USGS SapCa-1.AcB) with hydrated silica. (C) Detection of jarosite (or potentially Fe-rich natroalunite, see text), slightly depressed by mixing with hydrated silica in a yellow deposit (bottom left panel Figure 10). (D) Combination of kaolinite+smectite clay, hematite, and hydrated silica to explain the spectra of a fresh mud (bottom right panel Figure 10). (E) Spectrum with goethite and hydrated silica from a redder region near the spectrum from C. (F) Jarosite and gypsum surface coating of a rock.

largely devoid of this feature, but in a few clay spectra there is a shoulder or small band at 2.3 μm that most closely matches saponite (Figure 14B and D). The clays were detected in two types of environments, ambient temperature rock coatings from surface-vapor interactions and warm, moist soils experiencing diffuse vapor emission. Phyllosilicates had a wide range of colors in the field including brown, grey, orange, and red (Figure 10). All four field sites had kaolinite+smectite, but montmorillonite and saponite were only seen at the Mudpots, and restricted to brown and white-yellow alteration products.

2.4.1.4 Miscellaneous

Instances of bright yellow elemental sulfur deposits were found at Cerro Negro and Momotombo (Figure 12A) close to the vents of active gas emissions (Figure 7; Figure 8). Sulfur is identified by a sharp brightening edge at 0.4 μm followed by a flat spectrum. The yellow deposits were often identified as pure sulfur, but with additional hydration bands (Figure 12A), possibly suggesting some mixing of hydrated silica or condensed water on the surface, although other water bands were not present. Momotombo displayed the most S^0-rich deposits with large expanses of pure yellow sulfur blanketing much of the interior crater walls.

Hydrated silica was abundant at all of the field sites (Table 2; Figure 12B; Figure 13D) and formed in the lowest pH, highest temperature, concentrated vents, as well as, in broader

deposits near diffuse vapor emission. It was identified by hydration bands at 1.4 and 1.9 μm, along with a broader band at ~2.25 μm. The field spectral band positions and widths matched that of siliceous sinter [*PDS Geosciences Node and CRISM Spectral Library Working Group*] and opal [*Clark et al.*, 2007b], suggesting a hydrated, amorphous silica phase. Most field spectra collected at all sites had a ~2.25 μm band that we attribute to some amount of hydrated silica within the sample. Yet the spectra of a few white sinter-like deposit (Figure 7) and rock coatings (Figure 8; Figure 10) matched a pure hydrated silica endmember.

We also measured pristine basalts at each site. These rocks were generally very dark and required longer measurement times. They were characterized by low reflectance, relatively flat spectra with a broad band around 1.0 μm or a decreasing slope to high wavelength. General basalt, basaltic andesite, or mafic library spectra were the best matches. Some hand samples had macroscopic phenocrysts, but the crystals did not compose a large enough area for a noticeable contribution to the spectra. A few rocks were an exception to this and augite was detectable.

2.4.2 Comparison of Nicaraguan Field Sites

To characterize the spatial occurrence of alteration minerals at all sites, we determined the occurrence of each individual mineral as a relative percentage to the other minerals. This method gave us a first order estimation of mineral frequencies to compare the sites. However, it does have the potential to be biased towards minerals that are easily identified, such as clays and gypsum with very distinct spectral bands, or affected by sampling bias, such as limited access to the field site. There is also the potential that minerals can mask others in mixture, which could bias these relative frequencies. Additionally mineral coatings can mask the bulk composition of a sample. The results discussed suggest certain environmental controls on mineral formation from acid-sulfate alteration, but future work is needed to resolve the above issues.

While all of the field sites shared similar alteration mineralogies, the variety of minerals within the classes and the frequencies of individual minerals varied (Table 2). We find that Cerro Negro and Momotombo had the greatest mineral variety within each mineral class with five types of sulfates, four oxides/hydroxides, and two clays present at these sites. Telica has the least mineralogic variety with three sulfates, one oxide/hydroxide, and two clays, although the fewest data were collected at Telica. The San Jacinto Mudpots have moderate diversity, but also exhibit additional clay phases not identified at the other sites. Hydrated silica is ubiquitous at all of the sites (Figure 11B-C and E; Figure 12A-C; Figure 13D; Figure 14A-E), while elemental sulfur is only present at Cerro Negro and Momotombo.

2.4.2.1 Cerro Negro

Approximately 60 spectra samples were taken at Cerro Negro along the 1992 crater wall and the 1995 crater rim. We sampled the variety of alteration settings, including within fumarolic vents and radially outward through their aprons, encrustations, rock coatings, hot soils with diffuse outgassing, inactive fumaroles, and within evaporitic outwash basins. Cerro Negro has the greatest occurrence and diversity of sulfate and iron oxide/hydroxide minerals (Table 2). The major secondary minerals at this site determined from VNIR reflectance spectroscopy are gypsum (Figure 11A and C), hematite (Figure 11B), and goethite (Figure 11E and F). Minor minerals are hexahydrite (Figure 11B), natroalunite, Fe-bearing natroalunite, and sulfur. Finally the trace minerals include an Fe-sulfate (Figure 11C) and an iron oxide that could not be precisely identified. There are also trace mixtures of the Al-phyllosilicates kaolinite and smectite (Figure 11F).

At Cerro Negro there is a wide range of temperature (>100°C to ambient) and pH (<0 to 6.5). The lowest pH and highest temperatures generally correlate with the center portion of the

170 m crater wall and trend to less acidity and lower temperature towards the fringes (see Figure 4 in *Hynek et al.,* submitted). At fumaroles near the center of the crater wall with highest temperature and acidity, the main secondary minerals were sulfur and hydrated silica (Figure 7; Figure 11) at the vents and gypsum and silica extended down the aprons, consistent with the XRD mineralogy. Similar to the aprons, gypsum and silica dominated alteration mineralogy away from the central wall towards lower temperature and higher pH. In areas of more diffuse venting beyond focused vents, the alteration mineralogy identified in the spectra included hydrated silica, gypsum, and natroalunite (Figure 11C), consistent with detailed mineralogical analyses of altered deposits in these areas [*McCollom et al.,* submitted]. Rock surfaces directly downwind of active vents contained elemental sulfur. Hexahydrite was also identified in a few instances at the focused vents. Goethite was occasionally found on the moist top of vent structures, but it was more often observed with hematite on rock surfaces at ambient temperatures. Rock not currently interacting with vapors tended to have coatings of iron oxides and phyllosilicates. Iron minerals generally were spatially distinct from sulfates minerals, but a few samples had mixtures of gypsum and hematite or phyllosilicates and hematite. Enclosed basins with bathtub rings existed a few to ~10 m downslope of numerous fumaroles and outwash channels connecting them suggested transport and evaporation of alteration mineral. Spectroscopy measurements of this area only detected goethite, hexahydrite, and hydrated silica, but field XRD results showed a number of additional hydrated sulfates [*Hynek et al.,* submitted]. Finally, phyllosilicates found at Cerro Negro existed on rock surfaces along with iron oxides, likely from past fumarolic gas condensing on the basalts' surface. XRD also detected

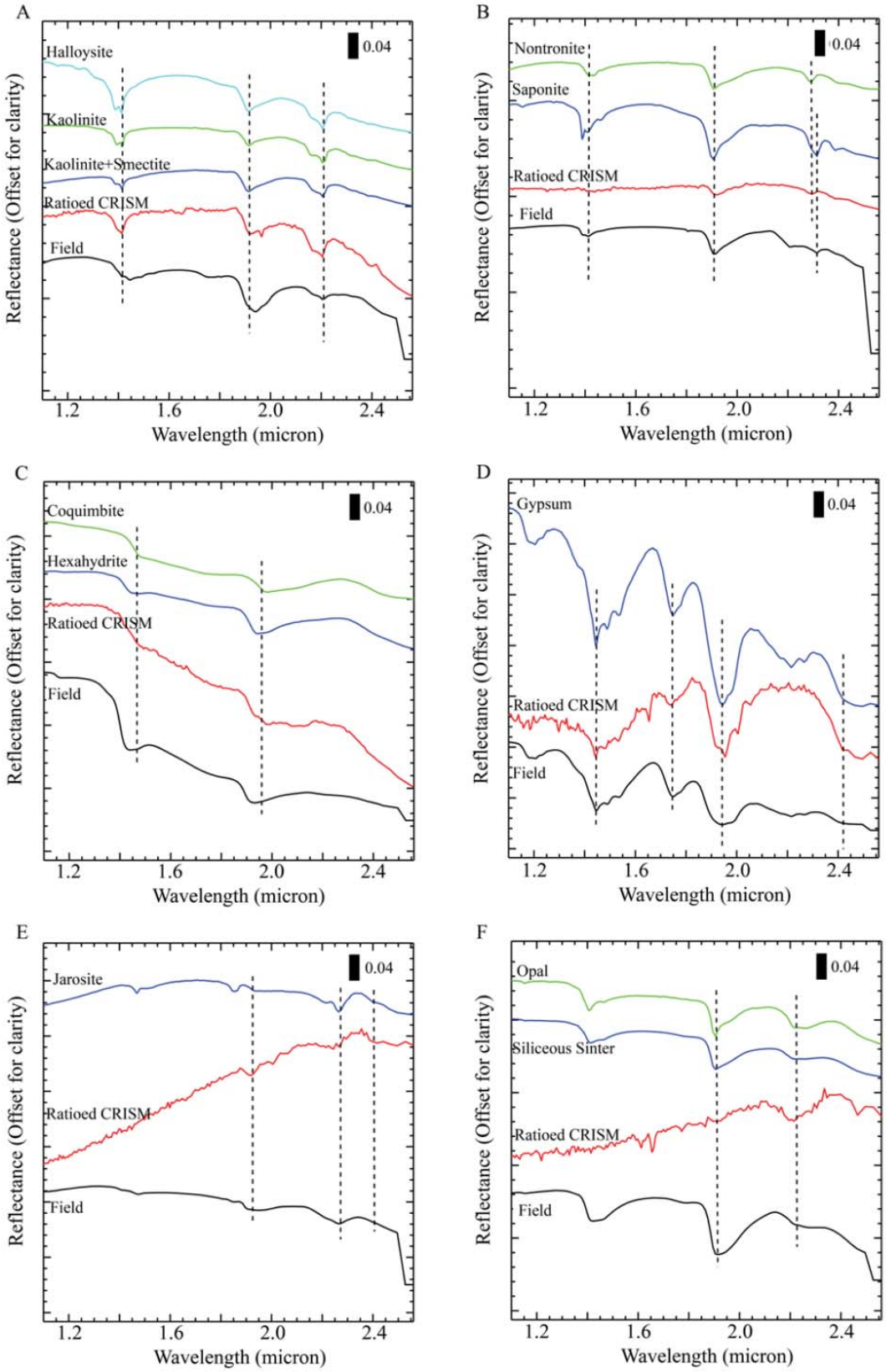
A
Halloysite
Kaolinite
Kaolinite+Smectite
Ratioed CRISM
Field
0.04
Reflectance (Offset for clarity)
1.2
1.6
2.0
2.4
Wavelength (micron)
B
Nontronite
Saponite
Ratioed CRISM
Field
0.04
Reflectance (Offset for clarity)
1.2
1.6
2.0
2.4
Wavelength (micron)
C
Coquimbite
Hexahydrite
Ratioed CRISM
Field
0.04
Reflectance (Offset for clarity)
1.2
1.6
2.0
2.4
Wavelength (micron)
D
Gypsum
Ratioed CRISM
Field
0.04
Reflectance (Offset for clarity)
1.2
1.6
2.0
2.4
Wavelength (micron)
E
Jarosite
Ratioed CRISM
Field
0.04
Reflectance (Offset for clarity)
1.2
1.6
2.0
2.4
Wavelength (micron)
F
Opal
Siliceous Sinter
Ratioed CRISM
Field
0.04
Reflectance (Offset for clarity)
1.2
1.6
2.0
2.4
Wavelength (micron)

Figure 15. Comparison of Nicaraguan field, Mars CRISM, and Library VNIR spectra. CRISM spectra were produced by ratioing regions of interest by spectral flat areas from scene that had been atmospherically corrected. Regions of interest were directed by previous studies. CRISM scenes used were (A-C) frt000096ee [*Thollot et al.*, 2012], (D) frt0007d87 [*Wray et al.*, 2011], (E) frt0000a425 [*Farrand et al.*, 2009], (F) frt00010628 [*Skok et al.*, 2010]. CRISM and field spectra were scaled by 5 (A-C) and 3 (E-F) and only Mars was scaled by 5 (D) for ease of comparison. (A) Example of Al-phyllosilicates (Kaolinite KL502, Halloysite CM13). Similar band shape in the 2.2 μm region makes it difficult to distinguish specific mineral. (B) Example of Fe/Mg-smectite. Mars spectrum is slightly shifted towards nontronite (Nontronite NG-1.a), while field spectra is matched to saponite. (C) These phyllosilicates are in situated near a Fe/Mg-polyhydrated sulfate, which are hard to distinguish. Fe-sulfate, coquimbite (Coquimbite BKR1JB621A) fits Mars spectra slightly better, but hexahydrite as found in the field is also a possibility. (D) Gypsum example. These spectra can be much harder to distinguish on Mars than Earth. (E) Jarosite spectral sample. Mars jarosite mineral family members are also hard to identify. (F) Hydrated silica comparison. Broad 2.25 μm features identify the deposit as a silica mineral (Opal Tm8896).

phyllosilicates closer to fumaroles at elevated temperature and acidic conditions that were not discernible in VNIR measurements.

2.4.2.2 Momotombo

Fifty spectra were collected from within the heavily altered summit crater of Momotombo, which exhibited the lowest pH (down to -1) and highest temperatures (>>100°C) of all the field sites. For safety reasons, samples were not collected near the most active vents and a number of float samples were measured, in addition to soils interacting with diffuse gassing regions. Momotombo had a similar degree of mineral diversity as Cerro Negro (Table 2), but was dominated by hydrated silica (Figure 12A-C) and sulfur (Figure 12A). A number of other minerals were detected with VNIR in much lower spatial concentrations. Minerals in relatively minor occurrences are: gypsum (Figure 12D), natroalunite (Figure 12E and F), hematite (Figure 12C and E), goethite (Figure 12D and F), and the unknown 0.43 μm Fe-sulfate. Trace minerals include Fe-bearing natroalunite, pickeringite, kaolinite (Figure 12C), kaolinite+smectite (Figure 12E), and a general iron oxide.

The sulfur and hydrated silica were concentrated in the hotter, S-rich interior of the crater consistent with the XRD results of samples from those areas [*Hynek et al.,* submitted]. A number of float samples were measured at Momotombo with abundant gypsum, likely transported from vent aprons. Tens of meters away from the active vents, several rocks at Momotombo displayed classical spheroidal weathering (Figure 8). Yet despite distinct layering, the alteration was mainly hydrated silica mixed with goethite, hematite, or natroalunite, although no mineralogical trend was obvious from the interior to the surface. Compositional data from XRF confirmed that most elements were previously leached away, leaving silica [*Hynek et al.,* submitted]. In fine, moist soils along the cooler edges of the summit crater, we identified Al-phyllosilicates that were red in color and indicative of the presence of hematite as well. These soils were at ambient temperatures, but may have been areas of high temperature alteration in the past.

2.4.2.3 Telica

Telica volcano had the lowest mineral diversity; however, only 10 samples were collected from the rim of the crater (Table 2) and we were unable to access most sites of active venting. The greatest spatial frequencies of alteration mineralogy had spectral identifications matching members of the alunite (Figure 13B-C and E) and jarosite (Figure 13A-B) families, which for reasons discussed below are likely natroalunite and an Fe-rich natroalunite, respectively. Along with goethite (Figure 13C and E), these two minerals were categorized as the major minerals. Kaolinite+smectite, hematite (Figure 13F) and the 0.43 μm Fe-sulfate were present in minor quantities.

The fewest samples were analyzed at Telica due to accessibility. Rock patches of heavy alteration occurred in a limited number of areas along the very edge of the rim, which had minor

interaction with volcanic gas (Figure 9). These were identified as Fe-bearing natroalunite, natroalunite, and goethite. More distant from the rim was a field of ejected boulders. Rock downwind of the volcano and in topographic lows had surface alteration expressions of Fe-bearing natroalunite, natroalunite, and goethite. Trace kaolinite+smectite and hematite were also observed on the rocks. Field XRD also detected montmorillonite at Telica [*Hynek et al.,* submitted].

2.4.2.4 San Jacinto Mudpots

The final field site, which is part of the Telica volcano complex, had the most uniform spatial distribution of alteration minerals, i.e. many minerals at similar occurrences (Table 2). About 20 samples were collected at this site. Goethite was the only mineral classified widely observed (Figure 14E). The minor minerals include gypsum (Figure 14F), Fe-bearing natroalunite (Figure 14C and F), hematite (Figure 14D), kaolinite+smectite (Figure 14D), montmorillonite, and saponite (Figure 14B). Pickeringite (Figure 14A), which was unique to the Telica complex, the unknown 0.43 μm Fe-sulfate, and the rare feroxyhite are trace minerals at this site.

Three types of areas were measured at this site: 1) a rock wall with diffuse steam, 2) bubbling mudpots, and 3) dry, hard ground with multiple zones of alteration (Figure 10). The rock wall was largely red rocks with fissures that allowed steam to escape and consisted of primary material, hematite, goethite, kaolinite+smectite, and montmorillonite. The wet muds next to thermal springs contained kaolinite+smectite and hematite. Finally the hard, zoned surfaces, representative of relic fumaroles and mudpots exhibited hematite and goethite with some indication of Fe-bearing natroalunite, gypsum, and montmorillonite. Clays were a more

dominant phase at these locales, consistent with XRD results [*Hynek et al.,* submitted]. XRD also detected additional hydrated sulfates not detected with VNIR.

2.5 Discussion of Field site Results

The hydrothermal areas studied here all have minerals representative of three mineral groups: 1) sulfates (gypsum, Fe-bearing natroalunite, natroalunite, hexahydrite, pickeringite, Fe-sulfate), 2) oxides/hydroxides (hematite, goethite, iron oxide), and 3) phyllosilicates (kaolinite, kaolinite+smectite, montmorillonite, saponite). However, the frequency and variety within each mineral family is different between the field areas. Hydrated silica is also widespread; as is sulfur at Momotombo. The distribution of alteration minerals suggests that there is not a distinct mineral assemblage unique to a single volcanic hydrothermal area.

The universal feature in all field spectra is hydration. The 1.4 and 1.9 μm water bands are prevalent in almost every spectrum. Structural hydroxyl (-OH) is largely responsible for the feature around 1.4 μm, while structural or adsorbed water (H_2O) produces the 1.9 μm band [e.g. *Clark et al.*, 1990; *Bishop et al.*, 2008b]. These features are expected in phyllosilicate spectra even in areas of high temperature, since experimental results demonstrate that phyllosilicates do not begin to dehydrate or dehydroxylate until ~400°C with weak features often present until 900°C [e.g. *Gavin and Chevrier*, 2010; *Che and Glotch*, 2012]. The water bands were unexpected in the elemental sulfur samples (Figure 12A) and may represent adsorbed water since these samples were always near active venting. Furthermore, the doubly hydrated form of Ca-sulfate, gypsum, is found throughout our sites despite anhydrite being predicted in models due to the high temperature [*Marcucci and Hynek,* submitted; *McCollom et al.*, submitted]. Variable temperature gradients may allow areas of lower temperature for gypsum formation or gypsum might form as a metastable mineral. When the stronger 1.4 and 1.9 μm bands are seen with an

additional broad band at 2.25 μm, it is indicative of hydrated silica. This can be a pure mineral or a phase mixed with another mineral class, such as hematite (e.g. Figure 11B).

Mineral mixing occurs in a number of ways that can affect the resulting spectrum [*Clark*, 1999]. In linear mixing, when light photons react with a single material before returning to the detector, the individual mineral spectra can be added together to form the mixture spectrum. However, smaller spots sizes and VNIR wavelengths more often lead to detections of intimate mixtures, which results in a photon reacting with multiple materials before reaching the detector. The result is a non-linear mixture of the individual spectra. Therefore, while minerals in the mixture can be identified from different portions of the mixture spectrum, they cannot easily be deconvolved into relative abundances. Models have been applied to Mars observations [*Poulet and Erard*, 2004; *Poulet et al.*, 2008a], but due to complexity and remaining uncertainty in the solutions, we did not employ them here. Another form of mixing occurs when one mineral dominates the spectrum and masks the other minerals present. This has been shown in different studies and often occurs with iron minerals [*Cloutis et al.*, 2006; *Farrand et al.*, 2009; *Dehouck et al.*, 2012]. Iron-bearing minerals were widespread at our field sites and could have masked other mineral signatures. This may account for some diversity differences between the VNIR study and the XRD study [*Hynek et al.,* submit] since the water bands from the hydrated silica overlap with the more complex bands of gypsum. This type of masking evident in Figure 11C, where the mineral identified is gypsum, but it is expected from detailed chemistry [*McCollom et al.,* submitted] that hydrated silica should also be abundant here. Similarly, members of the alunite-jarosite mineral families have comparatively weak hydration bands that would be obscured if gypsum were present. Mineral masking also occurs when mineral coatings obscure

the bulk rock composition. This can add uncertainties into mineral identifications and, in particular, relative frequencies.

Mineral identification can also be hampered by cation substitution. The alunite and jarosite mineral families are a similar structure, but Fe^{3+} is replaced with Al^{3+} in the alunite minerals. Each contains K^{+}, but this can have substitution by H_3O^{+} (hydronium-) or Na^{+} (natro-). Field spectra collected indicated both jarosite and alunite, which are spectrally distinct from each other; however, natro-versions are only subtly different from their potassium endmembers [*Bishop and Murad*, 2005]. Based on laboratory experiments and minerals predicted in geochemical models, natroalunite is an expected product of plagioclase dissolutions in the Cerro Negro environment [*Marcucci and Hynek,* submitted; *McCollom et al.*, 2013]. Additionally, samples collected at Cerro Negro during previous field campaigns demonstrated the presence of natroalunite and Fe-rich natroalunite, while jarosite is rare [*McCollom et al.*, submitted]. The libraries used for identification had examples of endmember alunite, jarosite, and natrojarosite, but not natroalunite or solid solution of this mineral group. The similarity between natroalunite and alunite and previous data suggest that the alunite identified in field spectra was most likely natroalunite. Also since laboratory studies show that jarosite is rare at Cerro Negro, the jarosite signatures seen here may in fact be an Fe-rich natroalunite. While a comparison of VNIR spectra of this solid solution has not been done, Mössbauer spectra are similar for jarosite and Fe-rich natroalunite [*McCollom et al.*, 2013].

A feature that has not been conclusively identified is a sharp, but shallow absorption near 0.43 μm (Figure 11C). This is likely the result of the Fe^{3+} spin-forbidden transition [*Cloutis et al.*, 2006] and a prominent feature in most Fe-sulfates, such as in the jarosite mineral family. Some field samples displayed this feature, but the spectra did not have longer wavelength

features associated with members of the jarosite family or any other Fe-sulfate in the spectral libraries. This could be due to mineral mixing or the presence of a mineral that is not included in the spectral libraries. These spectra were generally classified as an unidentified Fe-sulfate. Because the feature is a result of Fe^{3+} in the mineral, it could also be a ferric oxide. However, iron oxides do not tend to exhibit this feature and they have relatively flat spectra in the longer wavelength range. Ferric oxide and hydroxide minerals, such as hematite or goethite, have broad iron bands around 0.9 μm and a flat long wavelength spectrum. The pattern suggests the unidentified 0.43 μm spectral dip represents an Fe-sulfate. *Hynek et al.* [submitted] found minor fibroferrite ($Fe_2(SO_4)_3$ and melanterite ($FeSO_4 \cdot 7H_2O$) that may account for this spectral signature.

There has been a noticeable lack of Mg alteration products in results from field campaigns. The primary rocks have significant Mg (Table 1 in *Hynek et al., submitted*), but Mg-sulfates have been largely absent. At Cerro Negro a comparison of cation abundance shows that alteration is depleted in Mg and enriched in Ca with respect to unaltered material [*Hynek et al.*, 2011]. Experiments showed abundant Mg-sulfate formed solely as an evaporitic phase in pyroxene experiments [*Marcucci and Hynek,* submitted]. A Mg-sulfate—hexahydrite—was identified during this campaign in an outwash basin at Cerro Negro. The highly soluble nature of the Mg-sulfates likely results in them being largely washed away or flushed into the drainage areas where they re-precipitate when the water evaporates. Since Mg-sulfates are readily dissolved by water, they could be indicators of the amount of precipitation or reworking by water for Martian deposits.

Phyllosilicates were a major component of alteration mineralogy at all of the sites we studies, specifically Al-rich kaolinite and montmorillonite indicated by a 2.2 μm Al-OH band. A

small 2.3 μm band suggests minor amount of an Fe/Mg-smectite, saponite, may also be present (Figure 14B and D). Experimental studies have shown that Al-phyllosilicates are generally more resistant to weathering in acidic or high temperature environments given the strong Al-OH bond [*Altheide et al.*, 2010; *Gavin and Chevrier*, 2010; *Daly et al.*, 2011]. Additional studies examining the weathering of phyllosilicates in acidic solutions found that an Fe-smectite weathered quickest in the acidic solutions, while increased Al abundance increased the weathering resistance [e.g. *Eberl and Hower*, 1975; *Amram and Ganor*, 2005; *Altheide et al.*, 2010]. Furthermore, experimental and field studies show that Al-phyllosilicates, such as kaolinite and halloysite, frequently form in acidic, hydrothermal areas [e.g. *Fialips et al.*, 2000; *Ece et al.*, 2008; *Fernández-Remolar et al.*, 2011]. This is consistent with the bulk of Nicaragua phyllosilicates we identified being Al-rich kaolinite. However, another consideration is composition; the Nicaragua rocks are richer in Al then either Fe or Mg, which influences secondary mineralogy. Small but detectable amounts of Fe/Mg-smectites were found at our field sites, indicating that minor Fe-rich clays can form in acidic conditions. Based on the evidence at these field sites, we support that the dominance of Al-phyllosilicates over Fe/Mg-smectites is largely due to the enhanced Al-phyllosilicate formation in hydrothermal, acidic conditions. However, gradients in the environmental conditions allow for the formation of Fe/Mg-smectites in the same vicinity. If the composition of the Nicaraguan rocks was richer in Fe, we would expect to see a greater presence of Fe-smectites at our field sites, but still less than Al-phyllosilicates.

In general, each of the four sites had minerals representing each of the three main categories listed above—sulfates, phyllosilicates, and oxides/hydroxides—but variability within those categories (Table 2). Of the four sites, Cerro Negro and Momotombo had the most variety

of alteration minerals followed by the San Jacinto Mudpots, and then Telica. The main control of secondary mineralogy in acid-sulfate alteration reactions was primary mineral composition. This supports results of experiments [*Marcucci and Hynek,* submitted; *Tosca et al.,* 2004] and iron-dominated alteration mineralogy at Rio Tinto [*Fernández-Remolar et al.*, 2005]. In the Nicaraguan field sites the rock chemistries are largely comparable and may be a less influential factor of secondary mineralogy. Hence, other explanations for the variations we observed in the field are warranted, such as environment parameters pH, temperature, fluid:rock ratio. *Hynek et al.* [submitted] outlines five types of environments that can be distinguished with mineralogy and our VNIR study supports this conclusion. That paper also compared mineralogy determinations from VNIR with those from XRD on co-measured samples. Both techniques show that mineralogical variations occur on a meter-scale, which would not be identifiable from remote sensing instruments. To identify such environments on Mars, geological context and local mineralogical measurements would be needed.

2.6 Implications for Mars

This suite of alteration products from our study have many overlapping minerals with those identified globally on Mars by CRISM and OMEGA [e.g. *Gendrin et al.*, 2005; *Murchie et al.*, 2009b; *Ehlmann et al.*, 2011b; *Carter et al.*, 2013]. We can directly compare the VNIR spectra collected during this study to those seen on Mars (Figure 15). The TerraSpec4 instrument used in this study has a higher spatial resolution than the Martian datasets. This is further enhanced due to the noise contributed between field and orbiter measurements, such as spatial resolution and atmospheric contributions. Mars has deposits of Ca-sulfate, Mg-sulfate, and complex sulfates, like the jarosite family. Jarosite minerals are a particularly useful indicator of a drier, more acidic environment due to the low solubility of Fe. This mineralogy and

abundant amorphous silica is indicative of hydrothermal processes [e.g. this work and companion papers; *Schiffman et al.*, 2006; *Seelos et al.*, 2010; *Ruff et al.*, 2011]. While Martian sulfates, phyllosilicates, and oxides are often discussed separately, locations of sulfates mixed with phyllosilicates or iron oxides have also been documented [*Bibring et al.*, 2007; *Wiseman et al.*, 2008; *Wray et al.*, 2009b; *Fernández-Remolar et al.*, 2011]. When phyllosilicates are present in an area, they are often cited as an indicator for neutral to alkaline fluids. Furthermore, when phyllosilicates and sulfates are observed together, their sequence has often been used to suggest a changing environmental regime from more neutral to more acidic fluids. However, our work demonstrates that phyllosilicates may not be as robust of an indicator of formation conditions as previously thought.

As previously discussed, Al-phyllosilicates are generally more stable in low pH conditions and to a higher temperature then Fe/Mg-smectites. While Fe/Mg-smectites are more abundant on the Martian surface Al-phyllosilicates have also been found [e.g. *Ehlmann et al.*, 2009b, 2011b; *Carter et al.*, 2013] and both types have been seen in conjunction with sulfates [e.g. *Bibring et al.*, 2007; *Wiseman et al.*, 2008; *Farrand et al.*, 2009; *Wray et al.*, 2009b, 2010]. In particular the Noctis Labyrinthus, Mawrth Vallis, Valles Marineris, Meridiani Planum and Gusev crater are interesting places to compare to our field results since they contain sequences of Fe/Mg-smectites, Al-phyllosilicates, sulfates, and amorphous silica [e.g. *Anderson and Bell*, 2008; *Bishop et al.*, 2008b; *Lane et al.*, 2008; *Yen et al.*, 2008; *Farrand et al.*, 2009; *Wray et al.*, 2010; *Ruff et al.*, 2011; *Weitz et al.*, 2011; *Thollot et al.*, 2012].

Noctis Labyrinthus is located at the west end of the Valles Marineris rift and is part of the Tharsis volcanic region. It consists of closed and open basins that exhibit a number of mineral types. Studies of depressions and troughs showed a general bottom to top sequence of Al-

phyllosilicates, Fe/Mg-sulfates then Fe/Mg-smectites [*Weitz et al.*, 2011; *Thollot et al.*, 2012] (Figure 15A-C). This stratigraphic sequence is the reverse of the global alteration trend that generally shows Fe/Mg-smectites overlaid by Al-clays that is thought to be a testament to early neutral conditions that became progressively more acidic. Specifically, the lowest unit was likely halloysite or kaolinite [*Weitz et al.*, 2011; *Thollot et al.*, 2012]. This spectral identification is similar to the kaolinite mixed with smectite we saw in Nicaragua (Figure 15A). Associated sulfate deposits exist at slightly higher elevations. Polyhydrated sulfates most consistent with coquimbite, monohydrated sulfates consistent with szomolnokite and kieserite, and hydroxylated sulfates consistent with jarosite were observed. At our field sites we observed hexahydrite, which has similar spectral properties to coquimbite (Figure 15C), and jarosite. The highest layer was suggested to be nontronite, an Fe-smectite [*Thollot et al.*, 2012]. In our study, we observed a 2.3 μm band most consistent with saponite (Figure 15B). The presence of Fe or Mg in smectites subtly shifts the 2.3 μm band and it can be hard to distinguish on Mars. Two amorphous opaline deposits that may contain Fe-oxide/hydroxide minerals have been observed with this Fe-smectite unit. Such deposits often form as weathering rinds or leached sinters in volcanic areas. The uppermost portion of this layer also appears to be mixed with a jarosite-family mineral.

Two mechanisms have been suggested to explain this sequence, local aqueous activity that was the reverse of global trends [*Weitz et al.*, 2011] and warm, acidic groundwater circulation [*Thollot et al.*, 2012]. In the former, the area would have experienced periodic influxes of water with varying conditions that promoted the formation of different minerals. The uppermost layers could be lacustrine deposits or alteration of volcanic ash [*Weitz et al.*, 2011]. In the latter, upward circulating fluid would precipitate Al-phyllosilicates at the near-surface and

the freezing/evaporitic conditions of the surface would precipitate sulfates. The upward progression through added volcanic airfall or eolian layers would neutralize fluids for the precipitation of Fe-smectite. Periodic increases in or spatial closeness to hydrothermal fluid could have created the high elevation jarosite-like deposits [*Thollot et al.*, 2012]. Given our findings of all the products in this sequence co-located in volcanic environments, we suggest that local hydrothermal activity at Noctis Labyrinthus could have produced the complete sequence of mineralogy found there. This is similar to the *Thollot et al.* [2012] model where the system is driven by hydrothermal activity and there is no input from global climate trends. However, we argue that evaporation is unnecessary for the formation of sulfates because low fluid:rock ratios at a hydrothermal area are sufficient for their precipitation. Additionally, the position of Noctis Labyrinthus on the Tharsis rise is similar to the location of the San Jacinto Mudpots on the flank of Telica Volcano. The mudpots are characterized by shallow hydrothermal circulation that penetrates the surface in diffuse fumaroles and our field site contains the same minerals observed at this depression in Noctis Labyrinthus.

Terra Sirenum is a cratered highlands area situated south of the Tharsis rise. Exposures of alunite, jarosite, gypsum, Mg/Fe-sulfates, Al-phyllosilicates, Fe/Mg-phyllosilicates, and chlorides have been observed in this area [*Glotch et al.*, 2010; *Wray et al.*, 2011; *Ruesch et al.*, 2012]. The primary difference between the gypsum spectra observed in the field and on Mars is the detail to which the triplet and doublet are seen (Figure 15D; Table 1); therefore, the 1.76 μm singlet band is often the best indicator of gypsum on Mars. The sulfates and Al-phyllosilicates compose the main mineralogy at craters, while chlorides and Fe/Mg-smectites occur largely in the cratered plains [*Wray et al.*, 2011]. This may suggest an impact-induced hydrothermal influence on secondary mineralogy. Alunite has been observed in association with silica-rich

material, either montmorillonite or hydrated silica, and Al-phyllosilicate, either kaolinite or halloysite at Cross crater in this region [*Swayze et al.*, 2008]. This mineral deposit is also situated near lava flows. Two mechanisms have been suggested are an acid-sulfate hydrothermal system or low temperature evaporitic lake, which has been favored [*Swayze et al.*, 2008; *Baldridge et al.*, 2009; *Glotch et al.*, 2010; *Wray et al.*, 2011]. *Swayze et al.* [2008] support the lake environment hypothesis based on the spectral features of alunite. In lower temperatures, 1.43, 1.76, 2.21, and 2.32 μm bands are weaker compared to high temperature formation, which was suggested to be more consistent with the Terra Sirenum alunite spectrum. However, our field sites demonstrated weakening in those alunite bands when mixed with iron minerals, particularly jarosite family minerals or goethite (i.e. Figure 12F; Figure 13C and E). This further supports the previous discussion (Section 5) that solid solution mixtures of the alunite-jarosite mineral families affect VNIR spectra. Additionally the resolution of Mars spectral observations is much less compared to Earth field and laboratory spectral samples. It would be hard to distinguish such spectral changes in the Martian data, especially if other minerals or dust was present. Thus the weakened spectral bands attributed to lower formation temperature could be effects of mixing and the alunite family mineral was formed in a high temperature hydrothermal system.

The most aerially extensive sulfates observed to date occur in the layered deposits of Valles Marineris [e.g. *Chojnacki and Hynek*, 2008]. Valles Marineris is a giant rift valley that likely experienced hydrothermal activity, like similar rift zones on Earth [e.g. *Tiercelin et al.*, 1993]. This area hosts monohydrated sulfates, polyhydrated sulfates, Al-phyllosilicates, Fe/Mg-smectites, and amorphous silica that have been detailed in individual chasmata papers [*Bishop et al.*, 2009; *Flahaut et al.*, 2010; *Lichtenberg et al.*, 2010; *Roach et al.*, 2010b]. For the purpose of

this paper, we will not detail every instance of aqueous alteration, but will relate the trends of mineralogy in the context of our field results. Deep Fe/Mg-phyllosilicates are widespread in Valles Marineris with Al-phyllosilicates at higher elevations [*Murchie et al.*, 2009a; *Ehlmann et al.*, 2011b]. In general, potential polyhydrated mineral identifications include Mg-sulfates, starkeyite, epsomite, hexahydrite, and melanterite, and Fe-sulfates, copiapite, ferricopiapite, and halotrichite [*Gendrin et al.*, 2005; *Bishop et al.*, 2009]. Gypsum and kieserite are also present [*Gendrin et al.*, 2005]. *Bibring et al.* [2007] found Fe-sulfates and Fe-oxides/hydroxides/oxyhydroxides in close association with each other in Capri and Candor chasmata. The presence of hydroxylated ferric sulfate and hydrated silica have been observed in the region around Juventae Chasma [*Bishop et al.*, 2009]. These pieces of evidence, as well as, the geological context suggest that areas in Valles Marineris experienced hydrothermal activity. Similar to our Nicaraguan field sites, layered deposits are dominantly sulfates then phyllosilicates and iron oxides/hydroxides. The opening of Valles Marineris likely caused hydrothermalism, as does rifting on Earth, that would have formed these minerals [e.g. *Tiercelin et al.*, 1993]. There may have been localized vents that correspond to the interior layered mounds. A distinct difference between our field sites and Valles Marineris is the dominance of Fe- and Mg-sulfates on Mars over Ca-sulfates in Nicaragua. This could be attributed to parent lithology differences and less precipitation on Mars to remove Fe- and Mg-sulfates, which are more soluble than Ca-sulfates.

Mawrth Vallis is a large outflow channel area that experienced ample aqueous activity. The channel and surrounding plains have a representative sequence of the Al-phyllosilicates over Fe/Mg-smectites [*Bishop et al.,* 2008a]. The large extents of phyllosilicates in this area have suggested that it experienced more neutral conditions early in Mars' history [*Bibring et al.,*

2006]. However, there are isolated instances of sulfate minerals that may indicate potential localized hydrothermal activity. *Farrand et al.* [2009] found an isolated deposit of jarosite mineral type in Mawrth Vallis, surrounded by plains of Al- and Fe/Mg-phyllosilicates. Jarosite is an indicator or acidic environments and mineral family members are present at our field sites (Figure 15E). Additional spectral characteristics of the jarosite family deposit are consistent with mixed ferrihydrite, an iron oxyhydroxide. The jarosite deposit has a similar texture to the base Fe/Mg-smectites and appears to lie below the Al-phyllosilicates, suggesting the alteration of Fe/Mg-smectites to jarosite in acid-sulfate weathering [*Farrand et al.,* 2009]. A similar mechanism could explain the minor amounts of Fe/Mg-smectite we observed in Nicaragua. The depression is suggested to have held water that collected volcanically sourced sulfur-rich material; subsequent evaporation precipitated the jarosite and other Fe-minerals [*Farrand et al.,* 2009]. Alternatively, this depression could be a remnant crater and the jarosite was formed during impact-induced hydrothermal activity. This hypothesis was largely disregarded due to the lack of similar observations at other impact craters. However, we found that gypsum and silica dominate our field sites and may often mask the spectral signatures of other minerals present. This Mawrth Vallis location may be a unique hydrothermal area where other minerals can be seen remotely. The jarosite mineral family detection near Al-phyllosilicates akin to those identified in this study is also suggestive of hydrothermal formation.

In northern Meridiani Planum there are sequences of phyllosilicates and sulfates that suggest the sulfates are older than the phyllosilicates [Anderson and Bell, 2008]. The pattern of widespread sulfates with isolated areas of phyllosilicates is consistent with our hydrothermal field mineralogy. In our extreme to moderate acidic field locales, we found a number of phyllosilicates forming in conjunction with sulfates and iron oxides. While not as abundant as

the sulfates, the phyllosilicates were present at all sites and clearly detectable with VNIR reflectance spectroscopy. We identified only minor Fe/Mg-smectites, but abundant Al-smectites. This suggests that some mixed sulfate-phyllosilicate deposits, particularly Al-rich ones, observed on Mars could represent acidic hydrothermal environments similar to those documented in this study.

This work also has implications for the areas of high silica content that have been observed in several places on Mars, including near Syrtis Major and Home Plate in Gusev crater. Hydrated silica has been detected directly associated with vent structures in the Syrtis Major area using CRISM data [*Skok et al.*, 2010]. The suggested formation mechanisms are hot spring-type deposits from volcanic groundwater, a Si-rich magma that causes precipitation of silica minerals from vapor emissions, or a low temperature acid-fog. Based on our fieldwork, we would suggest a fourth option that acidic, high temperature vapor emissions leach cations from vent rocks creating a Si-rich lag. In the field, we see abundant silica in precipitated deposits and leached weathering rinds (Figure 15E). The Syrtis Major cones may be most like Momotombo, which has had the greatest duration of alteration. The mineralogy at Momotombo is dominated by hydrated silica. Since hydrated silica is the major alteration phase at our field sites, we expect that they would look similar to the Syrtis Major vents from CRISM-like orbiter data. This suggests that Mars orbiter measurements may not be able to detect the much more diverse mineralogy that likely exists at the surface.

Home Plate is proposed to be the site of a hydrothermal environment based on chemical and morphological results [*Squyres et al.*, 2007; *Yen et al.*, 2008; *Ruff et al.*, 2011]. In this area soil and rock that have 65-92 wt % silica have been observed by the Spirit rover [*Ruff et al.*, 2011]. The Paso Robles soil class also has a high silica content, but additional Fe- and Mg-

sulfates [*Lane et al.*, 2008; *Yen et al.*, 2008]. However, amorphous silica deposits can form via precipitation in a hot spring, precipitation from Si-rich vapors, or fumarolic gas surface alteration. *Yen et al.* [2008] suggested that sulfur-rich volcanic gas and hydrothermal fluids altered local bedrock forming amorphous silica and hydrated Fe- and Mg-sulfates. The abundant amorphous silica and sulfates at our field sites support this conclusion. A key difference is the resultant sulfates. Home Plate has abundant Mg-sulfates, while Cerro Negro has mainly Ca-sulfate. Although some hexahydrite, a Mg-sulfate, was observed on the top portion of fumaroles at Cerro Negro, the dominant Nicaragua sulfate is gypsum. These differences may be due to basalt and gas chemistry differences, which we find to be controlling parameters of alteration. In the Mars cases where a near pure silica soil is observed (East Valley near Home Plate [*Ruff et al.*, 2011]), we note that such an environment can be formed in systems with acidic fumarolic emissions.

In summary, previous studies suggest that hydrothermal systems on Mars with abundant sulfates and hydrated silica may have undergone alteration similar to what we identified at the field sites in Nicaragua [e.g. *McCollom and Hynek*, 2005; *Squyres et al.*, 2007; *Hynek et al.*, 2011]. Iron oxides/hydroxides and phyllosilicates, which can be more difficult to detect using XRD and SEM techniques, are particularly distinctive in VNIR spectroscopy and our data show these mineral classes are present in our field sites. Based on our work, we expect that a certain amount of these less abundant mineral families are present in the areas of high sulfate abundance on Mars. However, the dominance of gypsum and hydrated silica could mask minor mineral contributions when viewed from orbit.

2.7 Conclusions

We utilized a field reflectance spectrometer to detail the surface mineralogy of Cerro Negro, Momotombo, and Telica volcanoes, and the San Jacinto Mudpots in Nicaragua. The unique aspects of this study include:

- Utilization of *in situ* techniques to ensure identification of minerals present in the environment and not those they may have transformed to during transportation.
- The first time these field sites were studied with VNIR reflectance spectroscopy for direct comparison to Mars orbiter data.
- Addition of neighboring volcanic sites to understand regional context and broad environmental controls.

The inaugural use of *in situ* techniques at Cerro Negro, Momotombo, Telica, and the San Jacinto Mudpots demonstrates the strength of such instruments to rapidly characterize areas of study. These systems are pertinent to understand early Mars volcanic, hydrothermal alteration. From this study we provide the following major conclusions:

- The strengths of VNIR reflectance spectroscopy, as compared to the XRD results in the companion paper [*Hynek et al.*, submitted], lie in the rapid collection of measurement (on the order of 15 seconds) and the added identification of minor iron oxides/hydroxides and phyllosilicates.
- While alteration is widespread with a variety of environmental parameters, the common minerals identified at these sites are limited to gypsum (sulfates), hematite and goethite (oxides/hydroxides), kaolinite+smectite (phyllosilicates), and hydrated silica. Elemental sulfur is abundant throughout Momotombo and near active fumaroles at Cerro Negro.

- Despite potential biases from sampling, mineral masking, and detecting only those minerals more distinct in the VNIR wavelength range, the paralleled results between the sites and instruments demonstrated the discussed trends, keeping in mind that the number of samples analyzed at each site was not the same.
- Mineralogy is consistent with that found on Mars, although it varies on a scale equivalent to the fumaroles, i.e. a few to 10s of meters. Such scales and relationships are harder to discern from remote sensing, and *in situ* techniques as well as geological and regional context may be needed.
- Locations on Mars that had or may have had volcanic inputs, such as Noctis Labyrinthus, Syrtis Major, and Gusev crater area, and sites that may have had localized hydrothermal activity, such as Valles Marineris, Mawrth Vallis, and Meridiani Planum, can be directly compared to the mineralogy of the Nicaraguan field sites.

The above aspects and results provided novel insights into the acid-sulfate alteration at the Nicaraguan volcanoes and their application for interpreting ancient hydrothermal systems on Mars.

3. Laboratory simulations of acid-sulfate weathering under volcanic hydrothermal conditions: Implications for early Mars

Note: This chapter was submitted to the Journal of Geophysical Research-Planets as: Marcucci, E.C., and B.M. Hynek. "Laboratory simulations of acid-sulfate weathering under volcanic hydrothermal conditions: Implications." It is cited in the reference list and other chapters as "Marcucci and Hynek, submitted." Sections have been re-numbered and figures are in text to match the formatting of the dissertation. References for this paper have been combined with others at the end of dissertation. Acknowledgements have been combined at the beginning of the dissertation. Supplemental tables submitted with this paper have been moved to the Appendix A of the dissertation.

Abstract: We have completed laboratory experiments and thermochemical equilibrium models to investigate secondary mineral formation in conditions akin to a volcanic, hydrothermal acid-sulfate weathering system. Basaltic mineralogy at Cerro Negro Volcano, Nicaragua, characterized by plagioclase, pyroxene, olivine, and volcanic glass, was used. These individual minerals and whole rock field samples were reacted in the laboratory with 1 molal sulfuric acid at varying temperatures (65, 150, 200°C), fluid:rock weight ratios (1:1, 4:1, 10:1), and durations (1-60 days). Thermochemical equilibrium models were designed in Geochemist's Workbench. To understand the reaction products and fluids, we undertook scanning electron microscopy/energy dispersive spectroscopy, x-ray diffraction, and inductively coupled plasma-atomic emission spectroscopy. The results of our experiments and models yielded major alteration minerals that include anhydrite, natroalunite, minor iron oxide, and amorphous Al-Si gel. We found that variations in experimental parameters did not drastically change the suite of minerals produced; instead, abundance, size, and crystallographic shape changed. Our results also suggest that it is essential to separate alteration and evaporation phases to fully understand the reaction processes. Our laboratory reacted and model products are consistent with the mineralogy observed at places on Mars. However, our results indicate that determination of the unique formation conditions requires microscopic and regional context, as well as a thorough understanding of contributions from direct alteration and evaporation minerals.

3.1 Introduction

The first indications that sulfate salts existed on Mars came from the Viking missions. High concentrations of sulfur in soil samples suggested sulfate-cemented fines formed pebbles and duricrusts [e.g. *Toulmin et al.*, 1977]. Soils studied by the Pathfinder rover had some sulfate, but they were depleted with respect to Viking levels [*Bell et al.*, 2000], which has been interpreted as instrument resolution, masking differences, or a different kind of soil. More recently, Phoenix used water chemistry experiments to detect soluble ionic species consistent with Mg- or Ca-sulfate [*Kounaves et al.*, 2010]. Extensive observations of the Martian surface

by the Mars Exploration Rovers (MERs) and the Observatoire pour la Minéralogie, l'Eau, les Glaces et l'Activité (OMEGA) and Compact Reconnaissance Imaging Spectrometer (CRISM) instruments on board orbiters identified numerous sulfate mineral deposits widespread on the planet [e.g. *Gendrin et al.*, 2005; *Squyres et al.*, 2006b, 2007; *Murchie et al.*, 2009b].

Concordant and ongoing remote sensing results from the OMEGA and CRISM instruments have revealed sulfate deposits in discrete locales that are globally distributed. Data from visible and near-infrared spectroscopy have matched bands of specific spectra to kieserite ($MgSO_4 \cdot H_2O$) and gypsum ($CaSO_4 \cdot 2H_2O$) as well as other polyhydrated sulfates [e.g. *Gendrin et al.*, 2005; *Bishop et al.*, 2009; *Ehlmann et al.*, 2009a; *Murchie et al.*, 2009b; *Wray et al.*, 2009a, 2009b]. Often the spectra for the latter cannot be uniquely assigned to specific minerals, thus the general polyhydrated identification, but that may include epsomite ($MgSO_4 \cdot 5H_2O$), hexahydrite ($MgSO_4 \cdot 6H_2O$), starkeyite ($MgSO_4 \cdot 4H_2O$), melanterite ($FeSO_4 \cdot 7H_2O$), ferricopiapite ($Fe_{2/3}^{3+}Fe_4^{3+}(SO_4)_6(OH)_2 \cdot 20H_2O$), copiapite ($Fe^{2+}Fe_4^{3+}(SO_4)_6(OH)_2 \cdot 20H_2O$), or halotrichite ($FeAl_2(SO_4)_4 \cdot 22H_2O$) [*Gendrin et al.*, 2005; *Bishop et al.*, 2009]. The interior layered deposits of Valles Marineris and associated chaos regions contain the most aerially-extensive sulfate deposits identified to date by OMEGA and CRISM [e.g. *Chojnacki and Hynek*, 2008; *Murchie et al.*, 2009b]. Areas with hydrated silica and a hydroxylated ferric sulfate hydronium jarosite deposits, suggesting an acidic origin, which may be associated with hydrothermalism [*Milliken et al.*, 2008; *Bishop et al.*, 2009].

The Columbia Hills regions of Gusev crater contained a silica-rich material and Fe-phases, magnetite (Fe_3O_4) and nanophase oxides [*Squyres et al.*, 2007]. Initial textural and morphological clues, like fine layering and a bomb sag, and chemical clues, such as high volatile content, at Gusev crater supported a pyroclastic origin for the deposits known as Home Plate

[*Arvidson et al.*, 2006; *Squyres et al.*, 2007; *Schmidt et al.*, 2009; *Ruff et al.*, 2011]. The Home Plate deposits and Paso Robles soils in the Gusev crater consist of silica-rich deposits and ferric sulfates that are thought to represent hydrothermally altered volcanic material from acidic gas emissions and/or hot springs [e.g. *Lane et al.*, 2008; *Squyres et al.*, 2008; *Yen et al.*, 2008; *Schmidt et al.*, 2009; *Ruff et al.*, 2011].

Sulfates can form in a wide variety of environments. Mechanisms for the formation of the Martian deposits has been suggested to include: evaporation of briny water [*Squyres et al.*, 2004, 2006b; *McLennan et al.*, 2005], distribution of meteorite impact ejecta [*Knauth et al.*, 2005], formation in dirty ice [*Niles and Michalski*, 2009], condensation of volcanic acid fog [*Banin et al.*, 1997; *Tosca et al.*, 2004], and exposure to hydrothermal systems [*McCollom and Hynek*, 2005; *Squyres et al.*, 2007; *Chojnacki and Hynek*, 2008; *Ruff et al.*, 2011]. Although each of these formation mechanisms can plausibly produce sulfate deposits, they should have distinct geomorphic and regional expressions. Because of the global distribution and diverse geologic settings in which the sulfates occur, it is likely that various formation mechanisms occurred on the surface throughout time to deposit the sulfates and suggest different interpretations of the local geological history and evolution. Thus the ability to distinguish among the formation mechanisms is critical for understanding Mars' history. This differentiation requires an understanding of the geochemical reaction pathways, how mineral products may vary within each due to environmental conditions, as well as how the sulfates fit the geologic and geomorphic context. Detailing the paleoconditions has implications for the past habitability potential of the planet, because the role of liquid water in each geochemical mechanism differs. This work focuses on characterizing the expression of acid-sulfate alteration in volcanic environments.

Numerous studies have examined basalt weathering in the field, laboratory experiments, and thermodynamic/kinetic models. They have done each of these for different pHs, temperatures, and solution compositions. Basalt weathering is influenced by solution temperature and pH as well as mineral precipitation. Mars analog work has examined the acid-sulfate weathering of basalt, but the experiments to date have generally focused on lower temperatures or restricted parameter space [*Banin et al.*, 1997; *Tosca et al.*, 2004, 2005; *Golden et al.*, 2005; *Hurowitz et al.*, 2005; *Zolotov and Mironenko*, 2007; *McAdam et al.*, 2008]; they were not necessarily aimed at high temperature, volcanic environments. Additionally, of the previous studies, only *Hurowitz et al.* [2005] took evaporation into consideration as a separate phase. *Tosca et al.* [2004] and *Banin et al.* [1997] evaporated fluid but did so on top of grains. In the previous studies, a variety of sulfates form with some additional amorphous silica and iron oxides. However, all studies attributed the formation of the sulfates formed to evaporation. Experimental work most similar to the experiments here were related acid-sulfate alteration of Cerro Negro basalt cinders [*McCollom et al.*, 2013]. Alteration of these cinders dominantly produced amorphous silica, anhydrite, Fe-bearing natroalunite, with lesser amounts of iron oxides and sulfates, including hexahydrite in low fluid:rock ratios. Modeling done in conjunction with these experiments produced similar alteration minerals [*McCollom et al.*, 2013].

Similarly there is limited acidic thermodynamic modeling work related to Mars. Two studies that have created extensive models look at 0°C or focused on the evaporation process. While the models of *Zolotov and Mironenko* [2007] detailed both alteration and freezing/evaporation minerals, the models had a temperature of 0°C. They modeled the formation of amorphous silica, Fe-hydroxides, and then phyllosilicates as the main alteration products. Limited gypsum was also formed under very low pH conditions. Additional sulfates,

Mg-, Fe-, and Ca-sulfates formed during the freezing model progression. Similar sulfates formed in evaporation models created for the Meridiani Planum system [*Tosca et al.*, 2005]. The 0°C models find that plagioclase weathers more slowly than pyroxene and olivine [*Zolotov and Mironenko*, 2007; *McAdam et al.*, 2008]. *Berger et al.* [2009] also used 0°C in their models; however, the very low pH, pure sulfuric acid, and low fluid:rock ratio are more akin to the experiments and models presented in this paper. In these conditions the alteration mineralogy was amorphous silica and jarosite, corresponding to Merdiani Planum bedrock. As the system evolved Mg-, Ca-, and Fe-sulfates formed and phyllosilicates were stable at even more evolved progress [*Berger et al.*, 2009].

To further elucidate acid-sulfate alteration in a volcanic system, we based our study on the Cerro Negro Volcano in Nicaragua that has been studied as an analog for this process on ancient Mars [*Rogers et al.*, 2011; *Hynek et al.*, 2012; submitted; *Marcucci et al.,* submitted; *McCollom et al.,* submitted]. Cerro Negro (CN) is a young, active volcanic complex in western Nicaragua and it is composed of plagioclase, olivine, and pyroxene phenocrysts, glass, and titanian magnetite ($Fe^{2+}(Fe^{3+},Ti)_2O^4$) [e.g. *Walker and Carr*, 1986]. It first erupted in 1850, with the most recent eruptions having occurred in 1992, 1995, and 1999. This volcano was chosen as a Mars analog environment because of its lithology closely matches that of Martian bedrock and meteorites, although iron content is lower at CN (Figure 16). This is significant because parent rock lithology controls fluid composition, which in turn controls secondary mineralogy [*Tosca et al.*, 2004]. It is also young with a well-recorded history and ongoing S- rich fumarolic activity allows realtime observations of alteration. Differences can be examined between alteration sites that have been exposed for varying lengths of time based on eruption date (few years to decades). While other Mars analog sites have been used to examine acid-sulfate weathering, CN

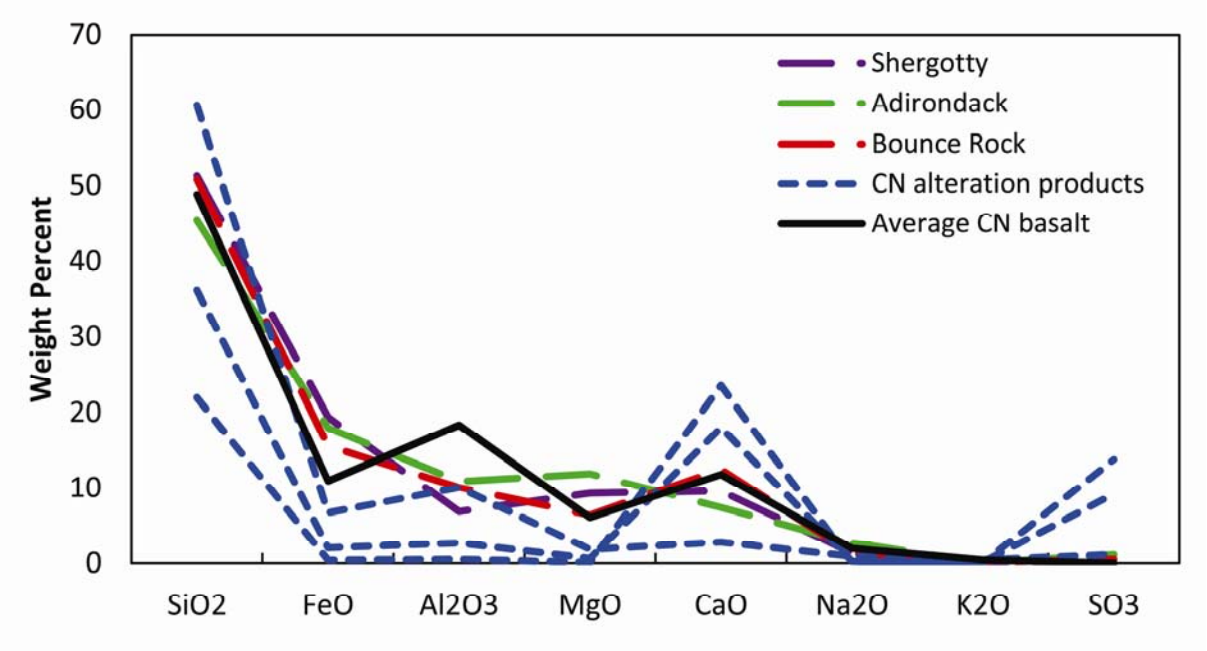

Figure 16. Comparison plot of the oxide composition of unaltered Cerro Negro basalt, CN field alteration products [*McCollom and Hynek*, 2005], and sample Martian basalts [*Rieder et al.*, 2004], Adirondack [*Gellert et al.*, 2004], and Shergotty [*Lodders*, 1998].

more accurately represents the composition of measured Martian rocks and possible conditions for an early hydrothermal volcanic environment on Mars; it also has extensive ongoing alteration. Here, we report results from experiments and models to characterize the chemical and mineralogical pathways to assess basaltic acid-sulfate alteration at CN and in the broader context, a type of alteration that could form the sulfates observed on Mars early in its history.

Experiments were designed to test a range of parameters, including mineral type, weathering duration, fluid:rock weight ratio, and temperature. The goal was to characterize the acid-sulfate weathering reactions occurring at Cerro Negro, and ultimately on early Mars. Our works differs from previous work in three ways: 1) the hottest experiments were conducted at a temperature higher than most previous Mars laboratory work; 2) we separate evaporation and alteration products; and 3) and we use a combination of models and experiments to more fully understand the reaction pathways. Our goal was to use a systematic approach by varying initial

parameters to determine if they produce diagnostic mineral suites or features that can be used to characterize acid-sulfate weathering in a relic hydrothermal system on Mars, such as the Paso Robles soils or Home Plate [*Squyres et al.*, 2007; *Lane et al.*, 2008; *Yen et al.*, 2008; *Ruff et al.*, 2011]. Key questions we address include: What secondary minerals do specific primary minerals produce? Do variations in duration, fluid:rock ratio, or temperature create distinguishing characteristic in the secondary mineralogy? Do these experiments yield insights into the reaction kinetics?

3.2 Methods

3.2.1 Experiments

We reacted pure minerals representative of CN basalt composition as well as whole rock field samples. The CN pyroxene has a calcium and magnesium rich composition [*Walker and Carr*, 1986; *Roggensack et al.*, 1997], so augite was chosen as the representative mineral [*Hoch et al.*, 1996] (Table 3). Calcium-rich plagioclase exists at CN; and bytownite was used in experiments [*Morrison et al.*, 1983]. San Carlos olivine was used to simulate the CN olivine. San Carlos olivine is less Fe-rich than CN olivine; however, it was a readily available composition most similar to CN. All minerals were acquired from Ward's Natural Science and prepared by grinding, sieving, and rinsing for a consistent grain size of 106-212 microns for uniformity between starting materials. Unaltered CN cinders collected during a field campaign from the 1999 cone were also reacted.

The dominant alteration environment at CN is a gas-dominated fumarolic system. In such environments, acidic steam condenses on rock surfaces and alteration takes place at rock/atmosphere boundaries thus representing a closed system. Open system components such

Table 3. Primary Material Composition in weight percent. Unless otherwise noted, composition was determined by XRF.

	Plagioclase (bytownite)[1]	**Pyroxene (augite)[2]**	**Olivine (forsterite)[3]**	**CN 1999 cinders**	**CN Plagioclase[4,5]**	**CN Pyroxene[4,5]**	**CN Olivine[4,5]**
SiO_2	49.3	54.1	40.5	48.35	44.2-46.8	53.8	56.5-55.0
Al_2O_3	32.5	0.7	--	17.65	36.0-34.2	--	--
Fe_2O_3 (T)	--	--	--	11.09	--	--	--
FeO (T)	--	6.1	11.6	--	9.6	9.6	12.8-18.4
MnO	--	--	--	0.193	--	--	--
MgO	--	15.8	47.8	6.65	--	15.5	30.7-26.6
CaO	15.3	21.2	--	11.9	19.4-17.3	21.1	--
Na_2O	2.8	0.6	--	1.97	0.4-1.7	--	--
K_2O	--	--	--	0.42	--	--	--
TiO_2	--	1.5	--	0.7	--	--	--
P_2O_5	--	--	--	0.09	--	--	--
Cr_2O_3	--	--	--	0.02	--	--	--

[1][*Morrison et al.*, 1983]
[2][*Hoch et al.*, 1996]
[3][*McCollom and Seewald*, 2001]
[4][*Walker and Carr*, 1986]
[5][*Roggensack et al.*, 1997]

as precipitation on rock surface do occur in the environment. However, the dominant control on secondary mineralogy is the closed system aspects. For the purposes of this paper, we consider CN as a closed system and used sealed reaction vessels to represent the alteration of the rocks from condensed steam that accumulates on their surfaces. There was Earth atmosphere in the container headspace. This is also a more straightforward experimental set up that could be run in bulk in the laboratory. Additionally, we chose H_2SO_4 to isolate the sulfur reactions to explore the formation of sulfates. Chemistries, for example chlorides, indicate the presence of other acids (HCl) on Mars, however we were most interested in the dominance of sulfur in solutions

expected for Mars and thus considered chlorides and other acids to be beyond the scope of this experiment.

The majority of experiments presented in this paper had an experimental temperature of 65°C. Figure 17 displays a summary of experimental design. In Savillex PFA acid digestion vessels, approximately 3 grams of mineral grains or CN basalt were mixed by weight with 1 molal (m) H_2SO_4 in fluid:rock ratios of 1:1, 4:1, and 10:1 (Figure 17; Table 4). Savillex vessels were sealed using a hand wrench. High oxidation of iron in olivine experiments indicated headspace Earth atmosphere and potential penetration of atmospheric O_2 into these containers. These experiments were reacted in the presence of Earth atmosphere to represent conditions at terrestrial analog sites. The containers were sufficiently sealed against loss from vapor escape below 70°C (limiting experimental temperature) with less than 0.1% mass loss in containers.

Table 4. Parameter Variations for Experiments and Models

Fluid	1 M H_2SO_4
Minerals	Plagioclase, pyroxene, olivine
Fluid:rock ratio	1:1, 4:1, 10:1 (weight)
Temperature	65°C, 150°C, 200°C
Duration	For 4:1 experiments: 3, 6, 9, 12, 30, 35, 40 days; 7.5 months For 1:1 and 10:1 experiments: 3, 12, 30 60 days
Added steps (long 10:1 and 1:1 experiments, high T, CN cinders)	Filtering fluid sample; rinsing-filtering products with ethanol
Analysis	pH[1], XRD, SEM/EDS, ICP-AES, petrography

[1] pH was measured at experiment termination at room temperature and GWB was used to determine the actual pH using a one-step or two-step speciation calculation. Fluid was first speciated in REACT at 25°C, while balancing on sulfate. The system was then respeciated with the adjusted sulfate value at 65°C, allowing charge balance on pH, giving *in situ* pH and speciation. Due to available supplies, pH was initially measured using pH paper, which had a lower limit of 0.8, although actual pH was lower in some cases. In cases where pH was measured at this limit, initially balancing on sulfate caused too great a compensation of sulfate in the charge balance, skewing speciation results. In cases with pH measured as 0.8, fluid was balanced on pH at 65°C in one step. This affected augite experiments in the 4:1 and 10:1 fluid:rock ratio experiments. This issue was rectified with the purchase of a micropH meter, used in 60-day, 1:1 and 10:1 experiments, all CN cinder experiments, and subsequent higher temperature experiments.

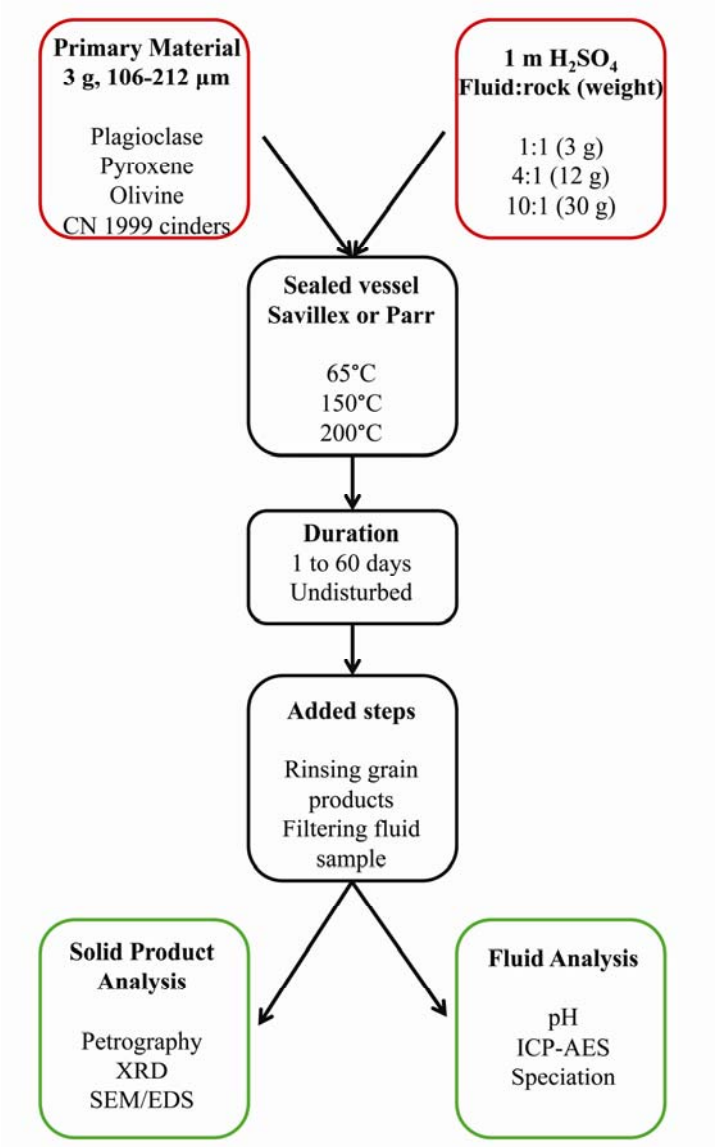

Figure 17. Flow chart of experimental design and analysis techniques. Table 4 and the text further detail parameters.

We chose 3 grams as the total amount of initial material because it was sufficient sample for analysis on multiple instruments. We chose the 4:1 fluid:rock weight ratio for comparison to previous experiments that used a similar ratio [*McCollom et al.*, 2013]. We used a 1:1 ratio to represent a much lower fluid:rock ratio, simulating thin surface coatings of acid on rocks and still

having enough fluid for analysis. For a high fluid:rock ratio, 10:1 was chosen based on the volume capacity of the reaction vessels. These above experiments were conducted for 3- to 60-days and a single fluid:rock ratio set for 7.5 months (Table 4). Durations were chosen to examine regular intervals within the 60 day set for a reasonable total completion time given the number of experiments to be completed.

Each timestep was a discrete set-up so that containers remained closed and undisturbed throughout the experiment (Figure 17). At the termination of each step, a fluid sample was taken and diluted; nitric acid was used to acidify samples above pH of 3 to retain dissolved species. For the first set of experiments, remaining fluid was siphoned off and discarded. Grains were subsequently air-dried at ambient temperatures. Sampling procedures were refined approximately halfway through the experimental study when we recognized the importance of evaporation in grain drying. New procedures included filtering the fluid sample, retaining the excess fluid for evaporation, and rinsing the grain products with ethanol while filtering with a handheld vacuum pump (hereafter referred to as rinse-filtering). This added step separated evaporative Mg-sulfates from alteration mineralogy. For clarity, the data presented in this paper represent the rinsed experiments.

To examine the secondary mineralogy in higher temperatures, an abbreviated series of experiments ran at 150 and 200°C with similar mineral preparation as the lower temperature experiments (Figure 17). These reactions occurred in a Parr acid digestion bomb, which consists of a PTFE liner inside a sealed metal pressure vessel. The highest experimental temperature, 200°C, was limited by the specifications of the Parr reaction vessel. A middle temperature of 150°C was chosen as a point between the high and low temperatures. Mass loss for these containers over the duration of the experiments was <0.05%. The series of parameter variations

were shortened due to secondary product similarities discussed below. Three minerals—pyroxene, plagioclase, and olivine—were reacted at a 4:1 fluid:rock ratio with 1m H_2SO_4 for 1 day at 150 and 200°C; pyroxene and olivine only were also reacted for 15 days at 200°C. Products were handled with the more detailed procedures, including rinse-filtering solid products and evaporating fluid remnants.

3.2.2 Experimental Analysis

Solid products were analyzed for elemental, mineralogical, and structural variations. Grain mounts were prepared to assess mineralogy and magnitude of alteration for 15 samples of primary and altered materials and observed with plain and crossed-polarizing light in a petrographic microscope. A Scintag x-ray diffraction (XRD) machine was used to examine the solid reactants and products for detailed mineralogy. A JEOL scanning electron microscope (SEM) showed the microscopic crystal formations and the accompanying energy dispersive spectrometer (EDS) measured the elemental composition of features. Fluid aliquots were analyzed for major, minor, and trace components using inductively coupled plasma–atomic emission spectroscopy (ICP-AES).

3.2.3 Thermodynamic Equilibrium Models

To further understand the alteration pathways within the experiments, we built thermodynamic models to replicate the experiments. We completed our analysis using Geochemist's Workbench (GWB) [*Bethke*, 2008], a software program that models chemical reactions by calculating thermodynamic equilibria. Although the program also has the ability to incorporate kinetics into the reaction progress, that option was not used in our models because of time limitations and lack of experimental constraints at high temperatures. Our thermodynamic database was modified to include a broader range of sulfate mineral data than the standard

libraries, such as complex sulfate natroalunites ($NaAl_3(SO_4)_2(OH)_6$), to better represent our potential experimental products. The thermodynamic information for added minerals was calculated using supcrt92 [*Johnson et al.*, 1992] and summarized in *McCollom et al.* [2013]. We outline a specific model example in the results section. In brief, a reaction was set up by creating a sulfuric acid solution at a set temperature and incrementally adding solid material to the solution. We held the temperature constant throughout the reaction. Because kinetics were not incorporated into our models, we suppressed more thermodynamically stable, but kinetically inhibited crystalline forms for silica, such as quartz, tridymite, coesite, and cristobalite, using controls in GWB to disallow their growth. However, the models were used to elucidate reaction pathways of the experiments, and ultimately compare to the field and Mars. Therefore, we only suppressed these phases that were known to be absent from the Cerro Negro field site. A related paper [*McCollom et al.*, 2013] presents results in which phyllosilicate phases were also suppressed since they were not present in experimental results.

Fluid analysis, including pH measurements, was completed at 25°C and not experimental temperature. Because fluid chemistry and speciation is temperature dependent, the results of fluid analysis were not representative of *in situ* chemistry, which ultimately dictates precipitation. A second use for GWB was to determine the *in situ* experimental pH and fluid speciation. Elemental fluid composition measured by ICP-AES was first speciated in REACT in a one- or two-step process depending on pH (see footnote of Table 4). The pH inputs in the experiments were measured with pH paper and an Accumet® micro-pH meter.

3.3 Results

Alteration occurred very rapidly in plagioclase, pyroxene, and olivine experiments with extensive macro- and microscopic alteration observed even in the shortest timestep (Table 5).

Table 5. Secondary Mineralogy and Relative Abundances[1]

	Plagioclase	**Pyroxene**	**Olivine**	**CN basalt**
	Experimental	**Alteration**	**Minerals**	
		XRD	**Results**	
Primary material	M	M	M	M
Anhydrite	m	M	-	-
Gypsum	M	-	-	M
Hexahydrite	-	-	M	-
Starkeyite	-	-	m	-
Pentahydrite	-	-	-	m
Alunogen	m	-	-	m
Ferrohexahydrite	-	-	M	-
Amorphous silica	-	-	-	-
		SEM	**Results**	
Primary material	M	M	m	M
Ca-sulfate	M	M	-	M
Mg-sulfate	-	-	M	M
Al-sulfate	M	-	-	m
Natroalunite	M	-	-	M
Fe-sulfate	-	m	m	M
Fe-O	-	-	m	-
Amorphous silica	M	-	M	M
	Experimental	**Evaporation**	**Minerals**	
		XRD	**Evaporation**	
Anhydrite	-	M	-	-
Kieserite	-	-	m	-
Hexahydrite	-	-	-	m
Pentahydrite	-	-	M	-
Alunogen	M	-	-	M
Voltaite	-	m	-	-
Rhomboclase	-	m	-	-
		SEM	**Evaporation**	
Ca-sulfate	M	M	-	m
Mg-sulfate	-	M	M	M
Al-sulfate	M	m	-	M
Fe-sulfate	-	M	m	-
Mg-Na sulfate	-	M	-	M
Mg-Fe sulfate	-	m	-	-
Si-phase	-	-	-	m

[1]'M' indicates a major phase, 'm' indicates a minor, and '-' indicates none present. Determination of abundance was done through relative amounts in SEM images and intensity of peaks in XRD.

Table 5 outlines the experimental minerals determined for each starting material according to type and instrument. It is divided into two main parts and two subdivisions. The top half presents the mineral results from alteration, while the bottom has evaporation mineral. These sections are each subdivided so that minerals detected by XRD are shown first and trace minerals identified with SEM shown second. The concentration of sulfate (or Mg^{2+} for olivine) in the fluids at the termination of the experiments compared to the predicted sulfate consumption (Mg^{2+} accumulation) in models indicated that reactions have not reached equilibrium at any temperature (Table A1). Additionally, the suite of secondary minerals were different for each primary mineral, but were consistent within that mineral regardless of duration, fluid:rock ratio, and temperature. Variations in these three parameters affected crystal abundance, size, and morphology, which we detail in the following sections and Table A2.

3.3.1 Experimental Products

3.3.1.1 Plagioclase (bytownite)

The macroscopic alteration evident at the termination of each plagioclase experiment was a clear gel situated on top of the largely unaltered grains (Figure 18A). It was hard to remove all traces of this gel in rinsed experiments; as a result trace amounts of gel remained with the grain products. The gel also likely included entrained fluid. This gel material dominated grain mount petrography and there were no changes in grains observed with time. However, differences in secondary products were observed on the microscopic scale through XRD and SEM. The main solid phase products for all timescales were natroalunite, amorphous silica, and alunogen. Gypsum was also present, likely as an evaporitic product.

XRD spectra of rinsed grain products consisted mainly of primary material with some

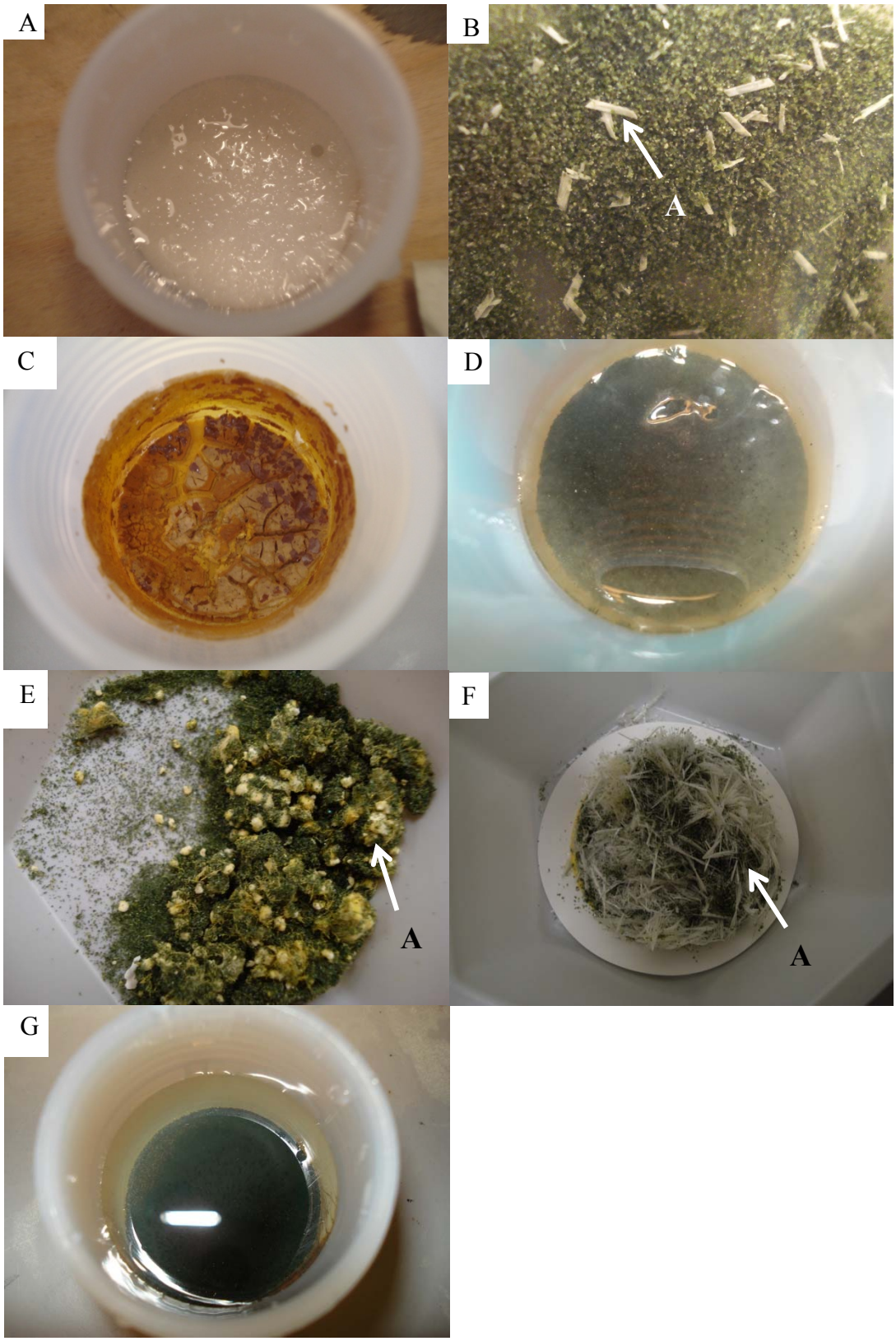
A
B
A
C
D
E
A
F
A
G

Figure 18. Images of macroscopic alteration of 65°C experiments. (A) Shiny layer on top of the white plagioclase grains is a layer of clear gel. (B) Green pyroxene grains with white Ca-sulfate (anhydrite-'A') approximately 5 mm. (C) Dried opaque orange gel; darker spots are the platy film from the top of the fluid of olivine experiments. Translucent reaction vessels are 50 mm in diameter. (D) Translucent gel layer on top of CN 99 basalt cinders. (E) Image of spheres in the pyroxene 1:1 60-day experiment, which showed to be composed of short rods of anhydrite. (F) Abundant anhydrite crystals from a 7.5-month experiment. (G) Thicker gel layer from a 10:1 CN basalt experiments.

gypsum and alunogen peaks (Table 5; Figure 19A). Based on the elevated temperature of experiments and geochemical models (Section 4.4), the presence of gypsum was unexpected. We attribute the formation of gypsum, instead of the dehydrated Ca-sulfate anhydrite, to the evaporation of fluid entrained in the gel material. SEM confirmed the presence of a Ca-sulfate phase in the alteration products and showed two additional alteration phases not indicated in XRD (Table 5; Figure 20). The additional phases were distinct cubic crystals and fans or blocky surface coatings. The EDS data of the cubic crystals determined these were natroalunite and had an average composition of $Na_{0.67}(H_3O)_{0.33}Al_{2.15}(SO_4)_2(OH)_{3.44}(H_2O)_{2.56}$. Composition was calculated with EDS data using the techniques of *Drouet and Navrotsky* [2003], which assumes two SO_4 per unit formula and hydronium (H_3O) to complete the 1+ ion balance. SEM images showed that increasing fluid:rock ratio decreased the relative abundance of natroalunite and no natroalunite was apparent in the 10:1 ratio experiments (Figure 20B and 5C). The amorphous surface fans and blocks had an EDS signature of Al-S-Si, with blockier features having a higher Si content than fans (Figure 20A), hereafter called amorphous silica. The fans were seen in a prior set of whole basalt experiments, which also formed gels [*McCollom et al.*, 2010, 2013]. Compared to mineralogical features in unrinsed experiments, there were noticeably less the Al-S-Si gel features than in the rinsed experiments.

Evaporation of experimental fluid produced sufficient material for XRD analysis in only one case, and alunogen was the main product identified (Table 5). All evaporation precipitates could be examined with SEM/EDS, which showed Ca- and Al-sulfate. The Al-sulfate crystal likely accounts for the alunogen XRD peaks.

3.3.1.2 Pyroxene (augite)

The pyroxene experiments showed the most distinctive and diverse suite of alteration and evaporation minerals. Visible after reactions were clear, acicular crystals, which were

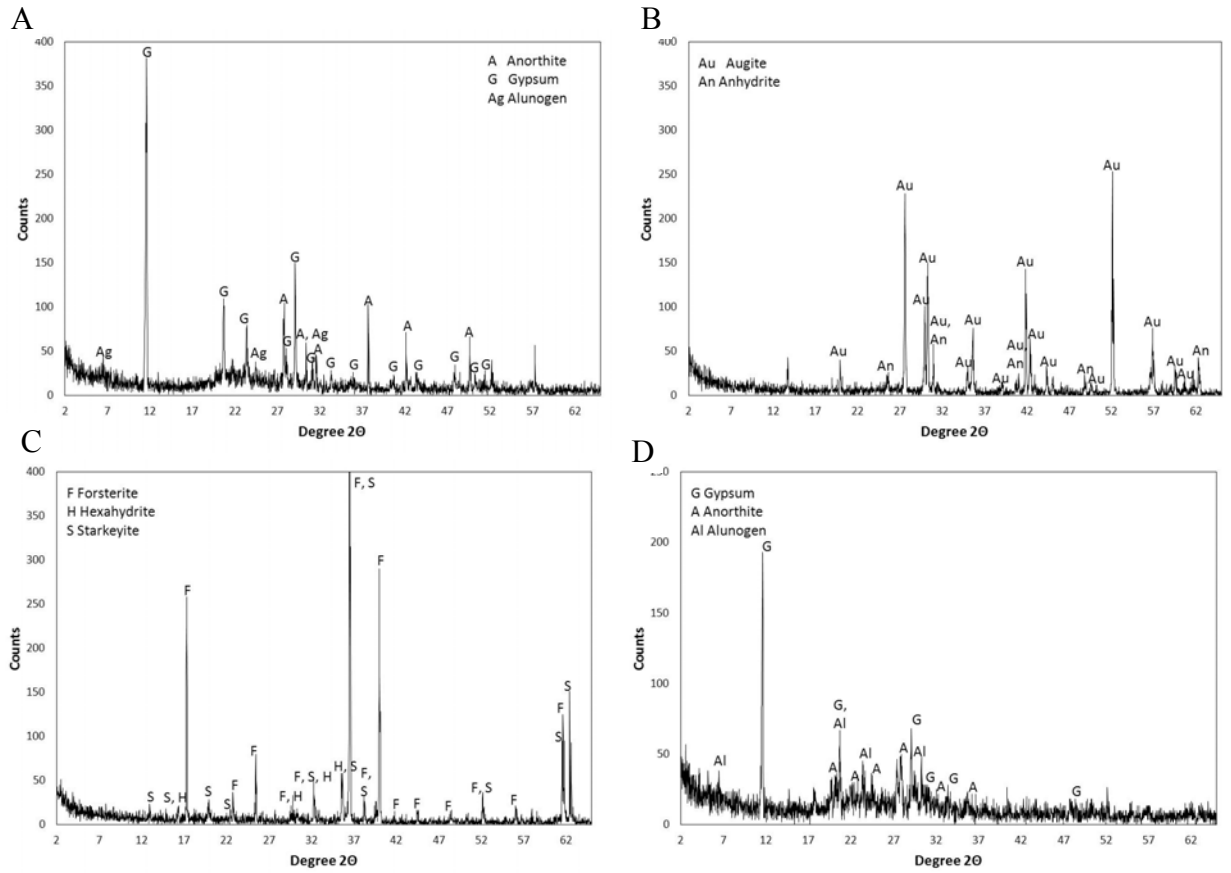

Figure 19. Series of XRD diffractograms from solid products of 65°C experiments. (A) Plagioclase (bytownite) at fluid:rock ratio 10:1 for three days with secondary alteration products identified as gypsum and alunogen. (B) Pyroxene (augite) experiment, 4:1 for thirty-five days. Anhydrite is the main alteration product. (C) Mg-sulfates, hexahydrite and starkeyite, for the 12-day, 1:1 olivine (forsterite) reaction. (D) Gypsum and alunogen peaks, mixed with anorthite peaks from the 4:1, 60-day Cerro Negro basalt experiment.

approximately one centimeter in length and dried white Figure 18B). Despite these distinct macroscopic crystals, petrographic images of grain mounts showed very little change from the original pyroxene. XRD spectra were predominately augite, which was the primary material, with additional peaks identified as anhydrite, which correspond to the macroscopic crystals as well as microscopic ones (Table 5; Figure 19B; Figure 21A). SEM/EDS measurements confirm that Ca-sulfate was abundant as an alteration product. Grain characteristics observed in SEM images show that both alteration and evaporation phases change in size and abundance with variations in experiment duration and fluid:rock ratio. As may be expected, abundance increased

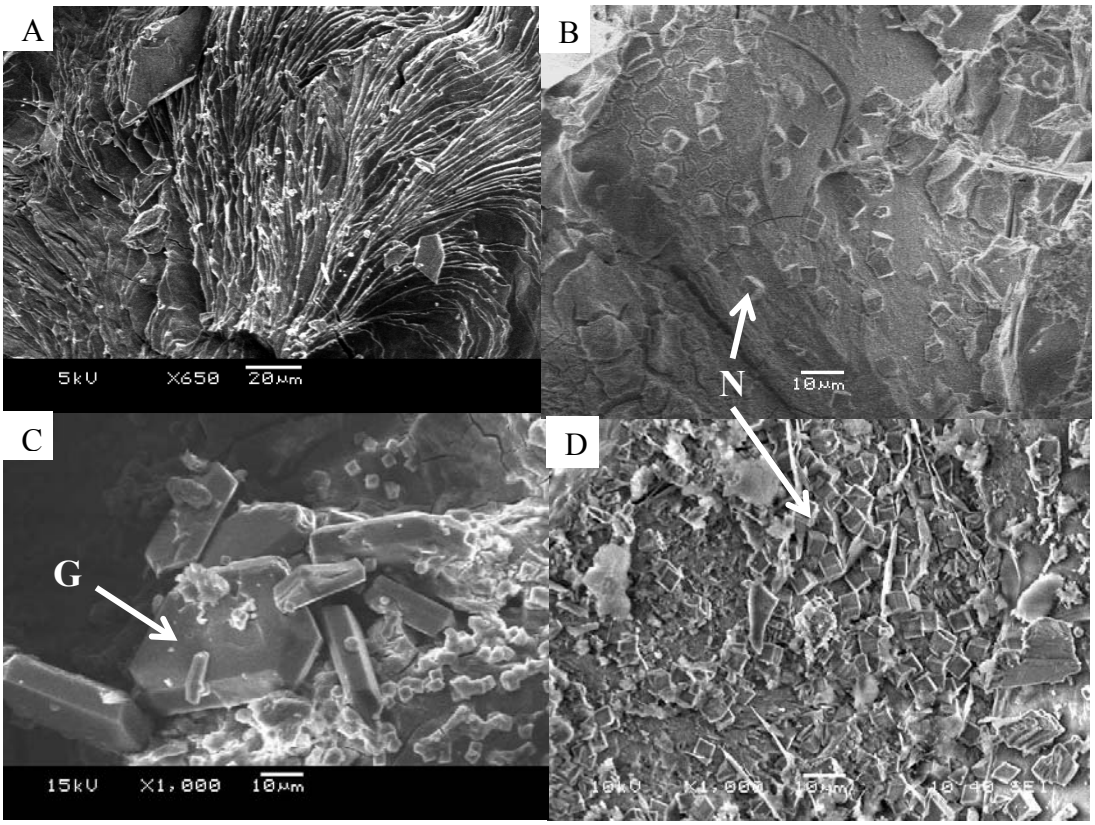

Figure 20. SEM images of plagioclase (bytownite) reacted with 1m H_2SO_4. (A) Fans of dried gel material with an Al-S signature with minor Si. (B) Experiment from 65°C and 4:1 ratio with fewer natroalunite ('N') crystals in the field then lower fluid:rock ratio (C) and higher temperature (D). (C) Gypsum ('G') and natroalunite. This image is from a 1:1 fluid:rock ratio experiment, which has a greater abundance of natroalunite crystals. (D) Natroalunite crystals from the 1-day 150°C experiment.

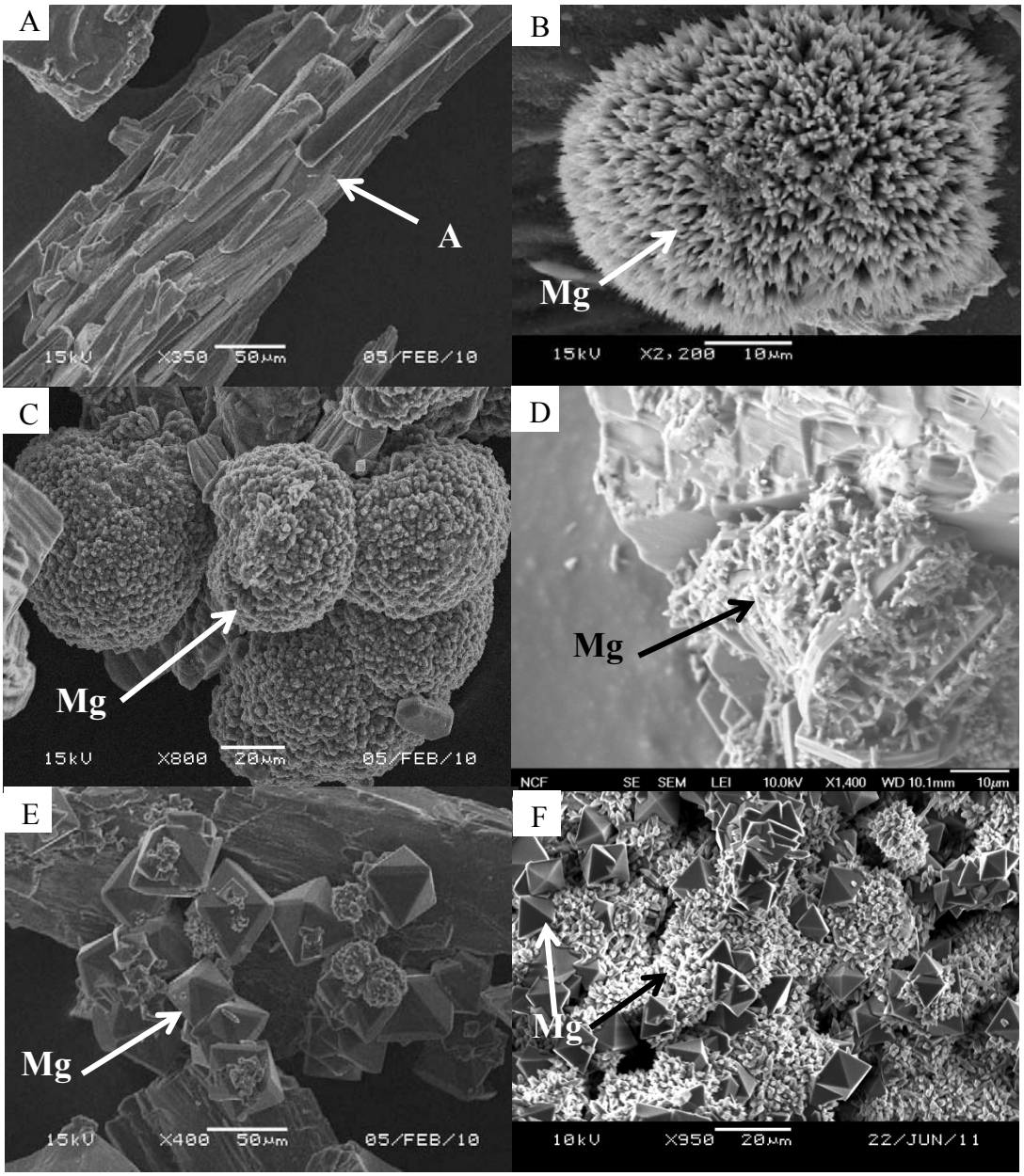

Figure 21. SEM images of pyroxene (augite) reacted with 1m H_2SO_4 at 65°C. (A) Ca-sulfate, identified in XRD as anhydrite ('A'). (B) Mg-sulfate ('Mg') from an experiment with fluid:rock ratio of 10:1. The surface of this sphere has blades, compared to (C) which is another Mg-sulfate sphere with a smoother surface from a 4:1 ratio experiment. (D) Third example of Mg-sulfate for a 1:1 ratio experiments, in the form of a mat of short rods. There is also an increase in size with increasing fluid:rock ratio. (E) Dipyramid crystal with Mg-sulfate signature, present in all experiments. This crystal shape is most similar to that of kieserite and hexahydrite. (F) Mg-sulfates are evaporation products. Later experiments retained and evaporated remaining experimental fluid, which produced numerous and abundant Mg-sulfate precipitates.

with duration and lower fluid:rock ratio with anhydrite alteration crystals being generally thinner, shorter, and more abundant at the 1:1 ratios. While crystals in experiments with ratios of 10:1 were still fine, they were less abundant. A unique feature of the macroscopic anhydrite crystals occurred in the 60-day, 1:1 ratio experiment where in addition to short rods, white spheres were visible to the unaided eye (Figure 18E). SEM images showed these spheres were a conglomeration of microscopic rods (Figure 21A).

The post-experiment rinsing step was most critical for the pyroxene experiments, which had abundant and varying forms of evaporitic Mg-sulfate, evident in SEM images (Table 5; Figure 21B-F). The rinsed secondary products contained no Mg-sulfates, while the subsequently evaporated fluid was dominantly these phases. The universal Mg-sulfate form was a dipyramid crystal (Figure 21E). Kieserite ($MgSO_4 \cdot H_2O$) and hexahydrite ($MgSO_4 \cdot 6H_2O$) have this crystal shape and we hypothesize that one or both of these was the observed mineral. The evaporitic Mg-sulfates appeared in multiple crystal forms in SEM images of each fluid:rock ratio. The dipyramids crystals occurred in all experiments, but other crystal shapes varied. Figure 21B shows that 1:1 experiments had rough, pointy spherical crystals, 4:1 had smoother spheres (Figure 21C), and 10:1 had mats of short rods (Figure 21D). There was also a decrease in size with higher fluid:rock ratio.

Fe-sulfate was also observed in SEM/EDS measurements of the evaporation products (Table 5). Even though Mg-sulfate was abundantly obvious in EDS, the evaporation products measured with XRD indicated anhydrite, voltaite ($K_2Fe^{2+}{}_5Fe^{3+}{}_3Al(SO_4)_{12} \cdot 18H_2O$), and rhomboclase ($(H_5O_2)^+Fe(SO_4)_2 \cdot 2H_2O$), which may correspond to the observed Fe-sulfate. There was no readily apparent Si alteration phase even though this element should be dissolving out of the primary material.

3.3.1.3 Olivine (forsterite)

Olivine alteration had the greatest visible (Figure 18C) and microscopic surface alteration (Figure 22A). The mineral started as pale green grains and changed rapidly to an orange color. An opaque orange gel overlaid the grains. In addition, there typically were suspended orange particles and floating orange films in the fluid. Altered olivine grains had visible dissolution pits in petrographic images. Only one experiment, the 3-day 10:1 set-up, was visually distinctive from the other olivine experiments. It ended with chalky white grains, rather than the otherwise seen orange grains and gels. However, the XRD and SEM mineralogy was consistent with the other experiments. Trace amounts of oxidized iron was the dominant control on alteration color, but alteration mineralogy was mainly amorphous silica with some Mg- and Fe-sulfate from evaporation of entrained fluid.

In addition to primary mineralogy, XRD identified hydrated Mg-sulfates, probably starkeyite and hexahydrite ($MgSO_4 \cdot 4H_2O$ and $MgSO_4 \cdot 6H_2O$) (Table 5; Figure 19C), which were likely an evaporation product. In SEM, virtually every surface was covered by amorphous

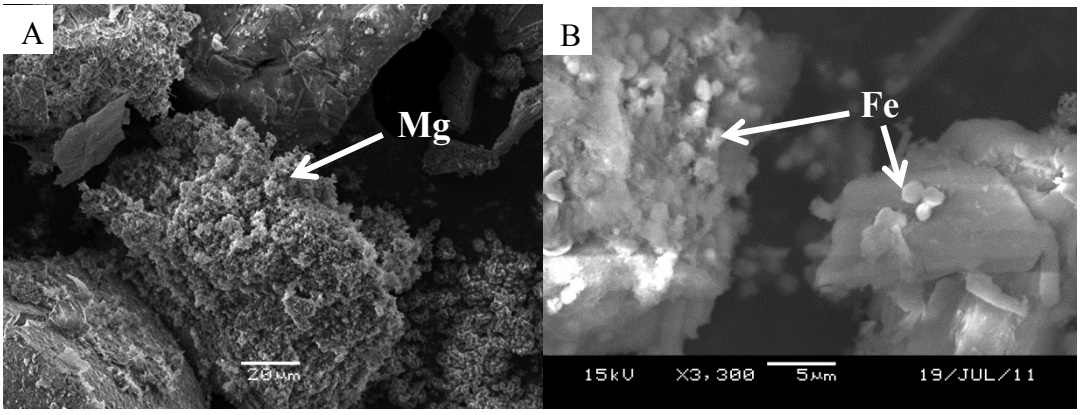

Figure 22. SEM images of olivine (forsterite) reacted with 1m H_2SO_4 at 65°C. (A) Amorphous surface alteration with a Mg-sulfate signature ('Mg') with a 4:1 fluid:rock weight ratio. XRD identified starkeyite and hexahydrite as possible hydrated Mg-sulfates represented here. (B) Spherical crystals (right) and radial stars (left top) with Fe-O signatures ('Fe') in a 10:1 ratio. These two forms could be representative of different stages of growth.

coatings containing significant amounts of Si. While no distinct crystalline shapes could be observed, the coatings did have a Mg-sulfate signature in EDS, potentially correlating to the XRD sulfates. The thick gels that resulted in these experiments were very difficult to completely rinse away, similar to the plagioclase experiment. We hypothesize that fluid entrained in the remnant gel contributed Mg-sulfates to the analysis of alteration grain products and that Mg-sulfates were not forming during the alteration stage of experiments. This was supported by evaporation of experimental fluid from olivine experiments. Mg-sulfates precipitated, similar to pyroxene fluid evaporation results. XRD of evaporation products showed pentahydrite ($MgSO_4 \cdot 5H_2O$) and kieserite and amorphous Mg-sulfate crystals occurred in SEM images (Table 5).

The only distinct forms found in SEM images of these experiments were occasional micron to submicron spheres with an Fe-O EDS signature, an Fe-oxide or –hydroxide mineral that may be hematite or goethite (Table 5; Figure 22). In addition to the more common sphere shape, the Fe-O targets also formed as a collection of radial spindles, resulting in a star-like form.

3.3.1.4 Cerro Negro 1999 Cinders

The final stage of experimental work reacted whole rock cinders from the 1999 eruption of Cerro Negro. Since component minerals were reacted individually, those results helped interpret whole rock reaction pathways. CN basalt is unusually phenocryst-rich, composed of basaltic minerals with compositions similar to those of the minerals that were individually reacted, as well as volcanic glass (Table 3). Additionally we observed how the rock reacts as a whole, as opposed to individual components. Similar to plagioclase and olivine experiments, a translucent gel layer formed on top of the cinders (Figure 18D). The color and cohesiveness of

the gel was observed to change slightly based on the fluid:rock ratio. With increasing fluid:rock ratio it became more cohesive and restricted the degree of iron oxidation that could occur, resulting in a less orange-tinted gel. Alteration products measurable in XRD were gypsum and occasional alunogen (Table 5; Figure 23A). There was also a minor amorphous Si bump at 18-22 2θ that could have been caused by the gel layer present or amorphous silica replacing phenocrysts (Figure 19D). This is the only silica secondary product and may represent weathering of volcanic glass. Microscopic examination with SEM/EDS identified Fe-sulfate and more complex sulfates with Al-Na (natroalunite) and Mg-Al as the cations (Table 5; Figure 23B-D).

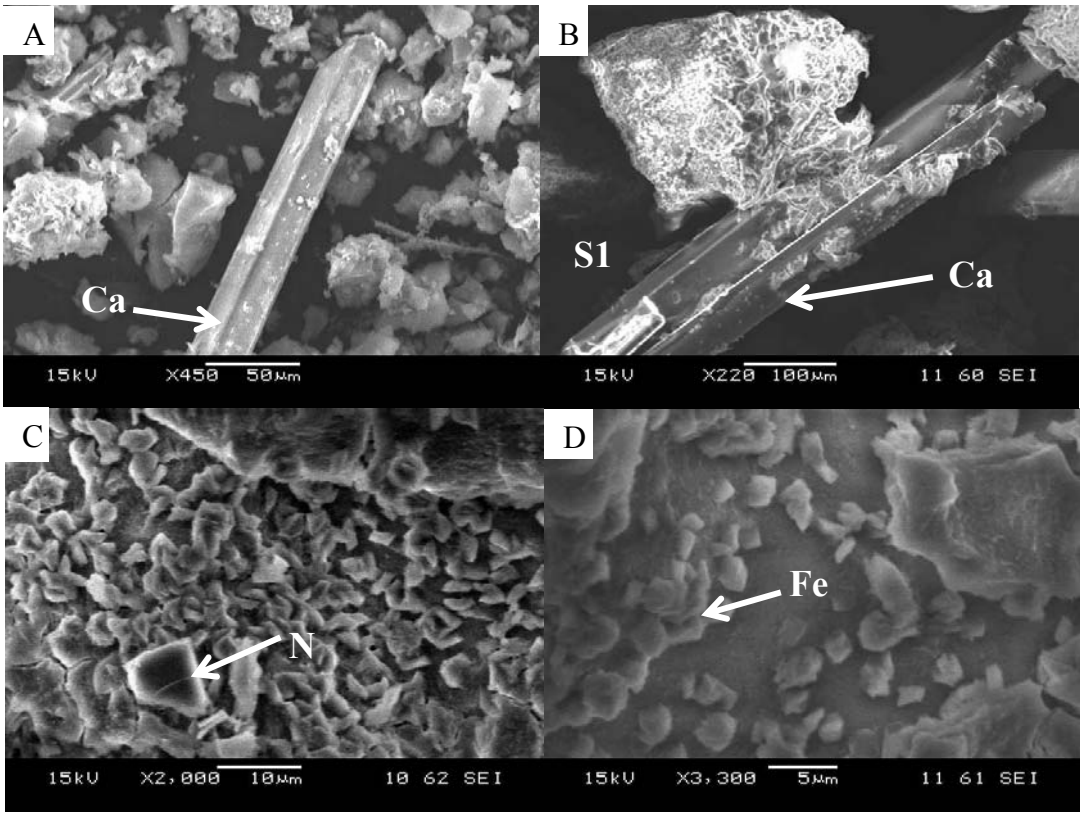

Figure 23. SEM images of products from the alteration of CN 99 and 1m H_2SO_4. (A, B, C) From the 4:1, 12-day experiments. (D) From the 1:1, 12-day experiment. (A) Rod of Ca-sulfate ('Ca'). (B) Rod of Ca-sulfate. The lighter mineral is a mixed Mg-Al sulfate ('S1'), potentially two separate components—Mg-sulfate covered by amorphous Al-sulfate. (C) Na-Al sulfate, natroalunite ('N'). (D) Fe-sulfate (Fe).

Evaporation products analyzed with XRD were composed of alunogen and hexahydrite. The hexahydrite may be related to pyroxene dissolution and evaporitic processed (Table 5). In SEM, evaporitic products from the 10:1 ratio experiments showed crystalline products, which consisted of a Mg-Na sulfate that we could not identify. The models (see Section 3.4.4) predicted the formation of mirabilite ($Na_2SO_4 \cdot 10H_2O$), which could suggest that the Na portion of this unknown sulfate was a similar mineral.

3.3.2 High Temperature Experiments

To investigate the influence of formation temperature on alteration mineralogy, we ran experiments at three temperatures: 65, 150, and 200°C. Due to experimental and equipment limitations for high temperature acidic experiments, we completed fewer 150 and 200°C experiments. This set of experiments was further abbreviated, because the first high temperature experiments completed resulted in alteration products similar to those within the 65°C experiments. The most noticeable difference between the 65°C experiments and high temperature experiments occurred in the olivine alteration, in which light green grains altered to a dark purple color, rather than orange. This was an effect of Fe oxidation and a statement to the differences between the Parr and Savillex container seals.

Additional 15-day experiments were completed for pyroxene and olivine, which GWB models indicated would have different alteration at greater reaction progress, including phyllosilicates. However, the family of secondary and evaporitic products again matched both shorter and lower temperature reactions. Microscopic changes in mineral crystal form, size, and abundance were observed in SEM images, similar to the changes seen due to duration and fluid:rock ratio at 65°C. For pyroxene experiments, the evaporitic Mg-sulfates present at higher temperatures were spherical forms and often clumped. The Ca-sulfate in these experiments was

larger and blade-like in structure compared to the rectangular shapes of 65°C. Natroalunite crystals formed in plagioclase alteration increased in abundance in higher temperature experiments (Figure 20D). Corollary thermodynamic models predicted products that matched experiments.

3.3.3 Fluid composition

Based on ICP-AES fluid analysis data, the species abundances for *in situ* experimental fluid composition were very similar for a given mineral and largely correspond to the composition of the primary mineral (Table 4; Table A3; Table A4). The general order of cation abundances for pyroxene were Ca>Mg>Fe>Si>Al (due to trace impurities in primary minerals there were minor amounts of Na>Mn>K that do not play a significant role in fluid speciation). Olivine followed a similar pattern in the elements that overlap: Mg>Fe>Si (with trace amounts of Ca>Mn>Na from impurities in starting material). General plagioclase elemental trend from greatest to least concentration was Al>Si>Na>Ca (Mg>Fe>Mn from impurities). Finally the CN 99-chemical trend was dominated by a combination of plagioclase and olivine: Al>Mg>Fe>Na>Ca>Si>Mn, in general. Notably the Si content was much lower than plagioclase or olivine.

The fluid speciation was used to determine the saturation states of minerals (Table A5; Table A6). Saturation state is an indication of whether a fluid is concentrated enough to precipitate a given mineral. In general, the saturation states and minerals were comparable within a given fluid:rock ratio between plagioclase and CN 99 cinder and the lower fluid:rock ratios had overall higher saturation indices, including many phyllosilicates. Pyroxene and olivine had similar mineral saturation indices for sulfates and silica polymorphs. In the 12- to 60-day, 1:1 ratio CN 99 experiments, Na and K were below the detection limit, so no

natroalunite or alunite were predicted to form. The 10:1 plagioclase and CN 99 experiments had measurable K and thus alunite was a potential mineral phase, in addition to natroalunite. Overall, plagioclase and CN 99 cinders had more than twice the possible minerals than pyroxene and olivine. This suggests that plagioclase was responsible for greater secondary mineralogy diversity in whole rock experiments. The mineral supersaturation values for plagioclase and CN 99 cinders were all much higher than pyroxene and olivine ones. The supersaturated values corresponded to a number of phyllosilicates and natroalunite. For all experiments, silica phases and Ca-sulfates gypsum, anhydrite, and bassanite ($CaSO_4 \cdot 0.5H_2O$) were close to equilibrium. Also similar between the starting materials, Mg-sulfates, hexahydrite, epsomite, and kieserite were undersaturated and would not precipitate until the fluid became more concentrated.

Because Mg^{2+} was a relatively conservative element and stayed in fluid until evaporation began, primary mineral dissolution can be estimated by the accumulation of Mg^{2+} in the fluid. However, plagioclase had trace to no Mg^{2+} or other conservative element; therefore, dissolution was not calculated for plagioclase. The calculated degree of dissolution did not take into account all elements or potential chemical interaction and should only be considered relative to each other, not as absolute dissolution. Fluid data from ICP-AES were reported as parts per million (ppm). Mass loss from dissolution was estimated using the trends in fluid concentrations. Assuming no Mg^{2+} in the initial acidic fluid, all Mg^{2+} measured in fluid was a direct result of mineral dissolution. As an example calculation, if there was a 300 mmolal (mmol/kg water) increase in Mg concentration and 2.7 g of water, then there were 0.81 mmol of Mg^{2+} in the entire fluid. This Mg^{2+} abundance was related to mineral weight using the mole fraction of Mg in the mineral and the mineral formula weight. For example 0.87 mol Mg/mol pyroxene (augite) with a formula weight of 220.75 g/mol resulted in 0.21 g of dissolution, or 7%. The calculations were

Table 4. Experimental Fluid Composition[1]

	65°C 4:1			65°C 1:1		65°C 10:1		150°C 4:1	200°C 4:1	
	Day 3	**Day 12**	**Day 40**	**Day 3**	**Day 60**	**Day 3**	**Day 60**	**Day 1**	**Day 1**	**Day 15**
Pyroxene										
Al^{3+}	4.22	5.89	6.38	39.5	38.3	4.53	8.84	13.9	17.8	1.78
Ca^{2+}	52.3	47.4	42.6	29.4	15.2	8.2	48.5	44.9	16	3.32
Fe^{2+}	18.3	29.1	38.5	45.8	93.4	5.65	23.5	41.7	65.2	18.6
K^{+}	0.422	0.367	0.219	0.692	n.d.	n.d.	n.d.	0.878	0.959	n.d.
Mg^{2+}	42.2	63.7	82.4	163	311	19.7	69.8	112	176	308
Mn^{2+}	0.464	0.78	1.05	0.845	3.77	0.101	0.625	1.08	1.71	2.8
Na^{+}	2.39	3.25	4.5	3.94	11.4	0.764	2.77	5.64	8.69	7.27
SO_4^{2-}	883	895	875	992	606	940	925	621	689	471
SiO_2(aq)	5.88	5.6	5.64	3.25	4.58	4.4	5.12	11.3	16.8	19.9
pH	0.256	0.28	0.322	0.379	1.627	0.145	0.264	0.659	0.698	1.328
Plagioclase										
Al^{3+}	491	471	410	287	51.4	358	525	243	74.2	--
Ca^{2+}	16.1	15	13.2	7.82	5.83	21.6	16.7	9.81	8.19	--
Fe^{2+}	4.9	4.63	6.24	3.82	0.64	3.3	2.22	1.13	0.344	--
Mg^{2+}+	6.45	6.31	6.24	9.84	11.5	3.71	4.52	10.4	9.24	--
Mn^{2+}	0.09	0.089	0.088	0.083	0.129	0.059	0.082	0.155	0.123	--
Na^{+}	79.6	72.7	56.8	71.3	0.147	60.9	78	11.5	0.756	--
SO_4^{2-}	807	767	668	447	95	706	851	420	186	--
SiO_2(aq)	97.3	18.1	4.66	2.32	2.13	14.4	4.47	14.5	14.3	--
pH	2.994	3.063	3.057	3.812	3.27	2.007	3.007	2.501	1.826	--
Olivine										
Ca^{2+}	1.59	1.77	2.5	2.67	1.67	1.02	1.19	2.11	1.81	1.41
Fe^{2+}	71.7	17.1	0.47	4.43	0.32	85.9	13.6	68.3	30.2	23.6
Mg^{2+}	916	1040	1060	941	834	856	1080	1020	784	651
Mn^{2+}	1.37	1.56	1.46	1.38	1.04	1.3	1.69	1.77	1.21	0.968
SO_4^{2+}	993	1060	1060	950	838	1020	1100	1170	830	677
SiO_2(aq)	35	3.7	3.08	2.41	1.8	19.6	3.6	13.7	14.1	13.3
pH	3.634	3.289	4.149	4.105	5.196	1.913	3.429	1.965	2.665	4.188
CN 99 cinder										
Al^{3+}	254	278	320	203	9.57	182	240	--	--	--
Ca^{2+}	12.6	13	12.6	12	8.25	22.1	17.8	--	--	--
Fe^{2+}	69.3	33.5	7.77	34.5	0.55	38.4	51.5	--	--	--
Mg^{2+}	184	194	165	181	181	81.5	82.6	--	--	--
Mn^{2+}	1.31	1.41	1.22	1.36	1.37	0.62	0.804	--	--	--
Na^{+}	16.2	2.71	0.219	2.99	n.d.	16	29.1	--	--	--
SO_4^{2-}	659	660	661	535	206	576	687	--	--	--
SiO_2(aq)	4.87	4.48	4.44	7.93	1.78	7.74	3.52	--	--	--
pH	3.054	3.083	3.162	3.125	3.57	1.631	1.707	--	--	--

[1]Units in mmolality

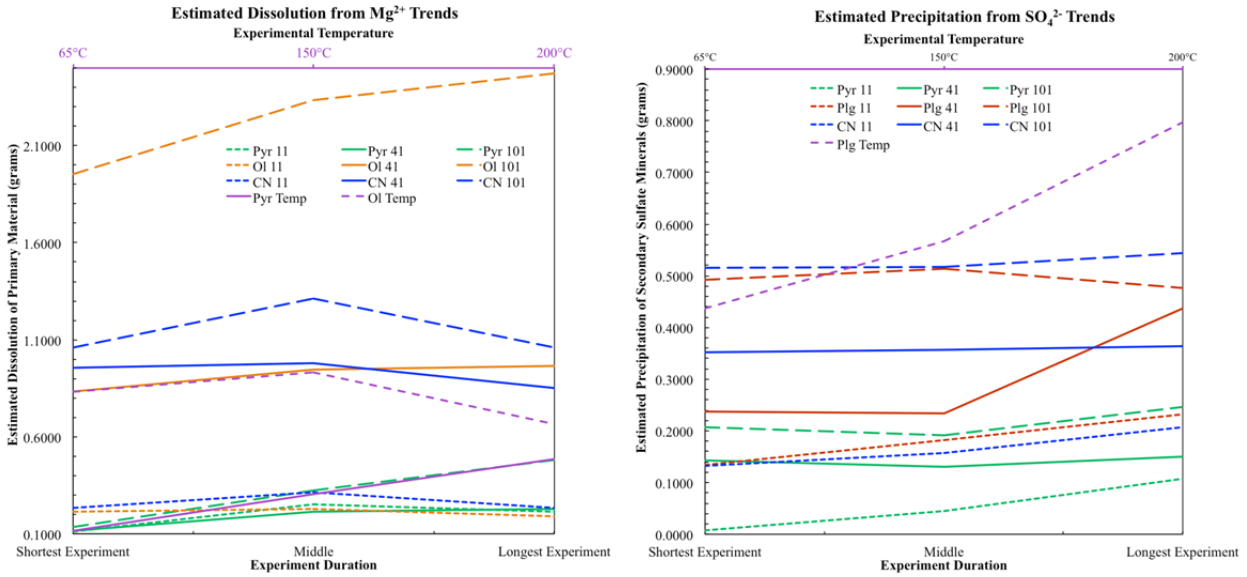

Figure 24. (A) Plot that demonstrates the degree of primary mineral dissolution. (B) Plot that demonstrates the trend of secondary sulfate mineral precipitation. Green, orange, and blue lines correspond to the main horizontal axis, Experimental Duration. Green lines show pyroxene data; orange lines show olivine data; red lines show plagioclase data; blue lines show CN basalt data. Dotted lines are for the 1:1 fluid:rock ratio; solid lines are for the 4:1 ratio; dashed lines are for the 10:1 ratio. Purple lines correspond to the second temperature axis donated in the top of the plot, Experimental Temperature.

most informative in pyroxene and olivine experiments that had abundant Mg^{2+}. Overall, the greatest degree of dissolution occurred in the highest fluid:rock ratio experiments and increased with temperature (Figure 24A). However, CN fluid tended to have a small decrease between the longest and middle duration experiments.

Additionally, olivine was an exception as well with the least degree of dissolution at the highest temperature. Among the primary reactants with Mg, olivine had the relatively greatest dissolution, demonstrated by the high fluid concentration of Mg^{2+} relative to its abundance in the olivine mineral. To estimate the amount of precipitation of secondary minerals, the change in sulfate anion concentration due to the precipitation of sulfate minerals was used. This was a rough estimate that only takes sulfate into account and does not consider multiple mineral

formations. The numbers presented here should only be taken relative to each other. Additionally this sulfate change cannot be directly correlated to a mass amount of precipitated secondary minerals because corresponding cations and waters, which would contribute to this total weight, were not included. Regardless, the calculated quantity of sulfate deposition was the same order of magnitude as the weight added and it provided a means to compare relative precipitation of minerals. Since olivine did not precipitate sulfate during the alteration stage of experiments, sulfate anion could not be used to estimate the amount of secondary products produced. Assuming an initial sulfate concentration equivalent to 1 molal, the decrease in the concentration at the termination of experiments was determined with ICP-AES measurements. The difference was converted into a weight using the amount of fluid used. For example if there were a difference of 400 mmolal and there was 2.7 g of water in that experiment then that equates to 1.08 mmol of sulfate. Using the formula weight, the moles were converted to 0.103 g of overall sulfate loss from fluid, or precipitation. Overall, precipitation was greatest at larger fluid:rock ratios and higher temperature (Figure 24B). Plagioclase, followed by pyroxene then olivine, had the most rapid consumption of sulfate related to the formation of sulfate minerals. The rate of consumption for the CN 99 cinders was most similar to plagioclase.

3.3.4 Geochemical Models of Alteration

3.3.4.1 Plagioclase (bytownite)

Geochemical models were created representing each experiment to aid in the interpretation of experimental and field results [*Marcucci et al.*, submitted]. Plagioclase models were set up to react 1m H_2SO_4 with the pure plagioclase mineral, as occurred in the experiments. For example, the model that replicated the 4:1 plagioclase experiments consisted of 3g of solid reactants in the 'Reactant' tab in GWB and sulfuric acid and temperature listed in the 'Basis'. O_2

fugacity was set to atmospheric to represent the air in the sealed reaction vessels. Oxide composition (Table 3) was used to represent the correct elemental proportions in the solid mineral. For this example there was 1.48g of SiO_2, 0.98g of Al_2O_3, 0.46g of CaO, and 0.08g of Na_2O. The sulfuric acid was added as a solution of water and sulfuric acid (sulfate anion and protons) for a total molality of one. The sulfate ion was the charge balancing element and pH was 0.075.

Total sulfate concentration in the experimental fluid as measured by ICP-AES was used as a tracer to compare the extent of reaction progress between the models and experiments. In the above example for 65°C, the measured final experimental sulfate concentration was approximately 700 mmolal, which matched the model concentration after 30% of the equilibrium reaction had taken place, or reaction progress of 0.3. The first approximately 20% and 60% of the models were representative of 65°C 1:1 and 10:1 experiments, respectively. For 150 and 200°C, the reaction progresses were 50% and 70%, respectively (Table A1). The model products matched experimental results with the two main products of the model being amorphous silica and natroalunite (Figure 25A). Inconsistent with experiments, the Ca-sulfate anhydrite was predicted in the weathering reaction models; however, gypsum was formed in experimental products, which may be remnant of fluid evaporation under ambient conditions. Some production of diaspore occurs at the end of the predicted reaction progress, which may be related to the Al-rich gels in experimental observations.

3.3.4.2 Pyroxene (augite)

Pyroxene models were set up in the same manner as above, but with pyroxene composition replacing the plagioclase ones. Based on the measured sulfate component, the first 10%, 20%, and 30% of the models were representative of the 1:1, 4:1, and 10:1 65°C experiment

ratios, respectively (Table A1). Matching steps for higher temperatures were 10% for 150°C and 50% for 200°C. Anhydrite was observed in experimental results and was also predicted to form in the models (Figure 25B). Amorphous silica was predicted to form in the models, but silica phases were not observed in experimental results. Consistent with the determination that Mg-sulfate was an evaporitic mineral in the experiments, models were unsaturated with respect this minerals.

3.3.4.2 Olivine (forsterite)

The alteration models were set up the same ways as previously discussed. These were the only experiments did not have sulfates forming during the actual alteration progression; therefore, sulfate could not be used as a reaction progress tracer. Mg^{2+} was a conserved element until evaporation. The increase in Mg as olivine was dissolved was used as a tracer in these models and indicated reaction progresses of 10%, 30%, and 70% for 1:1, 4:1, and 10:1 ratio at 65°C, respectively. Both 150 and 200°C model reaction progress was 30%. The iron in this system was particularly sensitive to the presence of $O_{2(g)}$. Models taking Earth atmospheric oxygen fugacity into account predict the formation of hematite, possibly correlating to the spheres observed in experiments (Figure 25C). Also predicted to form were amorphous silica, talc, and antigorite. Amorphous silica was related to the Si-rich gel seen in experiments. The phyllosilicates talc and antigorite were not observed in experiments, which was likely due to a kinetic inhibition or lack of maturation time.

3.3.4.4 Cerro Negro 1999 Cinders

GWB models were designed to represent CN 1999 cinders based on its oxide composition data (Table 3). Typical products include anhydrite and a silica phase, as well as,

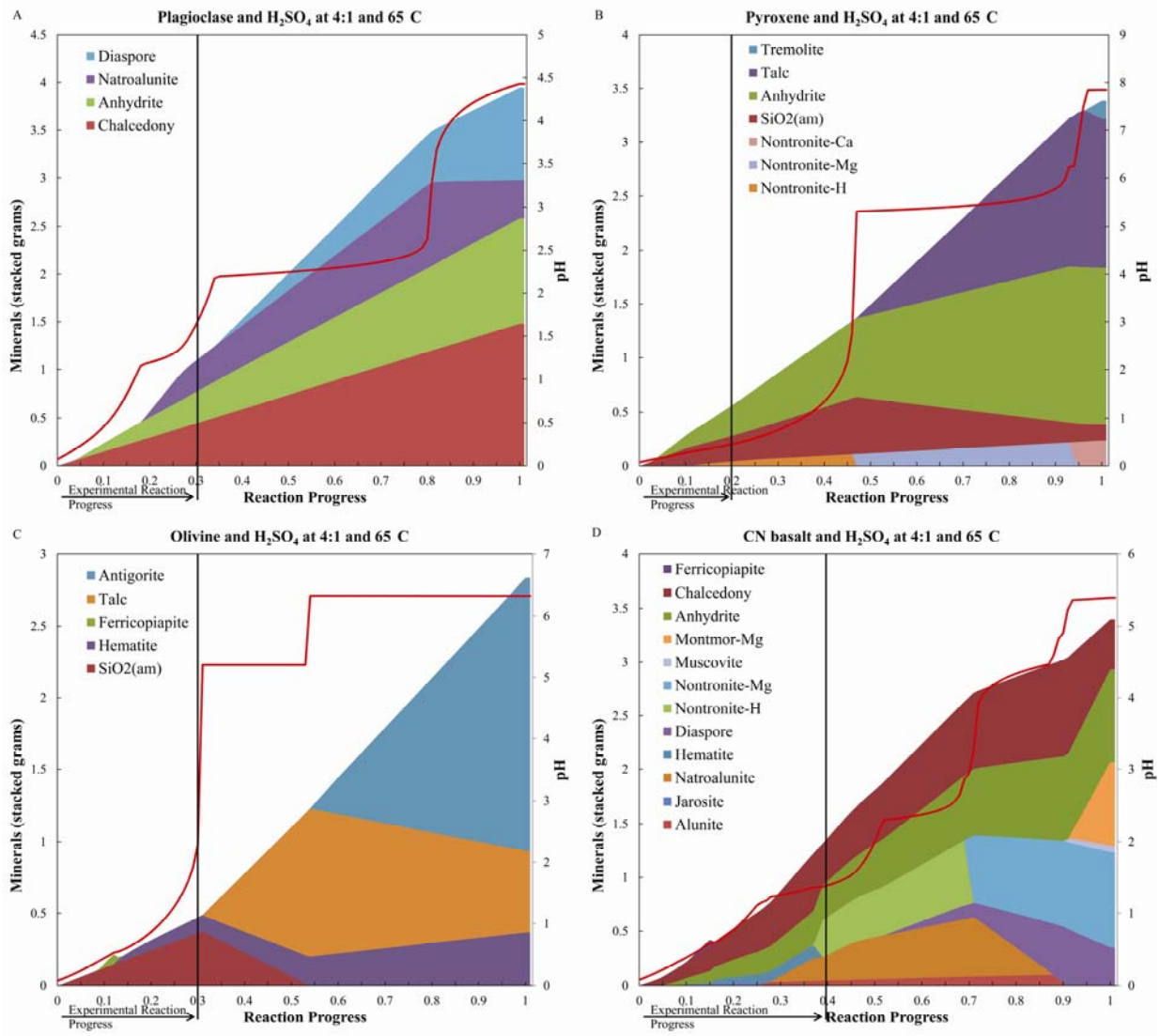

Figure 25. Plots of model reaction progress, representing sulfuric acid and mineral reactions, produced using data from Geochemist's Workbench models. These are stacked plots with the area representing the amount of minerals formed. pH is presented as a red line with a numerical right axis. Determination of reaction progress is explained in the text. (A) Example of thermodynamic reaction between 3 grams of plagioclase and 12 grams of sulfuric acid at 65°C. (B) Similar reaction for pyroxene. (C) GWB model for olivine. (D) Model for the alteration of Cerro Negro basalt cinders.

smaller quantities of jarosite, alunite, natroalunite, and hematite (Figure 25D). Distribution and quantities were dependent on fluid:rock ratio and temperature. As fluid:rock ratios decreases, the solution becomes saturated after reacting with less solid material then needed for a high

fluid:rock ratio, allowing earlier mineral formation. Also at lower fluid:rock ratios and further reaction progress at higher ratios, phyllosilicates were predicted to form, as in individual plagioclase experiments. Phyllosilicates were not observed in experiments despite model prediction. At higher temperatures, fewer minerals were predicted to form.

3.4 Summary of Experimental Results

The experimental and model experiments we conducted collectively give insights into basaltic acid-sulfate alteration. At the start of the experiments, the fluid was speciated with H^+, H_2SO_4, HSO_4^-, and SO_4^{--}. The weathering reactions dissolved the primary mineral, releasing cations into solution. After the Fe^{2+} was released, it oxidized to Fe^{3+} and minor amounts of iron oxides formed in olivine experiments. Over time, cation (Ca^{2+}, Mg^{2+}, Na^+, etc.) concentrations increased until they reached a saturation state with the sulfate ion, and began to precipitate secondary sulfate minerals. In our experiments, these were anhydrite in pyroxene experiments and natroalunite in plagioclase experiments. At the end of the experiments, the evaporation process increased the saturation of remnant fluid and Mg-sulfates and gypsum formed evaporitic deposits.

3.4.1 Effects of duration

All secondary minerals observed in the longest timestep were also observed in the shortest. Changes in duration manifested in much subtler ways evident in SEM images, including form, size and abundance. This can be observed in the continued decrease of SO_4^{2-} in the fluid as sulfate minerals precipitation (Figure 24B) and the buildup of conservative elements, like Mg^{2+}, as reactants dissolve (Figure 24A). Size and abundance change in a more intuitive way. As duration increases, minerals have a longer time to form and grow as more material becomes available. The seven and half month long experiments at 65°C and 4:1 fluid:rock ratio

continued to follow this trend (Figure 18B and Figure 18F). The Ca-sulfate changed form, in addition to size and abundance. Shorter experiments produced rectangular prism crystals; the longer experiments had larger, blade-like ones. During this longer time, new secondary minerals such as phyllosilicates did not appear to form, indicating that even longer maturation times, nucleation, or an increase in pH from rock buffering were needed.

3.4.2 Effects of fluid:rock ratio

The crystal size, abundance, and shape variations from SEM images hold true for fluid:rock ratio changes. With a lower fluid:rock ratio it was easier to saturate the fluid and precipitate minerals. These have relatively more crystals, which ultimately have a longer time to grow larger. This is demonstrated in Table 4, where ion concentration increased more quickly at the lower fluid:rock ratios then at higher ones. However, a lower ratio also means the fluid was more easily buffered and loses its ability to dissolve the primary minerals. Changes in crystal morphology were most evident in the Mg-sulfates formed in pyroxene evaporation experiments (Figure 21B, C, and D). This shape change could be a change in the specific hydration state of the Mg-sulfate, although they have not been identified. The macroscopic observed gels in plagioclase, olivine, and CN basalt experiments increased in thickness with increasing fluid:rock ratio from less than ~0.5 centimeters for 1:1 to between 0.5 and<1 centimeter for 10:1 (Figure 18DFigure 18G).

3.4.3 Effects of temperature

As with duration and fluid:rock ratio, changes in temperature resulted size, shape, and abundance differences based on SEM images. In the plagioclase experiments, the abundance of natroalunite crystals increased with temperature, although their size was about the same. The stability fields of natroalunite and anhydrite cross into lower sulfate activities as temperature

increases, resulting in longer growth times overall. In the pyroxene experiments, the size and form of Ca-sulfate crystals changed with temperature. The lowest temperature produced thick, prism crystals that were hundreds of microns long and tens thick. At 150 and 200°C, the crystals were shorter, less than one hundred microns. However, there were differences even between these two temperatures. The 150°C crystals were layered and wide (rectangular prismatic); whereas, at 200°C they were much thinner acicular-crystals.

3.4.4 Fluid saturation

Lack of phyllosilicates in experiments despite thermodynamic model prediction indicated that they were kinetically inhibited, have not had time to mature, or were there but hard to detect with XRD and SEM. We favor a combination of the first two. Fluid composition showed that the fluid was supersaturated with respect to phyllosilicates (Table A6), but model results predicted their formation. This is consistent with results from [*McCollom et al.*, 2013]. The Al-rich amorphous silica gel present in plagioclase, olivine, and CN rock alteration may be a precursor for phyllosilicates. This would be supported by the fact that experiments have not reached equilibrium and the infrequent but measureable quantities of phyllosilicates at CN [*Hynek et al., submitted*; *Marcucci et al.,* submitted]. Geochemical models of *Berger et al.* [2009] also showed a progression of amorphous silica and jarosite transitioning to other sulfates, and then to phyllosilicates. Al-phyllosilicates, such as kaolinite and montmorillonite, can form in acidic volcanic environments and are generally more resistant to acidic and thermal weathering than Fe/Mg-smectites [*Fialips et al.*, 2000; *Ece et al.*, 2008; *Altheide et al.*, 2010; *Gavin and Chevrier*, 2010], although they are still not present here.

A discrepancy between the fluid chemistry saturation states and the observed experimental products lies in the supersaturation of natroalunite in plagioclase and Cerro Negro

cinder experiments. Natroalunite was observed in both of these cases; therefore it should have been in equilibrium with the fluid. This could be explained by the fluid changing as it cooled prior to analysis or that the thermodynamic data used were inaccurate under these conditions. Plagioclase experimental fluid had a much higher silica concentration than the other experiments. This may have been due to some of the amorphous Si gel being accidently taken up during fluid sampling.

In general, the low fluid:rock ratio and high temperature experiments became saturated the quickest and subsequently consumed elements through precipitation. The 10:1 fluid:rock ratio had the most dissolution based on Mg^{2+} calculations (Figure 24). The larger quantity of acid would require more abundant material to increase the pH during dissolution; therefore retained its acidity for continued dissolution of primary mineral. Increased temperature also increased the amount of dissolution in all cases except olivine (Figure 24). This may be related to rapid silica precipitation that cuts off surface reactions [*Jonckbloedt*, 1998]. This may also explain when CN basalt experimental fluid had a slight peak in dissolution at an intermediate experimental duration.

Pyroxene and olivine had fewer mineral phases that were kinetically inhibited, as indicated by the lower saturation indices. This may be due to the ability of plagioclase and CN 99 cinders to buffer the fluid chemistry to higher pH, which created a stability field for a greater number of minerals like phyllosilicates, as well as, those primary materials having more elements available. Based on the rate at which sulfate was consumed, plagioclase and CN 99 cinders precipitate sulfates most quickly because their chemistry supports the formation of multiple sulfates, i.e. complex sulfates like natroalunite and Ca-sulfates (Figure 24B).

3.4.5 Cerro Negro basalt weathering

In our experiments, we found that plagioclase and olivine weathered faster than pyroxene, which showed very little alteration even though pH remained less than 1. This was contrary to the preferential dissolution of pyroxene over plagioclase found in the models of *Zolotov and Mironenko* [2007] and *McAdam et al.* [2008], but similar to the dominant plagioclase weathering seen in *Hurowitz et al*. [2005] experiments. There were two key differences between the studies that showed dominant plagioclase alteration and those that do not: 1) temperature and 2) experimental vs. model method. The experiments conducted in this study and those of *Hurowitz et al.*, [2005] used a high temperature, 65°C and 75°C respectively, while the thermodynamic models used 0°C [*Zolotov and Mironenko*, 2007; *McAdam et al.*, 2008]. This may indicate that temperature played a role in the dissolution rate of plagioclase, in addition in pH. A second point to consider was the different methods used for the studies, modeling vs. experimentation. Modeling often uses far from equilibrium thermodynamics so that kinetic relationships represent either dissolution or precipitation, but not both. The experiments presented here had simultaneous dissolution and precipitation, which was consistently evolving the fluid chemistry.

At the start of our weathering, plagioclase dissolved and released cations Ca, Al, and Na, which lead to formation of anhydrite (Ca) and natroalunite (Al-Na), consistent with other whole rock experiments on Cerro Negro basalt [*McCollom et al.*, 2013]. Mg and Fe were freed from pyroxene and olivine. The Fe contributed to sulfates, both Fe-sulfate and traces in more complex ones, or Fe-oxide spheres. There was a lack of abundant Fe-oxide spheres likely due to inadequate maturation time and kinetic inhibition. Mg accumulated in fluid, but did not reach a point of saturation until evaporation began, at which point Mg-sulfates precipitated. A

combination Mg-Al-sulfate not observed before was observed in EDS. We suspect this is a combination of evaporitic Mg-sulfate from entrained fluid on top of fans of Al-sulfate from the gel, which cannot be distinguished in the SEM images.

Si was released from all minerals; it was most noticeable in amorphous deposits from plagioclase and olivine weathering. While a Si-rich gel was prevalent in experiments, phyllosilicates were not observed, although they were predicted in models. Phyllosilicates are not very crystalline, which makes them hard to detect with methods such as XRD. Conversely, they may not have formed yet due to kinetic inhibition and the gel material may have been a precursor material. With even longer experiment durations, the gels could transform into more stable phyllosilicates phases through Ostwald ripening [*Steefel and Van Cappellen*, 1990]. Over time, phases that initially precipitated can transform into more thermodynamically stable phases as the fluid continues to change. The models presented in this paper were used as a comparison tool to examine reaction pathways of experiments and related to field observations; therefore phyllosilicates were not suppressed. However, similar models that did suppress phyllosilicates had alteration mineralogies that to first order matched the results presented here [*McCollom et al.*, 2013]. The main difference was the presence of kieserite, which was likely a result of low fluid:rock ratio.

3.4.6 Comparison to previous studies

It is important to note that the types of sulfates detected in this series of experiments and models are similar to those seen in previous experiments by *Banin et al.* [1997], *Tosca et al.* [2004], *Golden et al.* [2005], *Hurowitz et al.* [2005] in particular, the Ca-, Al-, Mg-sulfates, as well as, amorphous Si. However, one restriction of previous studies was the influence of evaporation. *Hurowitz et al.* [2005] separated evaporitic and alteration phases, but found that

sulfates only formed in the evaporitic deposits. This was in contradiction to our study, which showed that Ca-sulfate and natroalunite can form during alteration in the closed system (Table 5). Similarly, *Tosca et al.* [2004] and *Banin et al.* [1997] considered evaporation but evaporated experimental fluid on top of the grains and the sulfate was considered evaporitic. Based on the experiments completed in our study, the assumption that sulfates only form during evaporation is not valid. To understand the full reaction process, the alteration mineralogy must be separated from the evaporation mineralogy.

Additionally the thermodynamic models presented previously differ from our own models and experimental results in some ways [*Tosca et al.*, 2005; *Zolotov and Mironenko*, 2007]. A low pH alteration model had a dominant amorphous silica component, which was consistent with our results [*Zolotov and Mironenko*, 2007]. However, this model had little formation of sulfate. Additionally the Na released from plagioclase formed Na-saponite and montmorillonite; whereas, our experiments and models form natroalunite. The Meridiani evaporation model is consistent with our experimental evaporation with the formation of Ca-, Fe- and Mg-sulfates, but we argue that some sulfates form during acid-sulfate alteration and both alteration and evaporation need to be considered for this site [*Tosca et al.*, 2005]. A second Meridiani Planum model was most similar to our own and simulated the reaction of Martian basalt with pure sulfuric acid at low fluid:rock ratios and pH [*Berger et al.*, 2009]. Despite being run at temperature and atmospheric conditions of Mars, their result of amorphous silica and jarosite then Ca-, Mg-, and Fe-sulfates is consistent to the experiments and models presented here, as well as, trends in the field site alteration mineralogy [*Hynek et al.*, submitted; *Marcucci et al.*, submitted]. Our work did not produce jarosite, but this may be related to compositional differences, see Section 5.

Iron oxide forms in olivine experiments were typically spheres, but radial star growths were also observed. *Golden et al.* [2008] examined the growth of hematite spheres in hydrothermal conditions and observed that they had a radial growth pattern in a similar size range, ~1 micron, as we see in our experiments. They further demonstrated that the Meridiani Planum hematite spheres have a similar radial growth and suggested that the larger size of Martian spheres could be due to high temperatures, thus improved kinetics, or longer growth times. Crystals once nucleated would continue to grow as long as material, namely Fe^{3+}, was available. The two populations in our olivine experiments could represent different stages of mineral growth with the star forms being an earlier stage than the spheres.

3.5 Applications to Mars

The combined suite of experimental minerals matched closely with model predictions, Cerro Negro minerals, and Mars observations (Table 6). Investigation into the polyhydrated forms in Valles Marineris has suggested that the starkeyite and hexahydrite spectra best fit remote sensing data [*Bishop et al.*, 2009]. These were two of the most abundant minerals detected by XRD in our olivine evaporation experiments. Similarly, hexahydrite was seen in the CN 99 whole rock experiments, although a more hydrated Mg-sulfate, pentahydrite, was seen instead of starkeyite. These hydrated Mg-sulfates may be indicative of weathering from olivine-rich basalt, which is prevalent on Mars [e.g. *Hamilton and Christensen*, 2005; *Edwards et al.*, 2008]. Kieserite was also a possible mineral form in pyroxene experiments based on the dipyramid crystal shape, which had been detected in many locations the Martian surface, such as the Juventae, Ius, Hebes, and Capri Chasmata in Valles Marineris [*Gendrin et al.*, 2005; *Bishop et al.*, 2009].

Table 6. Comparison of Experiments, Models, Field, and Martian Secondary Mineralogy

	Experiments[1]	**Geochemical Models**[1,2]	**Cerro Negro**[3]	**Mars**[4]
Sulfate/salts	Gypsum, anhydrite, Mg-sulfates, Al-sulfate, natroalunite	Alunite ($KAl_3(SO_4)_2(OH)_6$), anhydrite, Mg-sulfate, natroalunite	Alunite, anhydrite, gypsum, Mg-sulfate, natroalunite	Gypsum, kieserite, polyhydrated sulfates, halite
Fe minerals	Possible iron oxide spherules	Hematite	Bernalite ($Fe^{3+}(OH)_3$), jarosite ($KFe_3(SO_4)_2(OH)_6$)	Hematite, jarosite, unidentified Fe3D3
Clay minerals	None observed	Phyllosilicates, smectites	Amorphous clays, smectites	Phyllosilicates, smectites
Silica	Amorphous silica	Amorphous silica	Opaline, amorphous silica	Opaline, hydrated silica

[1]This study
[2][*McCollom and Hynek*, 2005]
[3][*Hynek et al.*, 2011]
[4][*Gendrin et al.*, 2005; *Bibring et al.*, 2006; *Squyres et al.*, 2007; *Mustard et al.*, 2008; *Ehlmann et al.*, 2009a]

The fact that Mg-sulfates formed solely through evaporation in our experiments and models may imply that Mg-sulfate on Mars likely formed by evaporation. Other possibilities are very low fluid:rock ratios or in reactions over enough time for Mg-sulfates to saturate fluid. The current presence of Mg-sulfates in the observations suggests that precipitation or rewetting by flowing water is unlikely, since their highly soluble nature would have made them sensitive to the presence of liquid water. For example, the Mg-sulfates present at the MER landing sites may mean that these areas had no rain; in contrast an area that lacks Mg-sulfates, but has other sulfates, may be an area that had experienced rain or rewetting. It is also possible that subsequent precipitation did occur and the original Mg-sulfate deposits were larger than currently observed. Mg-sulfates were also largely missing at CN with some exceptions, specifically they were often found in drainage areas [*Hynek et al.,* submitted; *Marcucci et al.*, submitted]. This could be explained by terrestrial precipitation transporting and concentrating these materials.

Jarosite was not detected in our experiments, but natroalunite, an Al-member of the alunite family that is structurally related to the jarosite family was common. This could be because the chemistry of Cerro Negro, thus chemistry of the experiments, was lower in Fe and higher in Al compared to Martian basalt (Figure 16). An alternative explanation was that the jarosite detection on Mars was actually an Fe-rich natroalunite [*McCollom et al.*, 2013]. *McCollom et al.* [2013] analyzed jarosite/alunite family minerals with varying compositions using Mössbauer spectroscopy and determined that jarosite and Fe-rich alunites have similar spectra, suggesting the possibility that rover Mössbauer detections identified as jarosite may be an Fe-rich alunite member.

Ruff et al. [2011] and *Arvidson et al.* [2010] suggested possible hydrothermal origins for the Home Plate area of Gusev crater based on the presence of Si-rich material and geological context. As seen in the experiments and models, *in situ* alteration formed sulfate and abundant Si material. The highly soluble nature of sulfates, particularly Mg-sulfates, meant they were easily removed even with small amounts of water, resulting in deposits primarily composed of Si, as seen at Home Plate and Cerro Negro. Alternatively, Si could have precipitated as siliceous sinter from steam condensate; also seen at Cerro Negro in limited locales [*Hynek et al.,* submitted].

The Paso Robles soil class detailed by the Spirit rover has also been suggested for a hydrothermal origin [*Yen et al.*, 2008]. These deposits were identified as light-toned and sulfur-rich. Mineral deposits were rich in ferric sulfates, among the suggested phases were ferricopiapite, rhomboclase, hydronium jarosite, and fibroferrite [*Johnson et al.*, 2007; *Lane et al.*, 2008]. Additional silica, Mg-sulfates, Ca-sulfates, hematite, and Ca-phosphates made up the mineral assemblages of this soil class and mixtures varied on a meter to several hundred meter

scale [*Johnson et al.*, 2007; *Yen et al.*, 2008]. Fumarolic activity in volcanic centers has pH and temperature differences on these scales, which can result in mineralogical differences [*Hynek et al.,* submitted; *Marcucci et al.,* submitted]. Our experiments presented here suggest that mineral deposits in the Paso Robles soils could also vary from primary mineral differences.

Our results from laboratory experiments closely match predicted mineralogy from the thermodynamic models when evaporation was taken into consideration (Table 6). Contrary to previous experimental studies, we find that some sulfates do form during the actual alteration process, in addition to evaporation. Our experiments and models also match the mineralogy sampled at Cerro Negro, Nicaragua and detected on Mars by the orbiters and landers. However, defining characteristics of different formation parameters lay in the minute details. With these types of changes in mind, it may be impossible to distinguish formation environments on Mars using orbiter data alone. Instead microscopic detail and abundances will be necessary to identify the paleoenvironmental conditions for similar geochemical conditions on past Mars.

3.6 Conclusions

Multiple sulfate-rich deposits have been observed globally on Mars. Their widespread distribution leads to the possibility of different formation environments, although the general weathering mechanism is acid-sulfate alteration. Being able to distinguish between the different environments is useful in understanding the paleoconditions and evolution of the area. Additionally, understanding these conditions, in particular water and chemical disequilibrium, will provide data to assess the habitability of early Mars. Our work is aimed at identifying characteristics unique to a hydrothermal, volcanic weathering system. Below we highlight the results of this work.

- Plagioclase altered to natroalunite, Ca-sulfate, and an amorphous Al-Si-rich gel. Pyroxene altered to Ca-sulfate. Olivine altered to crystalline ferric oxides/hydroxides and amorphous gels. Major alteration of whole rock experiments included Ca-, Mg-, and Fe-sulfate plus natroalunite and amorphous Si-rich material.
- Comparison of the whole rock experiments to individual mineral experiments showed that plagioclase then olivine and pyroxene were responsible for alteration assemblages.
- Evaporation played an important role in forming the final mineral assemblage, forming ample Mg-sulfates and additional Ca-sulfates. It cannot be assumed that sulfates form solely during evaporation.
- Secondary mineralogy was consistent for a given starting material regardless of changes in reaction duration, fluid:rock weight ratios, and temperatures. The changes in secondary products that we have observed, which correspond to duration, fluid:rock ratio, and temperature were size, abundance, and form.

To directly respond to the key questions guiding the research:

- It has yet to be shown that different acid-sulfate weathering environments produce drastically different and distinguishing mineralogy suites. Based on experiments, microscopic imaging may be critical in determining paleoconditions present during formation.
- It will be vital to understand the entire reaction processes that occurred on Mars. The presence or lack of (un)expected minerals may be key to understanding the history. Thermodynamic models assist in the interpretation of experiments.

- In order to determine specific formation conditions at hydrothermal environments on Mars, future measurements will have to rely on microscopic imaging and a thorough understanding of contributions from various processes including precipitation and evaporation.

4. Extent and types of aqueous alteration in Coprates Chasma, Mars

Note: This chapter is in preparation for submission as: Marcucci, E.C., and B.M. Hynek. "Extent and types of aqueous alteration in Coprates Chasma, Mars." It is cited in the reference list and other chapters as "Marcucci et al., in prep." Sections have been re-numbered and figures are in text to match the formatting of the dissertation. References for this paper have been combined with others at the end of dissertation. Acknowledgements have been combined at the beginning of the dissertation.

Abstract: High-resolution spectroscopic and morphologic images of Valles Marineris chasma walls and floors provide insights into the extent and relationship of aqueous alteration in Coprates Chasma. Visible-near infrared hyperspectral images were used to identify hydrated minerals that include Fe/Mg-smectites, Al-phyllosilicates, polyhydrated sulfates, monohydrated sulfates, and hydrated silica. Thermal infrared spectroscopy from flat areas supported these findings. Textural and morphological features were identified from co-registered HiRISE and CTX images. A series of pre-rifting alteration likely resulted in deep dominantly Fe/Mg-smectites, near-surface Al-phyllosilicates, and subsurface hydrothermal hydrated silica. The large silica deposit coincided with the intersection of Coprates Rise with the chasma, suggesting a formation influence. Post-rifting alteration formed isolated Al-phyllosilicate and monohydrated sulfate deposits. Within the main chasma monohydrated sulfates formed on spurs and in floor deposits. Southern grabens with closed basins contained both types of phyllosilicates and sulfates, likely polyhydrated, that may have resulted from evaporation. Coprates Chasma is a relatively unobscured canyon that penetrates into Noachian crust and was used to characterize type, timing, and extent of aqueous alteration.

4.1 Introduction

Since the giant rift valley Valles Marineris was discovered by Mariner 9, individual chasmata have been defined and it has been the focus of many geological studies on Mars [e.g. *Nedell et al.*, 1987; *Witbeck et al.*, 1991; *Lucchitta et al.*, 1994; *McEwen et al.*, 1999; *Edwards et al.*, 2008; *Bishop et al.*, 2009; *Flahaut et al.*, 2010; *Fueten et al.*, 2010, 2011; *Lichtenberg et al.*, 2010; *Roach et al.*, 2010b]. This rift system, associated with the rise of the Tharsis volcanic complex, is a series of grabens that can be >10km deep exposing ancient stratigraphic layers [*Dohm et al.*, 2009; *Ehlmann et al.*, 2011b]. The advent of detailed imagery and mineralogical instruments showed that Valles Marineris is layered with mineralogy indicative of aqueous alteration, including phyllosilicates, sulfates, and hydrated silica [e.g. *Chojnacki and Hynek*, 2008; *Bishop et al.*, 2009; *Ehlmann et al.*, 2009a, 2011b; *Lichtenberg et al.*, 2010; *Roach et al.*,

2010b]. Remote sensing data from the Compact Reconnaissance Imaging Spectrometer for Mars (CRISM) and Observatoire pour la Minéralogie, l'Eau, les Glaces et l'Activité (OMEGA) instruments on board the Mars Reconnaissance Orbiter and Mars Express, respectively, have mapped the Valles Marineris region using visible to short wavelength infrared reflectance spectroscopy [*Bibring et al.*, 2006; *Murchie et al.*, 2009b].

These instruments have detected Fe/Mg- and Al-phyllosilicates in chasma walls [*Gendrin et al.*, 2005; *Bibring et al.*, 2006; *Bishop et al.*, 2009; *Ehlmann et al.*, 2009a; *Murchie et al.*, 2009b]. Light-toned layered deposits within the chasmata contain sulfates, such as gypsum ($CaSO_4 \cdot 2H_2O$), kieserite ($MgSO_4 \cdot H_2O$), and polyhydrated sulfates (PHS). The spectral nature of PHS can result in non-unique mineral identifications, but potential matches include hydrated Mg- and Fe-sulfates such as epsomite ($MgSO_4 \cdot 5H_2O$), hexahydrite ($MgSO_4 \cdot 6H_2O$), starkeyite ($MgSO_4 \cdot 4H_2O$), melanterite ($FeSO_4 \cdot 7H_2O$), ferricopiapite ($Fe_{2/3}^{3+}Fe_4^{3+}(SO_4)_6(OH)_2 \cdot 20H_2O$), copiapite ($Fe^{2+}Fe_4^{3+}(SO_4)_6(OH)_2 \cdot 20H_2O$), or halotrichite ($FeAl_2(SO_4)_4 \cdot 22H_2O$) [*Gendrin et al.*, 2005; *Bishop et al.*, 2009]. Ius Chasma has kieserite and PHS within closed basins and older Fe/Mg-smectite and hydrated silica layers [*Roach et al.*, 2010b]. Capri Chasma has mineral detections indicative of kieserite, PHS, and Al-phyllosilicate or hydrated silica [*Flahaut et al.*, 2010]. They formed within interior layered deposits, but the kieserite tended to occur in cliffs edges, between layers of PHS and a basal silicate material. Iani Chaos appears to be dominated by gypsum in light-toned chaotic mounds [*Glotch and Rogers*, 2007]. A sequence containing old monohydrated sulfates and hydroxylated sulfates, capped with younger ferric oxides then PHS and hematite units occur in Aram Chaos [*Lichtenberg et al.*, 2010]. In addition to hydrated sulfates in bright floor mounds, Juventae Chasma has hydrated silica in fractured layered deposits [*Bishop et al.*, 2009]. Surrounding plains areas also have hydrated silica plus

hydronium jarosite ($(H_3O)Fe_3(OH)_6(SO_4)_2$), which is suggestive of acidity and hydrothermalism [*Milliken et al.*, 2008; *Bishop et al.*, 2009].

Coprates Chasma is a canyon in the eastern portion of Valles Marineris. There have been limited structural and mineralogical studies of this chasma [*Murchie et al.*, 2009a; *Fueten et al.*, 2010, 2011; *Flahaut et al.*, 2012]. Mineralogical identifications indicate deep mafic bedrock, suggesting exposure of Noachian crust, and deep phyllosilicates [*Murchie et al.*, 2009a; *Flahaut et al.*, 2011, 2012]. Furthermore, Coprates Chasma appears to be a transitional point for Valles Marineris where ancient crust is exposed to the east, but not to the west. Two studies on the layered deposits in the western portion of the chasma show evidence of monohydrated and polyhydrated sulfates [*Fueten et al.*, 2010, 2011]. The eastern portion, near a central ridge, appears largely devoid of such interior layered mounds and is the focus of this study. This work is a study of mineral identification and continuity of mineral stratigraphy. Here, we analyzed mineralogy of the chasma walls, floors, and surrounding areas to constrain the alteration history of this key section of the Valles Marineris.

4.2 Geological Setting

Coprates Chasma is a canyon approximately 800 km long comprising the eastern portion of Valles Marineris before the start of the large chaotic terrains and outflow channels [*Witbeck et al.*, 1991]. This paper focuses on an area distinct from previous studies (roughly latitude: 12ºS to 17ºS, longitude: 307ºE to 300ºE) (Figure 26). The study area is approximately 200 km long and canyon width varies from about 75 to 100 km. A central ridge runs almost the entire length of the study section and a series of smaller grabens exist approximately 30 km south of the chasma. The elevation change from the surrounding plateau to the chasma floor ranges from

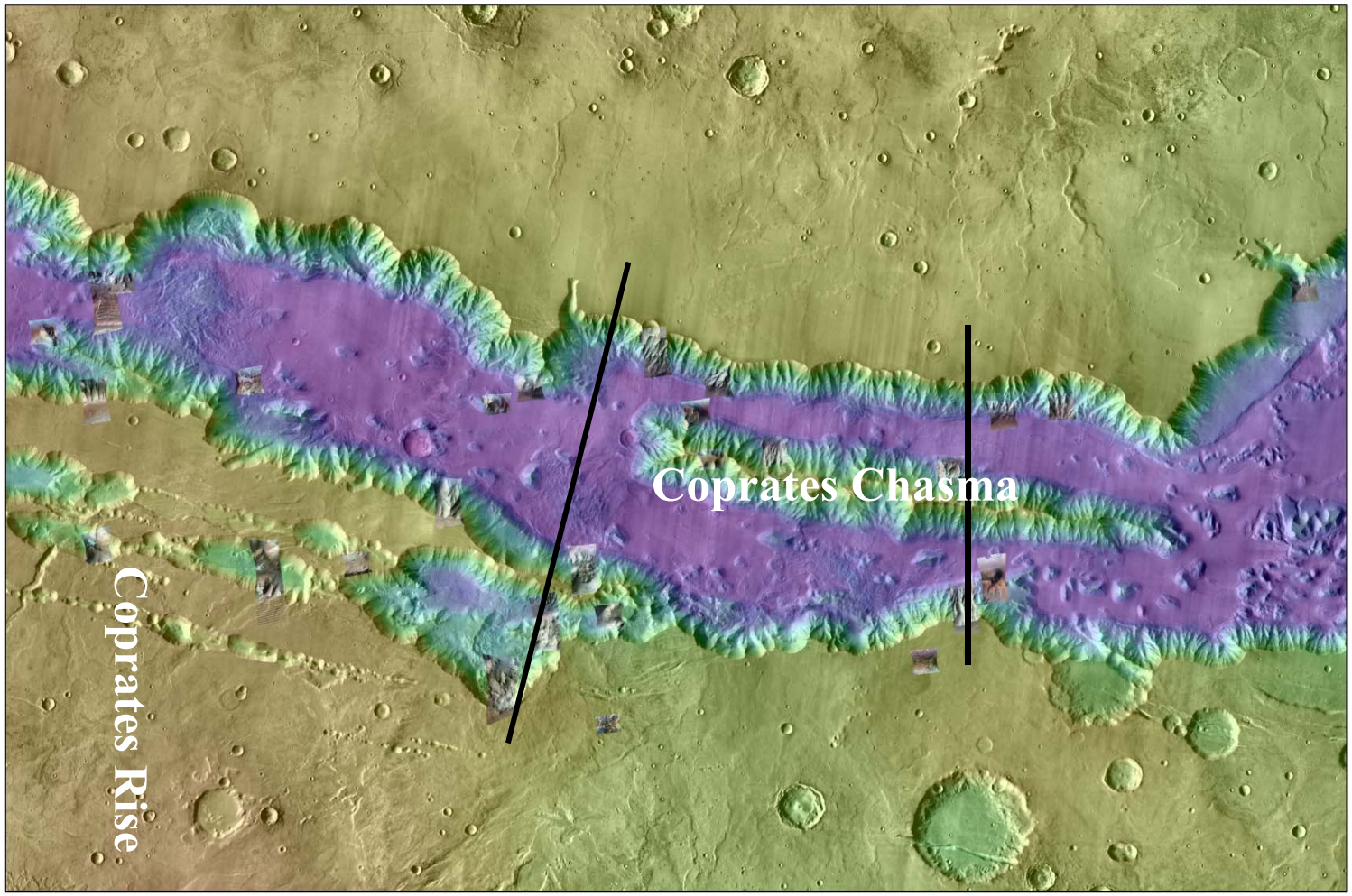

Figure 26. Context map of the Coprates Chasma field site composed of MOLA topography and THEMIS daytime visible IR data. CRISM scenes are overlain on the map. Black lines represent the cross-sectional profiles used in Figure 27.

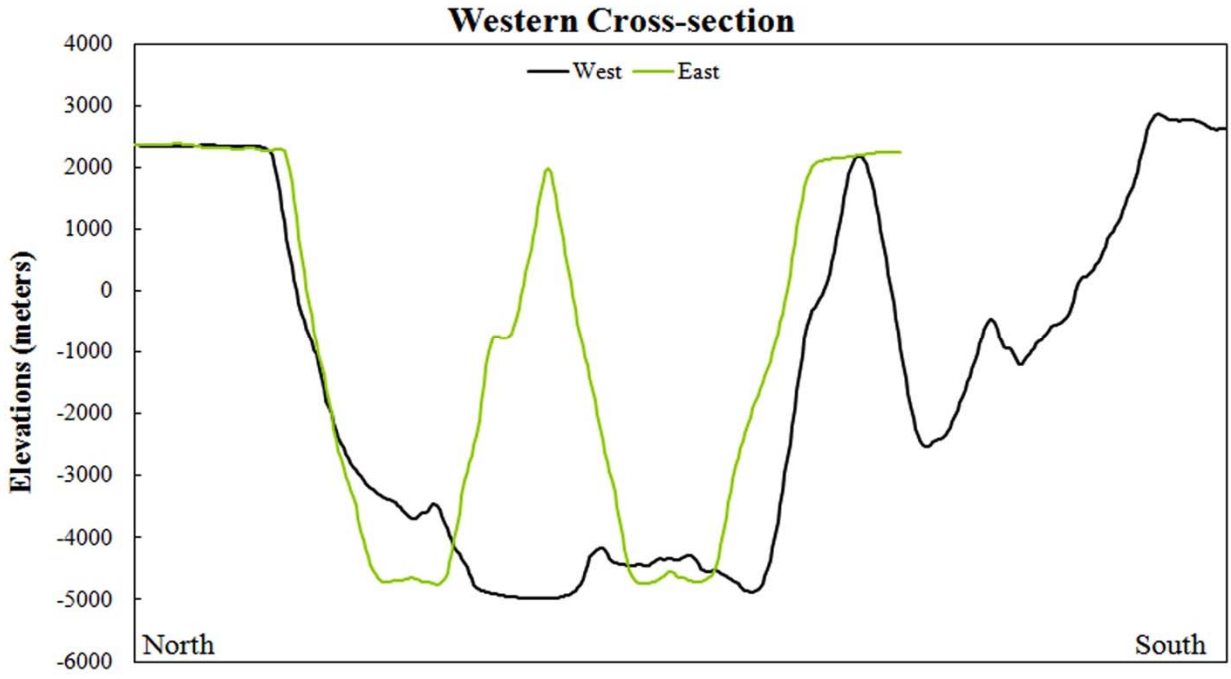

Figure 27. Cross-sectional profiles of western and eastern Coprates chasma. The western part of the chasma is generally wider, has higher absolute elevations and has additional grabens in the south plateau.

approximately 6-7 km with additional longitudinal variability. The study area of this paper encompasses the portion of the chasma that intersects with Coprates Rise, an ancient volcanic ridge part of the Thaumasia region (Figure 26). This influences the absolute elevations east and west of the intersection. The northern plateau has an eastward dipping slope with a 1000 m elevation change; the south plateau first dips ~2000 m to the east then rises 500 m.

The Coprates Chasma walls in this study area are characterized by fine layers exposed in spur and gully formations. The southern walls in the western portion of the study area appear to have experienced more mass wasting in the form of large landslides. The north and south sides of the central ridge have similar absolute elevations and morphology of spurs. Thin horizontal layers are apparent within the top 0.6-0.7 km of the walls. The spur and gully formations begin shortly below the top of the wall and extend approximately 4-5 km. Debris fans often cover the

bases of the slopes. Contrary to the other chasmata, this area of Coprates Chasma lacks significant interior layered deposits. Although there are two populations of unlayered floor mounds: irregular, angular blocks and symmetric conical shapes.

The observed morphology is broadly consistent with the general categorization of units in *Flahaut et al.* [2012], including four units: 1) thin layers in the upper wall, 2) sporadic mid-wall outcrops, 3) bright, fractured blocks low in the wall, and 4) a dark basal unit. A general mineral sequence was derived from the first year of CRISM images, which included the identification of deep Noachian-aged phyllosilicates at ~2 km absolute elevation [*Murchie et al.*, 2009a]. This phyllosilicate layer, largely consistent with chlorite material, was under- and overlain by pyroxene-bearing material. The basal unit was pyroxene and olivine-rich. The topmost units, >2 km thickness, consisted of Al-smectite over Fe/Mg-smectite with a top basalt sand.

4.3 Datasets and Methods

4.3.1 CRISM

We analyzed 30+ full and half resolution targeted long wavelength (1.00-3.92 μm) CRISM scenes (Table 7) covering approximately 15% of the study area and representing a full range of elevations along the slope walls, the capping plains surrounding the chasma, floor features (mounds and dunes), and smaller southern grabens (Figure 26). CRISM scenes were downloaded from the Mars Orbital Data Explorer PDS web interface (http://ode.rsl.wustl.edu/mars/) and imported into the ENVI/IDL software program using the CAT Tools add-in. Scenes were atmospherically corrected using the standard volcano scaled method [*Murchie et al.,* 2009b]. They were further cleaned using a custom ENVI/IDL program that removes errant band extremes. This program works on a pixel-by-pixel basis by identifying single bands within a spectrum that are anonymously high or low and replacing them by

averaging neighbor bands. Additionally a flat field was applied to each image. The flat field method applies a ratio to the entire image using a user-defined region of interest (ROI), usually a spectral bland, dusty, and uninteresting portion of the scene. It is used to remove scene-wide features, such as atmospheric peaks that were not completely corrected for, and to highlight changes in spectral bands. Regions used for the ratio were chosen carefully to avoid introducing false bands or removing real spectral features. Both flat fielded and un-flat fielded image spectra were used and compared to determine mineralogy. CRISM spectra were compared with the United States Geological Survey (USGS) and CRISM spectral libraries for mineral identification [*PDS Geosciences Node and CRISM Spectral Library Working Group*; *Clark et al.*, 2007b].

Cleaned CRISM images were manually explored for unique spectral signatures, guided by color and textural variations. Once areas with spectral characteristics of interest were identified, they were marked using the native ROI tool. The ROIs were used to define map parameters for the ENVI Orthogonal Subspace Projection mapping function. This function searches the image for pixels that have similar spectral features as defined by the ROIs. The result is a band for each ROI, which can be projected in a red-green-blue (RGB) image. Manual interactive stretching was used to set the limits of detection sensitivity. This function is similar to the built-in CAT Tools parameters defined in *Pelkey et al.* [2007]. These parameters, in particular those indicative of hydration, phyllosilicates, and sulfates, were compared to our user-defined maps with high correlation. After spectral processing, the scenes were projected into map coordinates with the CAT Tools map tool and exported to ArcMap.

4.3.2 THEMIS

Daytime infrared Thermal Emission Imaging System (THEMIS) images were used to examine longer wavelength (6-15 μm) features on flat surfaces (plateau plains and chasma

Table 7. List of CRISM images analyzed in this study.

CRISM ID	Description	Fe/Mg-smectite	Montmorillonite	Silica	Sulfate
frt00005f84	Slopes	x			
frt00008fe7	Floor mound	x			
frt00009226	Slopes	x			x?
frt0000943d	Hanging valley	x			
frt00009b24	Slopes	x	x?	x?	
frt00009d64	Base of slope				x?
frt0000a51a	Plains		x		
frt0000b6c5	Behind balcony		x		
frt0000b8e2	Slopes	x			
frt00011840	Ridge		x	x?	
frt00011df2	South graben	x	x		x
frt00012316	Ridge	x			x?
frt00023742	Slopes	x			
frt00024c3d	Slopes		x		
hrl000086ec	Plateau slopes	x			
hrl0000a8f6	Balcony	x		x	
hrl0000b30b	Slopes	x			
hrl0000cd37	Slopes	x			
hrl0000d0de	Upper slopes	x			
hrl00010d3b	Behind balcony	x	x?		
hrl00012165	Slopes, peninsula	x			x
hrl00019505	Landslide floors	x	x		
hrl00019dc2	Slopes	x		x	
hrl0001b8ae	South graben	x	x		x
hrs00004787	Base of slope	x			x
hrs00009991	Plains		x		
hrs0000bdbb	Plains		x		

floors). Radiance and emissivity images were produced using the THMPROC interface (http://thmproc.mars.asu.edu/). We processed THEMIS data following the techniques described in *Bandfield et al.* [2004]. Decorrelation stretches (DCS) highlighted compositional differences [*Gillespie et al.*, 1986]. DCS images were created using bands 9-6-4 and 8-7-5. The former highlights silicate- and sulfate-rich materials and the latter highlights mafic minerals [*Bandfield*,

2008; *Hamilton et al.*, 2008; *McDowell and Hamilton*, 2009; *Baldridge et al.*, 2012]. Emissivity spectra from selected areas were averaged with DaVinci (http://davinci.asu.edu). We compared spectra and spectral ratios to laboratory spectra of pure minerals from Arizona State University's spectral library [*Christensen et al.*, 2000a].

A visible wavelength daytime band 12 THEMIS mosaic (100 m/pixel) was also used to build the base map in ArcGIS [*Christensen et al.*, n.d.].

4.3.3 MOLA

The Mars Orbiter Laser Altimeter (MOLA) led to a global topographic map with meter-scale vertical resolution and ~150 m spot size for individual ground shots [*Smith et al.*, 2001]. We utilized this product in our analysis of Coprates Chasma for gridded elevation data at a pixel size of ~450 m. Elevations of morphological and spectral features of interest were determined in the GIS project that contained the co-registered CRISM scenes.

4.3.4 HiRISE/CTX

Morphology and textures of walls, floors, and isolated deposits were examined using imagery from the Context Camera (CTX) and the High Resolution Imaging Science Experiment (HiRISE). CTX produces images with a ~5.5 meter resolution over a larger regional area [*Malin et al.*, 2007]. We examined four scenes covering about 20% of the study area. HiRISE provides highly detailed images, 0.25 to 1.3 meter pixels, of specific targets, which are co-registered with CRISM scenes [*McEwen et al.*, 2007]. Several broad CTX images that transected the canyon were used to examine the general morphological trends, while HiRISE images that were co-registered with CRISM scenes linked textures with specific deposits.

4.4 Compositional Stratigraphic Sequences

Previous work on the stratigraphic sequence in Coprates Chasma has indicated basal units of olivine and/or low calcium pyroxene (LCP) material, mid-wall units of Fe/Mg-phyllosilicate, and top units of additional LCP material with thin Fe/Mg-smectite then Al-smectite interbedded high in this top unit [*Murchie et al.*, 2009a; *Flahaut et al.*, 2012]. The results of our mineralogical and stratigraphic analyses were mostly consistent with these layers, but we suggest a modification of the alteration mineralogy stratigraphy, especially as related to longitudinal variations. In general, the absolute elevations between the north and south are comparable, but those east of Coprates Rise are lower than those west of it by 1.5 to 2.0 km (Figure 27). Coprates Chasma was bisected by the Coprates Rise, a large volcanic region that is part of Thaumasia. The uplift created by this volcanic feature may account for the differences in absolute elevations and the added heat provided by volcanism may have also affected alteration mineralogy. Based on the stratigraphic relationships we observed, we propose there are two types of alteration that account for the types and extent of minerals observed.

4.4.1 Pre-rifting Mineralogy

Pre-rifting minerals began with the emplacement of Noachian-aged primary basal units. These basal units were characterized by LCP evident by a broad peak around 1.33 μm and a broad dip around 1.82 μm (Figure 28; Figure 29) and olivine with a broad reflective brightness starting at approximately 1.3 μm. LCP was also detected throughout the slope of the chasma and floor and served as a background signature for many alteration minerals. Olivine was less readily observed, but limited exposures at lower elevations were identified, supporting prior

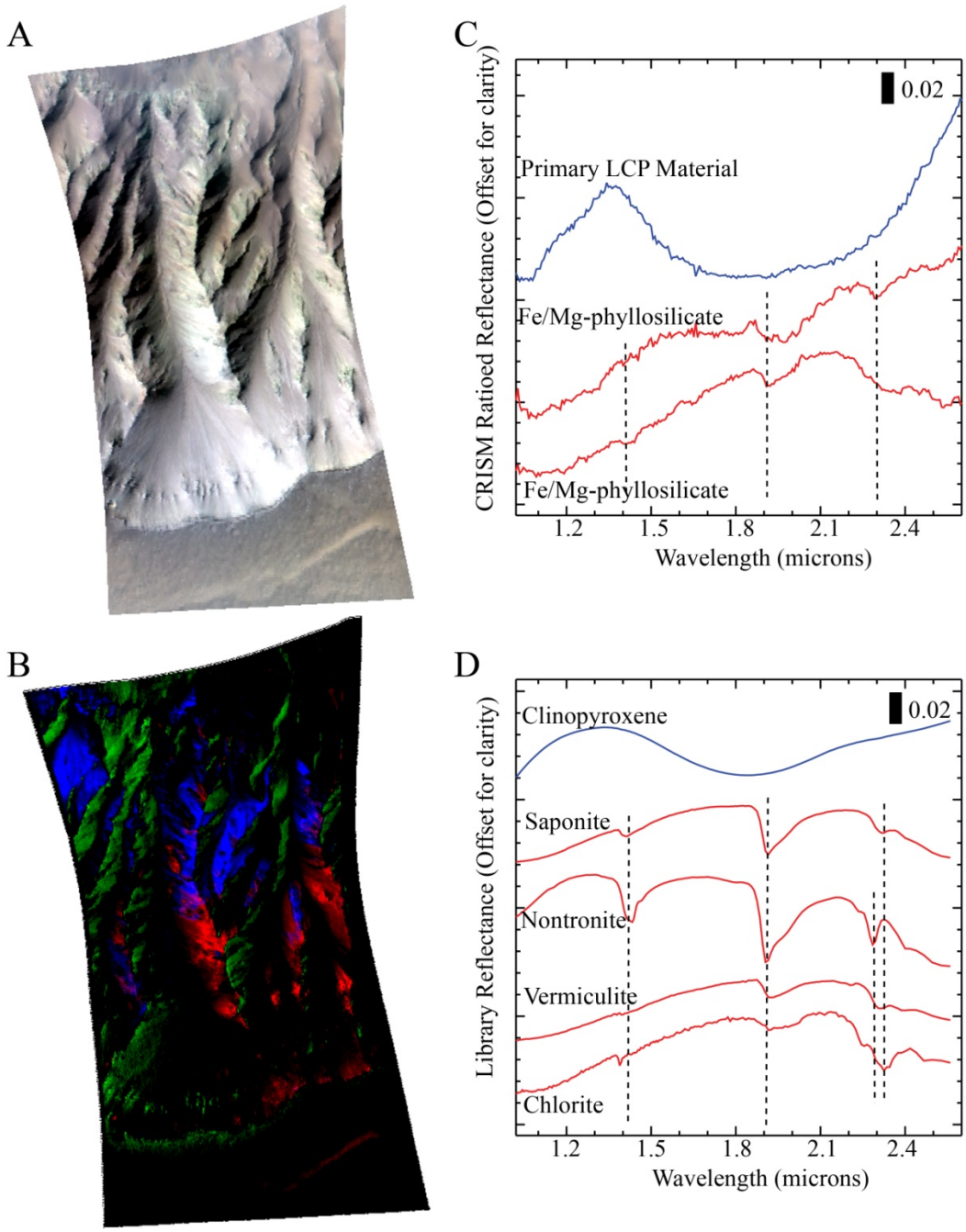

Figure 28. Spectral examples of 2.3 μm Fe/Mg-smectite and LCP primary material. (hrl0000d0de). (A) Standard RGB CRISM image (R: Band 233 (2.5295 μm); G: Band 78 (1.5066 μm); B: Band 13 (1.0800 μm)). (B) Map mineral produced in ENVI from average spectra in user-defined ROIs (R: Fe/Mg-smectite; G: Spectral flat background; B: LCP material). (C) Ratioed CRISM spectra typical in this scene. (D) Library spectra that most closely match CRISM results.

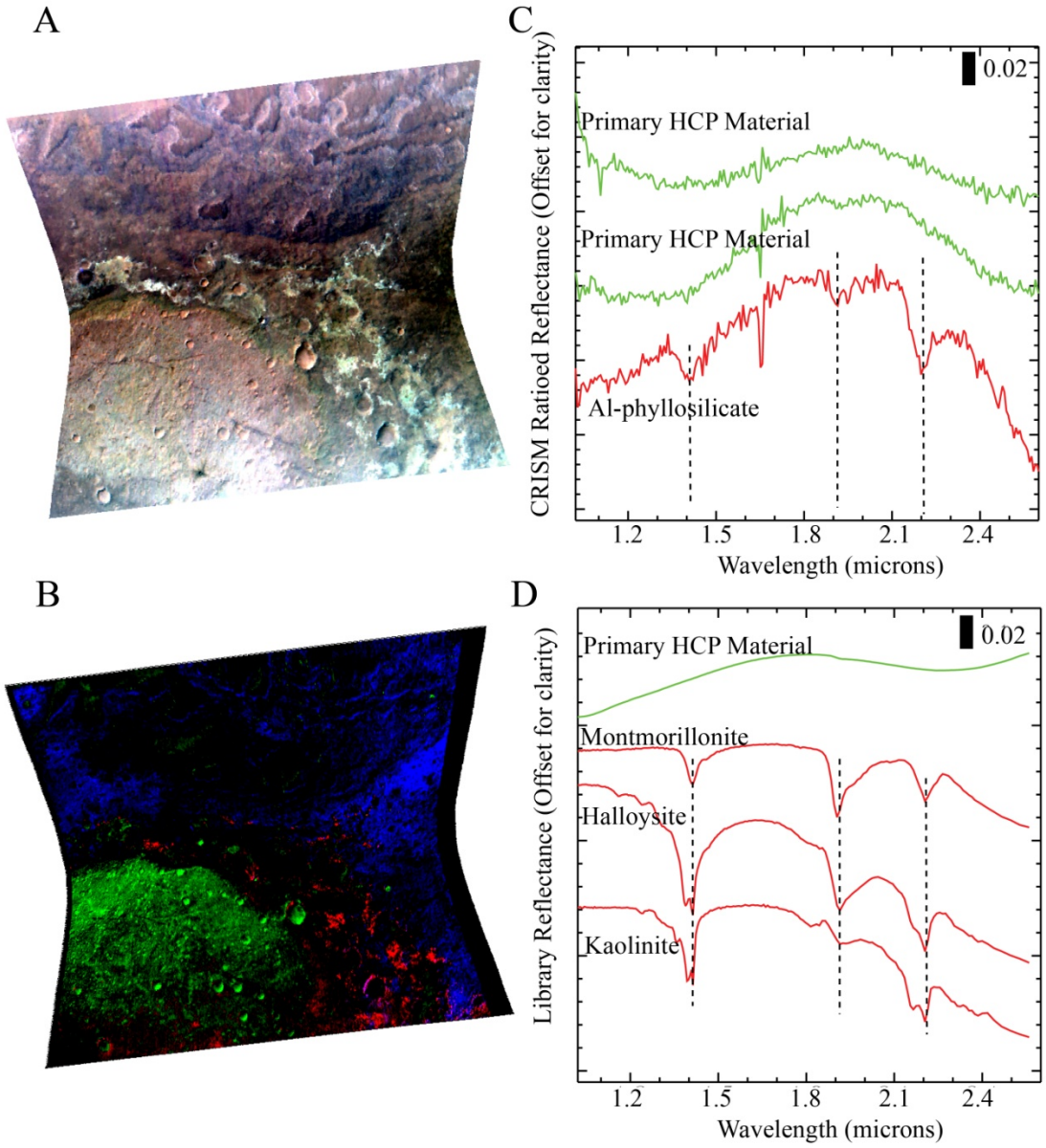

Figure 29. Spectral examples of 2.2 μm Al-phyllosilicates and HCP on the southern plateau. (frt0000a51a). (A) Standard RGB CRISM image (R: Band 233 (2.5295 μm); G: Band 78 (1.5066 μm); B: Band 13 (1.0800 μm)). (B) Map mineral produced in ENVI from average spectra in user-defined ROIs (R: Al-phyllosilicate; G: Higher reflection HCP material; B: Lower reflections HCP material). (C) Ratioed CRISM spectra typical in this scene. (D) Library spectra that most closely match CRISM results.

work in Coprates and surround chasmata [*Edwards et al.*, 2008; *Murchie et al.*, 2009a; *Flahaut et al.*, 2012].

Higher in the stratigraphic sequence the dominant alteration mineral family observed in eastern Coprates Chasma was deep Fe/Mg-smectites (Figure 28). Fe and/or Mg-phyllosilicates were identified from metal-OH bands in the 2.3 μm region. The shape of this band varied from a well-defined singlet band, most similar to saponite, or a dropoff, most like vermiculite. There were also instances of a 2.3 μm band without a strong 1.9 μm hydration band. This could be indicative of a dehydrated smectite or phyllosilicates in the chlorite family that lack the 1.9 μm feature.

The majority of Fe/Mg-smectite minerals occurred generally in the spur and gully formations with an absolute elevation range of about -1.0 to -3.0 km, corresponding to the previously identified deep phyllosilicate layer (Figure 30). One exception to this existed, where a distinct layer, approximately 15 meters thick was evident throughout the scene. Relative elevations were generally consistent between the north and south walls and the central ridge, but slightly higher in the west compared to the east. Clays were approximately 3.0 to 4.5 km below the plateau elevation in the east and 1.0 to 4.5 km in the west, although there was the occasional outlier. The elevation continuity of the deep 2.3 μm phyllosilicate layer between the northern, southern, and ridge slopes was indicative of pre-rifting alteration. These clays could have been emplaced by subsurface hydrothermal circulation or surface alteration followed by burial as has been suggested for other areas in Valles Marineris [*Murchie et al.*, 2009a; *Ehlmann et al.*, 2011a, 2011b]. The longitudinal differences in the absolute elevations of this section may be attributed to the intersection of basement structures of the Coprates Rise exposed in the canyon wall.

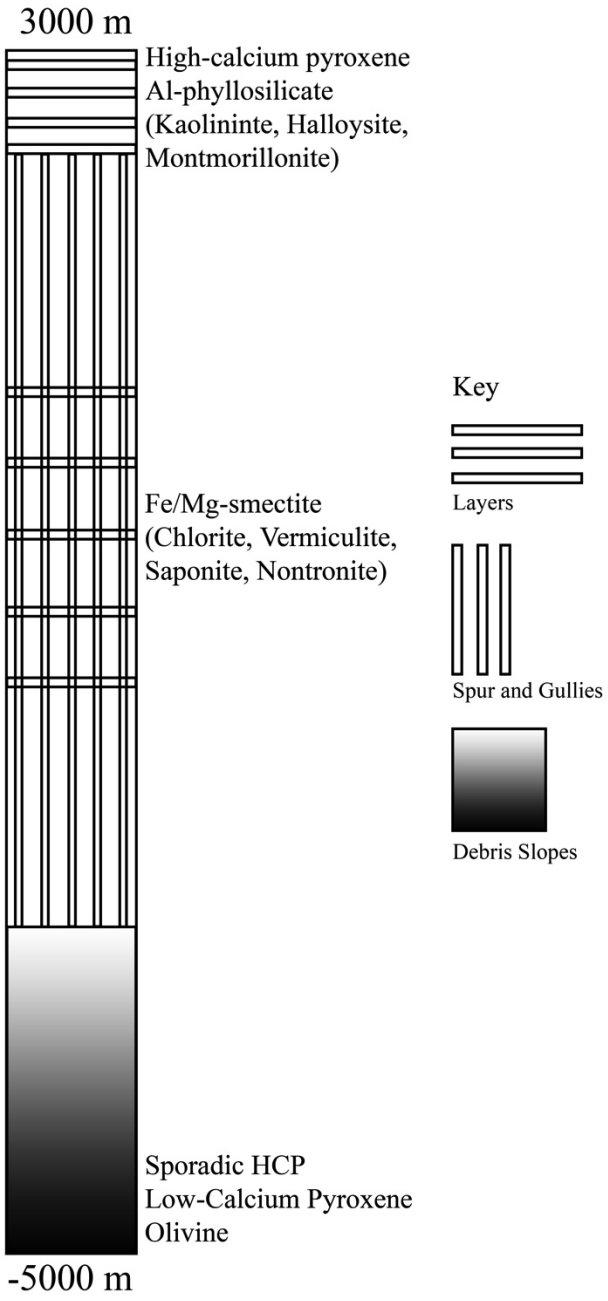

Figure 30. Average stratigraphic column of Coprates Chasma. Additional alteration minerals, sulfates, hydrate silica, and a deep Al-phyllosilicate, were observed sporadically throughout the column. Generally, the absolute elevations in the west are higher than the east due to the intersection of the Coprates Rise.

When first studied, the deep phyllosilicate layer was attributed to chlorite-rich material, due to the comparative depth of the 1.9 μm and 2.3 μm bands [*Murchie et al.*, 2009a]. The results of this study indicate that a wider variety of phyllosilicates may be present at this including more Mg- and more Fe-rich endmembers. These clays can be highly hydrated based on the strength of the 1.9 μm band. Additionally, we identified Fe/Mg-smectites in spurs that were around -4.0 km, lower than previous estimates [*Murchie et al.*, 2009a; *Flahaut et al.*, 2012]. In general, there is a greater vertical extent of Fe/Mg-phyllosilicates in the western portion of the chasma with observation within a few hundred meters of the plateau surface, while no Fe/Mg-phyllosilicates were observed in the upper 2.0 km of the eastern walls. The added input of heat from Coprates Rise in the south-west wall may have driven alteration processes to occur throughout a larger vertical area in the west, as is evident in concentrated hydrated silica deposits at the intersection.

Additional mid-wall pre-rifting alteration was observed as a concentrated hydrated silica deposit (Figure 31). Hydrated silica, such as opal, amorphous silica, or chalcedony, was identified with strong 1.4 μm and 1.9 μm hydration bands plus a broader band centered around 2.25 μm. The silica identified in our study corresponded to an area recently exposed by mass wasting landslides. This balcony area sits approximately 3.5 km lower than the plateau and 3.0 km off the floor. It was also one of the only locations where a distinct 2.3 μm phyllosilicate layer was observed. The hydrated silica was evident in debris flows and appeared to source from a thin wall unit. Hydrated silica is a dominant product in acidic, hydrothermal environments [e.g. *Seelos et al.*, 2010; *Hynek et al.*, 2012]. The location of the deposit was spatially close to the intersection of Coprates Rise that may have resulted in subsurface hydrothermal activity forming the silica. Alternatively this alteration could be from localized hydrothermal activity

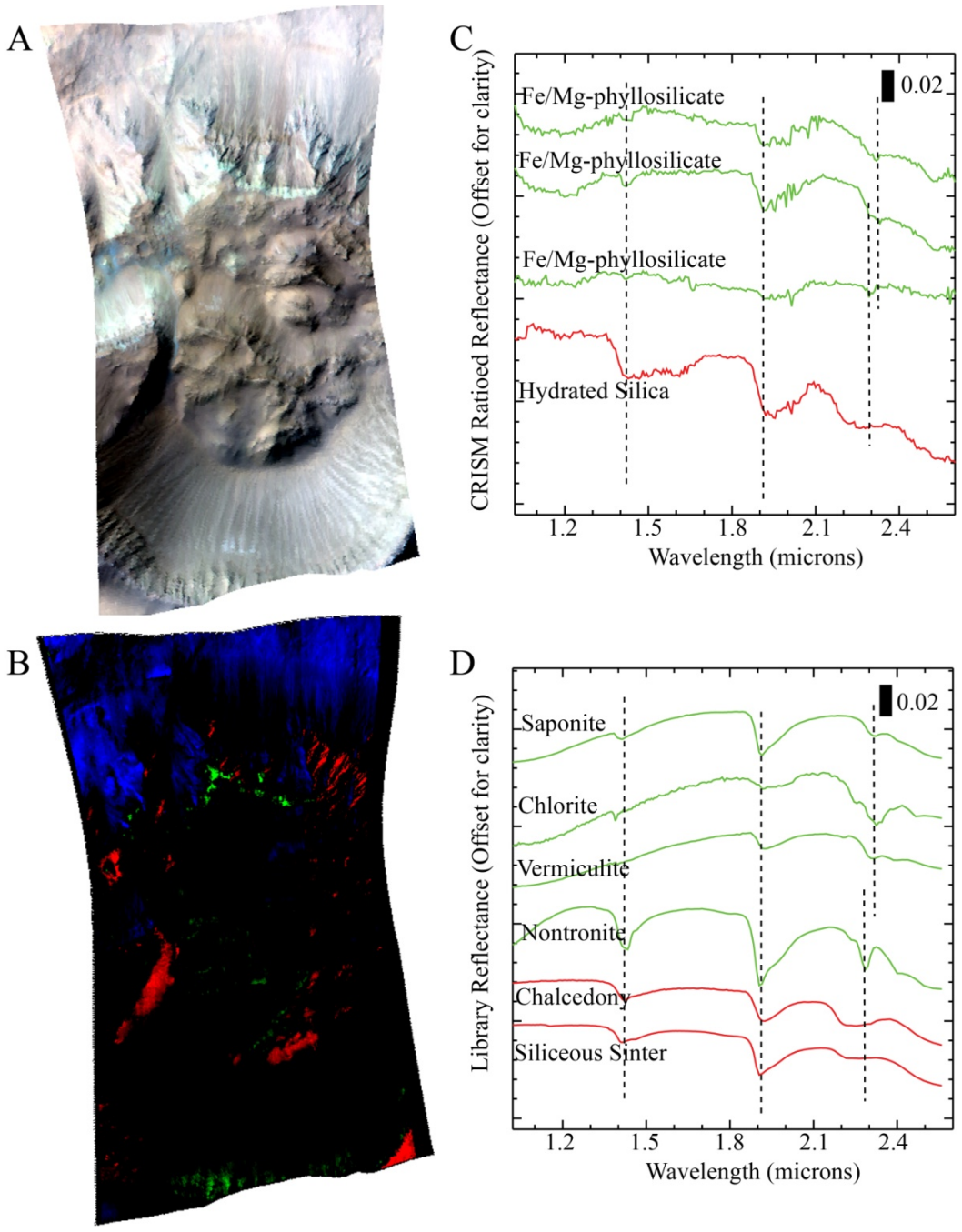

Figure 31. Spectral examples of hydrated silica and types of Fe/Mg-phyllosilicates from a more recently exposed balcony mid-slope on the south west wall (hrl0000a8f6). This is the only place where a distinct phyllosilicate layer was observed in the wall. (A) Standard RGB CRISM image (R: Band 233 (2.5295 μm); G: Band 78 (1.5066 μm); B: Band 13 (1.0800 μm)). (B) Map mineral produced in ENVI from average spectra in user-defined ROIs (R: Silica spectra; G: Fe/Mg-smectite; B: Spectrally flat background material). (C) Ratioed CRISM spectra typical in this scene. (D) Library spectra that most closely match CRISM results.

generated during the rifting event. We favor the former due to the association of volcanism and the deposit.

These phases of Fe/Mg-phyllosilicate were also found in the floor mounds observed. An asymmetrical mound to the west of the central ridge has a peak at an absolute elevation of -3.1 km. Similar to the walls, floor phyllosilicates were observed in the spurs and there is evidence of an HCP-rich layer at the base of the mound. Disordered landslide deposits on the chasma floor had isolated instances of Fe/Mg-phyllosilicates that did not appear to have continuity that would indicate formation at that location; therefore, this signature was likely a result of mixed wall phyllosilicates that were disrupted during the landslide.

At the top of the stratigraphic column was high calcium pyroxene (HCP) identified by a broad peak and dip shifted to longer wavelengths from the LCP (1.72 μm and 2.30 μm, respectively) and Al-phyllosilicates identified by the 2.2 μm band from the Al-OH bond (Figure 29). The plains observations in Coprates Chasma tended to exhibit singlet bands, most like montmorillonite, but we cannot rule out other Al-phyllosilicates. We found evidence of an extensive near-surface layer of Al-phyllosilicates (Figure 30). Specifically it occurred in small ridges as if exposed from the shallow subsurface. This is a new addition to the stratigraphic column presented in *Murchie et al.* [2009a], which had an Al-phyllosilicate then Fe/Mg-phyllosilicate sequence several hundred meters below the surface. CRISM scenes of the surrounding plateau utilized in this study suggested that there is an Al-phyllosilicate layer frequently exposed in the textured terrain throughout the study area.

The shallow-subsurface 2.2 μm Al-phyllosilicate was regionally extensive on the southern plateau, ranging across the entire east-west extent of the study area. The extent of this layer on the northern plateau is unclear, since limited CRISM data did not yield distinctive

spectral results. However, the north and south surfaces had a similar texture and some small ridges in the north had a 2.2 μm band, which could indicate the Al-phyllosilicate was also on the north plateau and formation occurred pre-rift. The widespread nature of this layer and its association with the chasma could suggest formation during high heat flow and rock-water interactions around the time of the rifting. Rifting would increase the heat flow of the area and Al-phyllosilicates are readily produced in hydrothermal conditions [e.g. *Altheide et al.*, 2010 *Hynek et al.,* submitted; *Marcucci et al.,* submitted]. Alternatively, these materials could have formed following the global trend of mineralogy, which forms Fe/Mg-smectites then Al-phyllosilicates and eventually oxidized iron as conditions become more arid [e.g. *Bibring et al.*, 2006]. The horizontal extent of the minerals would be indicative of the formation environment. The alteration appears to be associated with the chasma rim, extending approximately 50 km from the edge. CRISM coverage is not continuous, but images 150 km from the southern rim edge did not have the shallow subsurface Al-phyllosilicate features. This information suggests that the alteration was associated with the rifting event. Alternatively, the may be a more extensive deposit that has a shallower exposure depth near the rim and further from the rim similar alteration would exist at greater depth in the crust.

THEMIS daytime infrared spectroscopy was used to examine the chasma floors and plateau tops. The dominant signature was a standard basalt spectrum, but isolated areas had a dip in the 9 μm area, which is indicative of either a silica-rich or sulfate material (Figure 32). In particular, there was a sinuous red deposit evident in the 8-7-5 DCS image that had a strong absorption near 9 μm that corresponded to the edge of a landslide deposit. Based on the widespread nature of the signal, we attribute these features to a silicate-rich material rather than a sulfate-rich material, given the greater extent of silicate materials.

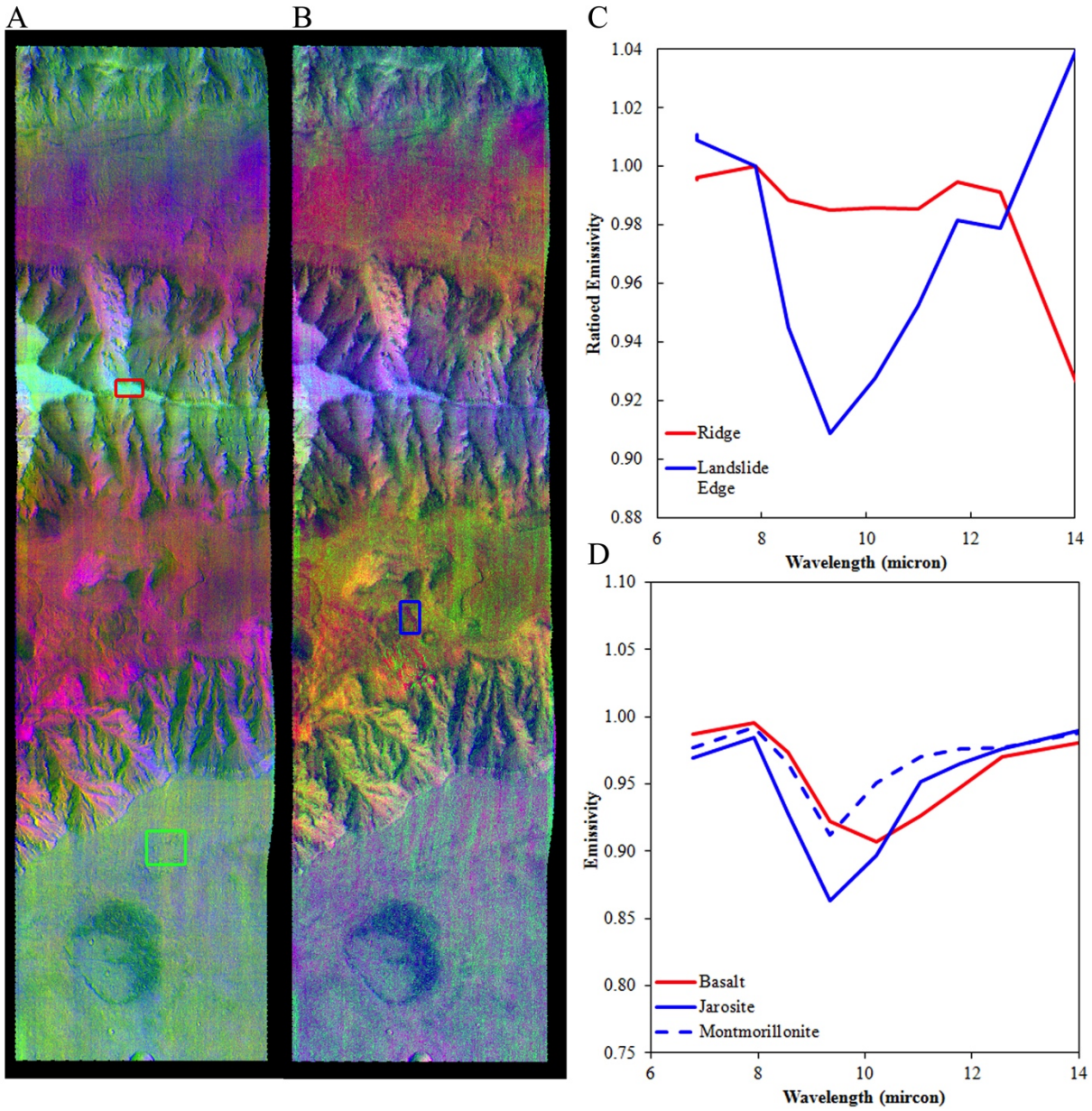

Figure 32. (A) 9, 6, 4, DCS image of radiance THEMIS scene (I4278002) over Coprates Chasma and central ridge. (B) 8-7-5 DCS image (radiance) of the same area. (C) Characteristic THEMIS spectra corresponding to boxes on A and B from emissivity images. The central ridge top (blue) was compared to the landslide edge (red). Both were ratioed over a dusty area (green) to enhance spectral differences. (D) Example library spectra. The low around 9 microns is often indicative of silica- or sulfate-rich material, although a definitive identification is not possible and other minerals within these families may be responsible for the spectral shape.

4.4.2 Post-rifting Alteration Mineralogy

We also identified a series of aqueous alteration minerals that appears to have formed concurrently with or after the chasma rifting during generated hydrothermal activity, similar to environments on Earth [*Tiercelin et al.*, 1993]. The section of Coprates Chasma studied in this work does not contain substantial interior layered deposits, which are common in other parts of Valles Marineris and are often associated with sulfates [e.g. *Roach et al.*, 2010a]. Sulfates generally had a 2.4 μm band and hydration bands. The 1.9 μm hydration band shifts to 2.1 μm for monohydrated sulfates so it can be indicative of a monohydrated versus polyhydrated sulfate. By the nature of the visible near-infrared spectral characteristics of sulfates, they can be hard to conclusively identify in CRISM data. The broad nature of the 1.9-2.1 μm hydration band plus the 2.4 μm band of the Mars spectra in our study area best matched a monohydrated sulfate, such as kieserite or szomolnokite (Figure 33). A well-defined deposit in CRISM at -2.88 km was only slightly discernible in HiRISE images. The other sulfates were observed between -0.17 to -0.67 km and -4.67 to -4.74 km and appeared to occur in unconsolidated deposits.

The variability of deposit morphology, unconsolidated or cohesive, suggested formation from multiple mechanisms post-rifting. A floor deposit formed a large white feature in a slight depression that may be evaporitic. The discrete sulfates on the chasma slopes situated at a range of elevations could represent more concentrated hydrothermal activity. At field sites in Nicaragua, the walls of volcanic craters are highly and extensively altered by diffuse and concentrated fumarolic activity [e.g. *Hynek et al.,* submitted; *Marcucci et al.,* submitted; *McCollom et al.,* submitted]. Coprates Chasma is larger than this terrestrial example, but conclusions can be drawn about hydrothermal wall alteration. The isolated sulfate deposits on Mars may be due to the larger size that resulted in spatially sporadic hydrothermal activity or

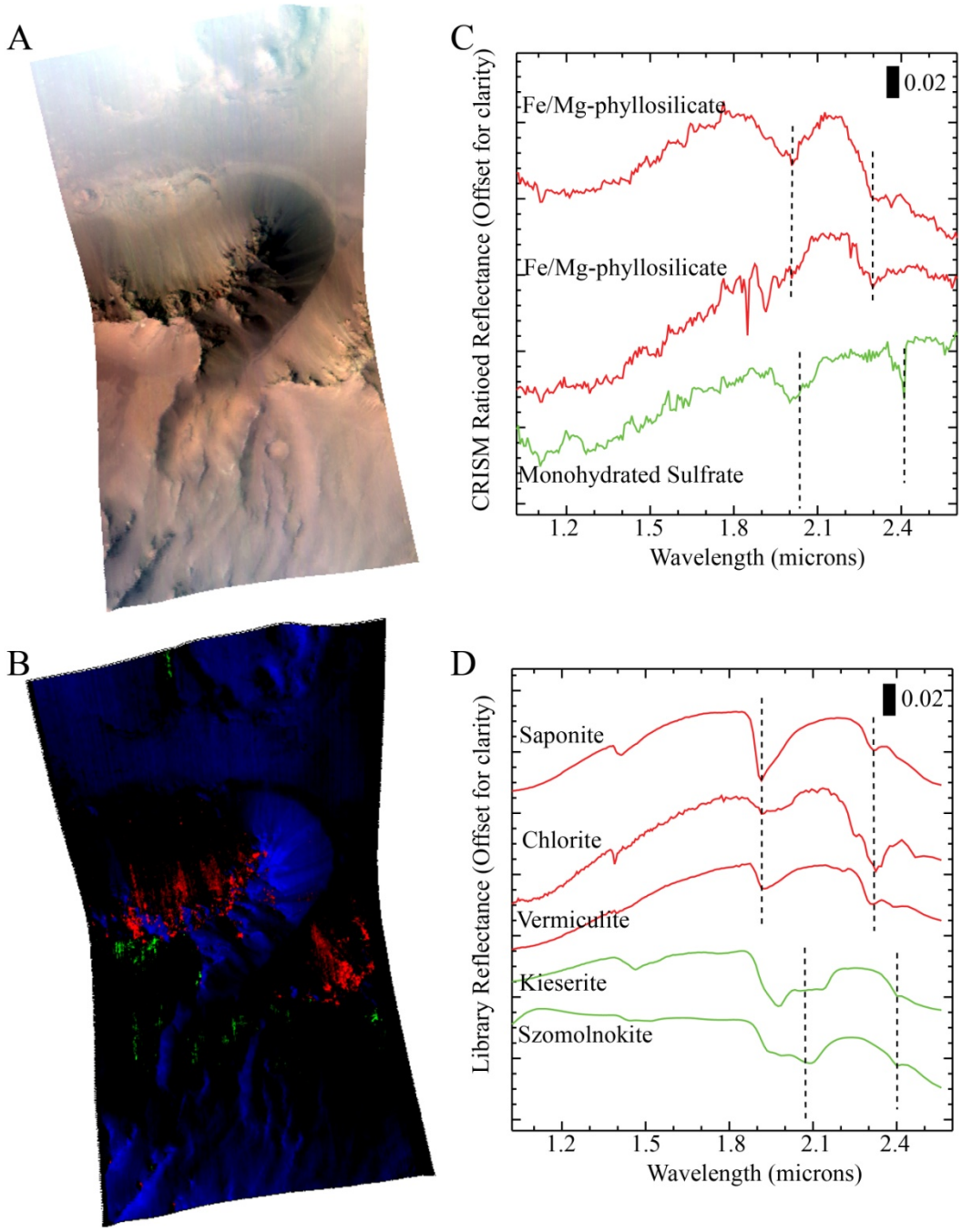

Figure 33. Spectral examples of a likely monohydrated sulfates and eroding Fe/Mg-phyllosilicates (hrl00012316). (A) Standard RGB CRISM image (R: Band 233 (2.5295 μm); G: Band 78 (1.5066 μm); B: Band 13 (1.0800 μm)). (B) Map mineral produced in ENVI from average spectra in user-defined ROIs (R: Fe/Mg-smectite; G: Sulfate B: Spectrally flat background material). (C) Ratioed CRISM spectra typical in this scene. (D) Library spectra that most closely match CRISM results.

post formation alteration processes, such as erosion that obscure the original extent of the deposits. We favor isolated events, similar to isolated systems that could have formed the interior layered deposits seen in other Valles Marineris chasmata.

Additionally, two isolated instances of the 2.2 μm phyllosilicate clay occurred at elevations lower than -4.0 km elevations. In both cases, these were coherent bright deposits, either forming small knobs or a thin layer in the lower wall. The coherent and isolated nature of these deposits suggested a post-rifting formation mechanism, such as localized hydrothermal activity. Al-phyllosilicates, over Fe/Mg-phyllosilicates, preferentially form in volcanic hydrothermal environments [*Altheide et al.*, 2010 *Hynek et al.,* submitted; *Marcucci et al.,* submitted].

South of the main Coprates Chasma area is a series of shallower grabens that experienced alteration distinct from that in the main chasma. The walls in these scenes had some layers, like those of the main chasma, with spectra exhibiting 2.2 μm, 2.3 μm, and 2.4 μm bands and hydration features. These minerals could be Al-phyllosilicates mixed with sulfates, likely polyhydrated based on distinct 1.9 μm band. The dominant features were large white deposits on the basin floors that contained concentrated white deposits, which had a mixture of mineral signatures including Fe/Mg-smectites, Al-phyllosilicates, and sulfates. The sulfates within this mixture had a defined 1.9 μm hydration band suggesting polyhydrated sulfates, although phyllosilicate signatures were more prominent and could account for this singlet hydration band. The basins were areas where water could have collected and evaporated to form a mixture of phyllosilicates and sulfates. The spatial relationship of the grabens with the Coprates Rise volcanism could be analogous to outwash basins in terrestrial volcanic environments [e.g., *Hynek*

et al., submitted; *Marcucci et al.,* submitted]. In these environments hydrothermal alteration occurs in the walls and subsequent precipitation concentrates sulfates in the topographic lows.

4.5 Summary

The purpose of this study was to determine the minerals present and their variability, the types of alteration, and how alteration related to the rifting events. We have identified Al- and Fe/Mg-phyllosilicates, sulfates, and hydrated silica in our study area of Coprates Chasma (Table 7). Our mineralogical and stratigraphic analyses of Coprates Chasma suggest that this area experienced alteration pre- and post-rifting and nearby smaller grabens exhibit additional alteration. This area is also influence by the pre-rifting emplacement of the Coprates Rise. We propose the following sequence of events:

(1) emplacement of LCP and olivine-rich material (deepest representing the Noachian),

(2) subsurface hydrothermal alteration formed deep phyllosilicates, mainly Fe/Mg-smectites,

(3) emplacement of Coprates Rise that caused uplift that offset the absolute elevations of the eastern and western stratigraphies and may have resulted in increased hydrothermal activity to the west forming subsurface hydrated silica deposits,

(4) start of rifting event that caused localized hydrothermal activity forming Al-phyllosilicates in the shallow subsurface associated with the rift center,

(5) rift opens forming a wide chasma with a central ridge and drop block floor mounds similar to the present day configuration,

(6) isolated hydrothermal areas form deep Al-phyllosilicates and monohydrated sulfates deposits,

(7) simultaneous or subsequent rifting forms small, shallower grabens south of the main chasma,

(8) fluid infill and evaporation in southern basins result in mixed evaporatic deposits including Fe/Mg-phyllosilicates, Al-phyllosilicates, and polyhydrated sulfates,

(9) landslides in the south wall near Coprates Rise expose the subsurface hydrated silica.

Coprates Chasma is a study in ancient alteration processes on Mars. The deep view of crust exposes unique information about the ancient crust of Mars. While deep olivine and LCP-bearing materials have been observed in other chasma, deep phyllosilicates have fewer exposures and are often excavated through impacts. Their identification *in situ* within the stratigraphic columns demonstrates their association with other minerals and timing of emplacement. Similarly, very shallow Al-phyllosilicates are unique to this area and suggest near surface hydrothermalism associated with the chasma rifting. Rifting has also caused hydrothermal alteration that formed isolated sulfate deposits. Sulfates are not prevalent in this portion of Valles Marineris as compared to other chasma, and these deposits do not form interior layered deposits. This may suggest a different formation mechanism. The association of Coprates Chasma with the large outflow channels may also affect the preservation of soluble mineral deposits. Coherent hydrated silica deposits exposed by landslides are in contrast to those associated with volcanic vents, impacts, or plains materials. They may demonstrate a complex relationship of subsurface hydrothermal activity associated with nearby volcanic interactions. Coprates Chasma is a unique area that represents a range of alteration types, ancient alteration, and an area largely free of interior deposits that provide a relatively clear view of wall structure and mineralogy.

5. Discussion and Conclusions

Sustained water activity is clearly evident on Mars, as is geothermal heat flow obvious from the number of volcanic centers across the planet. Understanding the interaction of magma and water on Mars is important for interpreting the geological evolution and astrobiological potential of the planet. Sulfates on Mars were first detected by the *Viking 1* and *2* landers in the 1970s and their widespread presence has been detailed through present-day instrumentation on the surface and in orbit. Sulfates are soluble, hydrated minerals often indicative of aqueous alteration. This work represents a study of the reaction pathways of acid-sulfate weathering using a combination of laboratory experiments, geochemical models, terrestrial analogs, and Mars remote sensing data. Acid-sulfate weathering is a process that can occur in many environments that have different implication for planetary history and habitability. For example, this type of weathering can occur in acid mine drainage areas, briny evaporitic lakes, dirty ice, impact-induced hydrothermalism, and regional acid fog. In this dissertation, I presented work that focuses on alteration that occurs in volcanic, hydrothermal environments. These systems are characterized by low pH, high temperatures, high sulfur concentration, and generally low fluid:rock ratio fumaroles (although some volcanic centers can host hotspring with high fluid:rock ratios). There are three parts of this project that build on each other.

My first contribution to the understanding of acid-sulfate weathering focused on visible near-infrared (VNIR) reflectance spectroscopy fieldwork at Nicaragua locales. This was novel *in situ* fieldwork at these sites. Measurements and samples were collected from four sites, Cerro Negro, Momotombo, Telica, and the Hervidores de San Jacinto (Mudpots). These four sites are the result of convergent tectonics as the Cocos Plate subducts under the Caribbean Plate off the west coast of Central America. The volcanoes range in age from 150 years to several centuries

and are characterized by basaltic to basaltic-andesitic primary materials. There are small differences in the rock and gas chemistry that may explain some secondary mineralogy differences. All four areas are currently active and have concentrated and diffuse fumarole vents with temperatures ranging from ambient to several hundred degrees and pH from -1 to 5. The Nicaraguan field sites are ideal Martian analogs because the unaltered rock chemistry closely matches that of Martian bedrock. This material influences fluid composition through weathering which ultimately affects the secondary minerals precipitated. The steam-driven fumaroles that represent low fluid:rock ratio systems were also of interest. Experiments and models in the proceeding section were designed after these environments.

Previous field campaigns collected samples for analysis upon return to home laboratories. While these trips were very productive, there was a desire to examine mineralogy *in situ* in order to understand the spatial context and relationships of their formation, measure thin surface coatings, and avoid mineral phase changes that occur when minerals are moved from their original locations. The August 2012 campaign was the first time *in situ* VNIR spectroscopy and x-ray diffraction were used in the field, and these instruments are similar to those on Martian orbiters and rovers. The combined analysis using both instruments also allowed for a comparison of the two techniques. The rapid collection of spectra resulted in over 200 samples. Trends within the minerals identified in these spectra suggested environmental constraints. At the Nicaraguan sites, amorphous silica, sulfates, sulfur, oxides/hydroxides, and phyllosilicates were present, in decreasing order of abundance. The predominant control of secondary mineralogy was the rock and gas composition, followed by environmental factors, such as temperature, pH, and fluid:rock. This is consistent with the experimental and model results where the alteration mineralogy was the same for a given starting material, regardless of other

initial parameters variations. Amorphous silica and elemental sulfur dominated the most acidic and highest temperature fumaroles. Sulfates, such as gypsum and natroalunite, occurred at fumaroles with more moderately acidic pHs and temperatures. Additionally using the VNIR instrument, abundant Mg-sulfates, and other highly soluble minerals were detected in an outwash basin where precipitation runoff ponded before evaporation. This is consistent with the experimental and model results in the first part of this research that demonstrated large amounts of Mg- and Fe-sulfates formed during the evaporation stage of alteration. This work implies that on Mars deposits of dominantly Mg- and Fe-sulfates may have been locally concentrated by precipitation and surface water flow. Concentrations should occur in topographic lows. Alternatively, areas where these sulfates are intimately mixed with other minerals are locations that likely have not experienced rainfall or surface water processes.

One of the novel insights into mineralogy at these sites was the presence of phyllosilicates. Phyllosilicates were present at all sites, but were much more frequent at the higher fluid:rock ratio site, San Jacinto Mudpots. Previous campaigns had not observed abundant or widespread phyllosilicates. Additionally, phyllosilicates were missing from the experiments, although models predicted their formation. The lack of phyllosilicates in experiments is likely due to a kinetic inhibition, which is overcome in the field with long maturation times and the presence of materials that can nucleate formation. Al-phyllosilicates (kaolinite and montmorillonite) were the main phases found in the field (potentially the Al-Si-rich amorphous gels in experiments could represent an immature form of the field phyllosilicate); however, evidence of Fe/Mg-smectites were also present. These latter phases are not as stable in high temperatures and low pHs as Al-phyllosilicates and their presence on Mars is often used to denote more clement conditions with neutral to alkaline pH. While large

deposits of Fe/Mg-smectites on Mars have likely not experienced hydrothermal conditions, their presence at the Nicaragua volcanoes indicates that they can form in acidic hydrothermal systems. Even though phyllosilicates in Nicaragua form in acidic environments, the areas with higher fluid:rock ratio and more maturity promoted greater formation. Observations of phyllosilicates mixed with sulfates, iron oxides/hydroxides, and amorphous silica may suggest a volcanic environment on Mars. In particular, phyllosilicate deposits in volcanic hydrothermal deposits would likely be composed mainly of Al-clays with sometimes minor Fe/Mg-clays.

Because the field portable VNIR instrument is similar to ones that orbit Mars, direct comparisons between Martian observations and these field results were possible. For example, Noctis Labyrinthus and northern Merdiani Planum have sequences of Fe/Mg-smectites over Al-phyllosilicates, which is an inversion of the normal global sequence. Localized aqueous environments different from the global trend could account for these. Such environments may have included a late influx of more neutral water due to topography concentrating valley network or flood fluid or impact release of volatiles. However, the Nicaraguan volcano fieldwork showed that these minerals could form and exist within a single hydrothermal environment. In Terra Sirenum on Mars, muted spectral features in an alunite spectrum originally suggested a low temperature formation; however, in Nicaragua similar features resulted when the alunite deposit was mixed with iron minerals, so that the combined spectrum had suppressed features of the individual minerals.

In Valles Marineris, the rifting event may have resulted in extensive hydrothermal activity that could explain the similarities in its sulfate deposits to the field sites. Finally, amorphous silica has been observed at Gusev crater and Syrtis Major, and it was also a major alteration mineral in Nicaragua. At Gusev crater there is a soil class called ‘Paso Robles’ that

sparked a debate over whether the silica was hotspring or fumarole-derived. The association of amorphous silica and sulfates observed at Gusev crater is similar to the mineral groups in the Nicaraguan field site with one difference being the type of sulfate, which was explained with basalt and gas chemistry variations. Amorphous silica was sufficiently widespread in Nicaragua and from orbit with Mars-equivalent spectrometers; it may be the dominant mineral signature as it is at Syrtis Major. The association of silica with sulfate, iron oxides, and phyllosilicates at the field sites, suggests that if higher resolution data were obtainable at Syrtis Major these other minerals would also be detected. This fieldwork represents the first time Nicaraguan field mineralogy was examined *in situ* and could be compared to Mars VNIR observations. In general, the field data have a much higher spectral resolution than Mars data resulting is greater confidence in mineral identification. With detailed field minerals, spatial associations, and environmental constraints, stronger inferences could be made about the Mars observations, such as paleoconditions and predictions of other minerals present. Additionally, there are currently limited remote sensing data over the Nicaraguan volcanoes. It would be very beneficial to conduct a regional CRISM-resolution remote-sensing campaign of this area. Such a study would strengthen the understanding of how *in situ* mineral observations compare to how minerals are viewed remotely. This comparison would then allow for more accurate predictions of Martian surface material from the orbiter data. I expect that CRISM-scale data over the Nicaraguan volcanoes would reveal spectral signatures dominated by hydrated silica and sulfates. Sporadic instances of phyllosilicates are also expected, particular over more mature areas such as San Jacinto. Iron oxides are slightly less distinctive than phyllosilicates in CRISM-type spectra, but should be discernible in areas that have been oxidizing from exposure to the atmosphere for longer periods of time. Additional, the Nicaraguan sites are modern Earth environments that are

being compared to ancient Martian locations. With an additional ~3 billion year old of surface weathering after the hydrothermal volcanic systems stopped, I expect phyllosilicate and iron oxide/hydroxide minerals to become progressively more abundant because of longer maturation times and more oxidation. A short summary of highlights from this work includes:

- Mg-sulfates are found in outwash basins indicating an evaporitic formation
- Fe/Mg-smectites can form in acidic, hydrothermal conditions
- Small-scale changes in environmental inputs result in the co-formation of sulfates, iron oxides/hydroxides, and phyllosilicates
- Field VNIR compared directly to Mars observations suggests alunite in Terra Sirenum could have a high temperature formation, supports concentrated silica in Gusev crater that form in volcanic environments, predicts that sites dominated by silica from orbit, such as Syrtis Major, would also have abundant sulfate and some iron oxides/hydroxides and phyllosilicates

The second component of my research was a series of aqueous geochemical experiments and models. The experiments and models were designed to detail the alteration in the Cerro Negro (CN), Nicaragua, field site to better understand the reaction pathways by determining what chemical and initial parameters constrained secondary mineralogy. To this end, I determined the mineralogical composition of CN whole rock basalt through a literature search. For experiments, these minerals were obtained from a commercial supplier and in models they were represented by oxides for accurate composition. Primary minerals were reacted with 1 molal H_2SO_4 (sulfuric acid) at varying fluid:rock ratios (1:1, 4:1, 10:1) and temperatures (65, 150, 200ºC). Experiments also introduced a time factor (ranging from 1 day to 7.5 months). This work encompassed parameter space relevant to Martian acid-sulfate weathering that had not

previously been explored. Previous experiments by other researchers generally included lower temperatures, fluid mixtures with additional acids (not pure sulfuric acid), and did not separate alteration and evaporation processes. Similarly, thermodynamic models used a temperature of 0ºC. This study was unique from previous ones due to the use of high temperatures, separation of alteration and evaporation products, and simultaneous use of experiments and models to examine the reaction pathways.

There were three main results from these CN mineralogy experiments and models. First, I determined that primary mineral composition was the dominant factor responsible for the formation of resultant mineral assemblages. For a given mineral, variations in initial parameters resulted in change of size, shape, and abundance in the secondary products, but not the type. This implied that a determination of formation environment would not be possible with only mineral identification from orbiters or landers. Instead microscopic imagery, more powerful than the current rovers, of alteration deposits is needed to examine fine-scale textures, which these experiments suggested to be distinguishing characteristics. Additionally, regional context and morphology are critical. Second, results demonstrated that a distinction between evaporation and alteration products is crucial to understanding reaction pathways. Sulfate minerals in prior studies and on Mars have been attributed solely to evaporation processes; however, this study identified abundant sulfates in acidic conditions even when high fluid:rock ratios existed. Simultaneous completion of experiments and models helped highlight this discrepancy of expected versus actual secondary minerals. Third, the bulk of previous thermodynamic modeling was completed at much lower temperatures, which affects the relative kinetic rates of dissolution. These experiments showed that pyroxene weathered more slowly than plagioclase and olivine at high temperatures, contrary to low temperature results where plagioclase weathers

more slowly than pyroxene and olivine. This information was used to interpret whole rock weathering experiments, where plagioclase and olivine dissolved most quickly, releasing cations leading to the formation of natroalunite, iron oxides, and amorphous silica. Subsequent dissolution of pyroxene was responsible for the formation of anhydrite. During fluid evaporation, abundant Mg-sulfates, gypsum, and some Fe-sulfates formed. The presence of these minerals at field sites and on Mars gives insights into the amount and degree of water activity post-formation. For example, precipitation can concentrate soluble sulfates in outwash basins as seen at Cerro Negro. On Mars, areas with a high abundance of these sulfates may not have experience reworking by water after the sulfates were deposited or it did experience water reworking and the original deposits were larger. A short summary of highlights from this work includes:

- Secondary mineralogy is controlled by starting material and initial parameters affect microscopic features, such as abundance, size, and duration
- Plagioclase and olivine react more quickly than pyroxene at high temperatures
- Ca-sulfate and natroalunite are examples of sulfates that formed during alteration and sulfates were not restricted to formation during evaporation
- Simultaneous completion of experiments and models produced new insights into reaction pathways
- Mg-sulfates were found exclusively in evaporation experiments

The final portion of this dissertation was to apply the knowledge gained from the previous work to a location on Mars, Coprates Chasma within the Valles Marineris rift valley. Rift valleys are high-energy areas where ‘thin’ crust allows for shallower magma reservoir. The added heat flow can interact with crustal water creating extensive hydrothermal activity. This is

evident on the Earth in the East African Rift Valley. The Coprates Chasma within Valles Marineris was chosen because it is a particularly deep chasma that exposes ancient Noachian crust and deep phyllosilicates. Additionally, it is largely devoid of layered deposits formed after the rifting event that obscure ground and wall features. For this project, remote sensing VNIR data from CRISM and thermal infrared data from THEMIS were used to examine the mineralogy present within the canyon and determine if spatial trends existed. This work incrementally adds to the body of material on Coprates Chasma from studies farther west of this site that focused on morphological trends. The determination of environmental controls and association of mineral families from previous portions of this dissertation set a framework within which the alteration mineralogy in this chasma can assist in the interpretation of paleoenvironments.

The main alteration mineralogy on the chasma walls was consistent with an Fe/Mg-phyllosilicate, such as saponite, chlorite, vermiculite, or nontronite. These represent a deep phyllosilicate layer possibly indicative of subsurface hydrothermal alteration. The correlation of the elevation of these deposits between the north wall, south wall, and central ridge demonstrated that the alteration occurred pre-rifting. Similarly, irregular floor mounds had similar textures and mineralogies, which suggested they were related to the chasma walls, rather than a post-rifting deposit. An Al-phyllosilicate layer was observed just below the plateaus around the rift system. This layer appears to be on both the north and south sides indicating it is a pre-rifting formation, possibly related to the global climate trend to more acidic environments.

Other mineral deposits at Coprates Chasma were indicative of formation after the rifting event. These consisted of hydrated silica, sulfate, and Al-phyllosilicates. In the field, these minerals were found in highly altered mineral deposits in hydrothermal volcanic environments. Based on the fieldwork and experiments/models from the preceding chapters, these are all

minerals that can be highly indicative of acid sulfate weathering. Silica and sulfate formed in the higher temperature, low pH, steam environments, while Al-phyllosilicates formed in slightly cooler, less acidic, higher fluid:rock ratio areas. Despite the slightly different formation conditions implied by the two groups of minerals, they all occurred at the same field sites, indicating a range of environments within the same hydrothermal volcanic center was possible. Additionally, Coprates Chasma intersects with a volcanic range, which corresponds to the location of the hydrated silica deposits. Added heat flux from the volcanic range may have created an area of increased hydrothermal activity, which ultimately formed the hydrated silica deposits. There is also a series of grabens south of the main chasma that has large white expanses of mineral deposits with Fe/Mg- and Al-phyllosilicate signatures, as well as, sulfates. These deposits appear to form in topographic lows. While the spatial scale is larger on Mars, there could be analogous to the outwash basins of Nicaragua with soluble sulfates and phyllosilicates. Phyllosilicates are more dominant than sulfates in these small grabens, contrary to Nicaragua, but this may be due to formation time. A short summary of highlights from this work includes:

- Eastern Coprates Chasma contains deep pre-rifting alteration and irregular post-rifting alteration
- Heat input from Coprates Rise may have increased the abundance of hydrated silica in the chasma walls
- Small southern grabens experienced a different type of alteration, namely evaporation of basin ponds, than the main chasma

The work presented in this dissertation is aimed at understanding the geological evolution of the planet through identifying the formation conditions of mineral deposits. It was completed

with a wide range of techniques, including laboratory experiments, thermodynamic modeling, field and remote sensing visible near-infrared reflectance spectroscopy and Martian dataset analysis. In brief, it showed that acid-sulfate weathering in a volcanic hydrothermal environment produces amorphous silica, sulfates, iron oxides/hydroxides, and phyllosilicates (in decreasing order of abundance) with abundant amorphous silica at all sites and high sulfur in isolated areas. One of the main goals of this research was to determine if and what diagnostic features existed in secondary mineral assemblages that could be used to distinguish it from other acid-sulfate weathering environments. The results of this work compared to those of other scientists working with these other environments show that there are not obvious definitive differences in the deposit characteristics. However, some controls have been identified. Primary lithology and gas chemistry are the main controls on alteration, followed by environmental parameters, such as temperature, pH, and fluid:rock ratio. Experiments indicated that these environmental parameters often produce only microscopic changes in secondary minerals when the starting material is similar. This indicates that future missions would be able to better interpret deposits with an instrument capable of such microscopic detail. Additionally, the combined use of experiments and models aids in the accurate interpretation of a complete reaction pathway, and *in situ* field techniques show novel mineral diversity within volcanic sites used as Martian analogs, which can be directly related to Martian datasets. The comparison of these datasets allowed for a stronger interpretation of Mars paleoconditions. The spectra from fieldwork lead to modifications of interpretations of some areas on Mars. Through this research I have determined the importance of distinguishing between alteration and evaporation products, the need for a combination of geomorphological context and mineralogical identification in both *in situ* and remote sensing methods.

The volcanic environments presented in this dissertation are dynamic areas with all of the requirements for life: water, energy, and chemistry, and could be abodes for life on Mars, as they are on Earth. Studying acid-sulfate weathering advances the knowledge of planetary surface conditions by recognizing distinguishing features representing conditions of formation. This in turn constrains how the planet evolved, how that evolution relates to Earth, and generally how habitable Mars might have been in the past.

References

Abramov, O., and D. A. Kring (2005), Impact-induced hydrothermal activity on early Mars, *J. Geophys. Res. Planets*, *110*(E12), doi:10.1029/2005JE002453.

Di Achille, G., G.-G. Ori, B. Hynek, and E. Hauber (2008), Global Distribution Of Putative Martian Deltas In The Light Of HRSC And HIRISE Instruments: Open Issues And Hydrological Inferences, in *Second Workshop on Mars Valley Networks*, edited by R. Craddock, pp. 16–19, Smithsonian Institution, Moab, UT (USA).

Di Achille, G., B. M. Hynek, and M. L. Searls (2009), Positive identification of lake strandlines in Shalbatana Vallis, Mars, *Geophys. Res. Lett.*, *36*(14), doi:10.1029/2009GL038854.

Allen, C. C., and D. Z. Oehler (2008), A Case for Ancient Springs in Arabia Terra, Mars, *Astrobiology*, *8*(6), 1093–1112, doi:10.1089/ast.2008.0239.

Altheide, T. S., V. F. Chevrier, and E. Noe Dobrea (2010), Mineralogical characterization of acid weathered phyllosilicates with implications for secondary martian deposits, *Geochim. Cosmochim. Acta*, *74*(21), 6232–6248, doi:10.1016/j.gca.2010.08.005.

Amram, K., and J. Ganor (2005), The combined effect of pH and temperature on smectite dissolution rate under acidic conditions, *Geochim. Cosmochim. Acta*, *69*(10), 2535–2546, doi:10.1016/j.gca.2004.10.001.

Anderson, R. B., and J. F. Bell (2008), Stratigraphy of Phyllosilicates and Sulfates in Northern Meridiani Planum, Mars, *Agu Fall Meet. Abstr.*, 1393.

Arvidson, R. E., J. L. Gooding, and H. J. Moore (1989), The Martian surface as imaged, sampled, and analyzed by the Viking landers, *Rev. Geophys.*, *27*(1), 39–60, doi:10.1029/RG027i001p00039.

Arvidson, R. E., F. P. Seelos, K. S. Deal, W. C. Koeppen, N. O. Snider, J. M. Kieniewicz, B. M. Hynek, M. T. Mellon, and J. B. Garvin (2003), Mantled and exhumed terrains in Terra Meridiani, Mars, *J. Geophys. Res. Planets*, *108*(E12), doi:10.1029/2002JE001982.

Arvidson, R. E. et al. (2006), Overview of the Spirit Mars Exploration Rover Mission to Gusev Crater: Landing site to Backstay Rock in the Columbia Hills, *J. Geophys. Res.*, *111*(E2), E02S01, doi:10.1029/2005JE002499.

Arvidson, R. E. et al. (2009), Results from the Mars Phoenix Lander Robotic Arm experiment, *J. Geophys. Res. Planets*, *114*(E1), doi:10.1029/2009JE003408.

Arvidson, R. E. et al. (2010), Spirit Mars Rover Mission: Overview and selected results from the northern Home Plate Winter Haven to the side of Scamander crater, *J. Geophys. Res.*, *115*, 19 PP., doi:201010.1029/2010JE003633.

Baker, V. R. (2001), Water and the martian landscape, *Nature*, *412*(6843), 228–236, doi:10.1038/35084172.

Baker, V. R., and D. J. Milton (1974), Erosion by catastrophic floods on Mars and Earth, *Icarus*, *23*(1), 27–41, doi:10.1016/0019-1035(74)90101-8.

Baldridge, A. M., S. J. Hook, J. K. Crowley, G. M. Marion, J. S. Kargel, J. L. Michalski, B. J. Thomson, C. R. de Souza Filho, N. T. Bridges, and A. J. Brown (2009), Contemporaneous deposition of phyllosilicates and sulfates: Using Australian acidic saline lake deposits to describe geochemical variability on Mars, *Geophys. Res. Lett.*, *36*(19), doi:10.1029/2009GL040069.

Baldridge, A. M., M. D. Lane, and C. S. Edwards (2012), Searching at the right time of day: Evidence for aqueous minerals in Columbus Crater with TES and THEMIS data., *J. Geophys. Res.*, doi:10.1029/2012JE004225.

Bandfield, J. L. (2008), High-silica deposits of an aqueous origin in western Hellas Basin, Mars, *Geophys. Res. Lett.*, *35*(12), doi:10.1029/2008GL033807.

Bandfield, J. L., D. Rogers, M. D. Smith, and P. R. Christensen (2004), Atmospheric correction and surface spectral unit mapping using Thermal Emission Imaging System data, *J. Geophys. Res. Planets*, *109*(E10), doi:10.1029/2004JE002289.

Banin, A., F. X. Han, I. Kan, and A. Cicelsky (1997), Acidic volatiles and the Mars Soil, *J. Geophys. Res.*, *102*(E6), 356.

Baptista, A. R., N. Mangold, V. Ansan, D. Baratoux, P. Lognonné, E. I. Alves, D. A. Williams, J. E. Bleacher, P. Masson, and G. Neukum (2008), A swarm of small shield volcanoes on Syria Planum, Mars, *J. Geophys. Res. Planets*, *113*(E9), doi:10.1029/2007JE002945.

Bell, J. F. et al. (2000), Mineralogic and compositional properties of Martian soil and dust: Results from Mars Pathfinder, *J. Geophys. Res. Planets*, *105*(E1), 1721–1755, doi:10.1029/1999JE001060.

Berger, G., M. J. Toplis, E. Treguier, C. D'Uston, and P. Pinet (2009), Evidence in favor of small amounts of ephemeral and transient water during alteration at Meridiani Planum, Mars, *Am. Miner.*, *94*, 1279–1282.

Bethke, C. M. (2008), *Geochemical and Biogeochemical Reaction Modeling*, 2nd ed., Cambridge University Press.

Bibring, J.-P. et al. (2006), Global Mineralogical and Aqueous Mars History Derived from OMEGA/Mars Express Data, *Science*, *312*(5772), 400 –404, doi:10.1126/science.1122659.

Bibring, J.-P. et al. (2007), Coupled Ferric Oxides and Sulfates on the Martian Surface, *Science*, *317*(5842), 1206–1210, doi:10.1126/science.1144174.

Binder, A. B., R. E. Arvidson, E. A. Guinness, K. L. Jones, E. C. Morris, T. A. Mutch, D. C. Pieri, and C. Sagan (1977), The geology of the Viking Lander 1 site, *J. Geophys. Res.*, *82*(28), 4439–4451, doi:10.1029/JS082i028p04439.

Bishop, J. L., and E. Murad (2005), The visible and infrared spectral properties of jarosite and alunite, *Am. Miner.*, *90*(7), 1100–1107, doi:10.2138/am.2005.1700.

Bishop, J. L. et al. (2008a), Phyllosilicate Diversity and Past Aqueous Activity Revealed at Mawrth Vallis, Mars, *Science*, *321*(5890), 830–833, doi:10.1126/science.1159699.

Bishop, J. L., M. D. Lane, M. D. Dyar, and A. J. Brown (2008b), Reflectance and emission spectroscopy study of four groups of phyllosilicates: smectites, kaolinite-serpentines, chlorites and micas, *Clay Miner.*, *43*(1), 35–54, doi:10.1180/claymin.2008.043.1.03.

Bishop, J. L. et al. (2009), Mineralogy of Juventae Chasma: Sulfates in the light-toned mounds, mafic minerals in the bedrock, and hydrated silica and hydroxylated ferric sulfate on the plateau, *J. Geophys. Res.*, *114*, doi:200910.1029/2009JE003352.

Boynton, W. V. et al. (2009), Evidence for Calcium Carbonate at the Mars Phoenix Landing Site, *Science*, *325*(5936), 61–64, doi:10.1126/science.1172768.

Byrne, S. et al. (2009), Distribution of Mid-Latitude Ground Ice on Mars from New Impact Craters, *Science*, *325*(5948), 1674–1676, doi:10.1126/science.1175307.

Cabrol, N. A., and E. A. Grin (1999), Distribution, Classification, and Ages of Martian Impact Crater Lakes, *Icarus*, *142*(1), 160–172, doi:10.1006/icar.1999.6191.

Cabrol, N. A. et al. (2003), Exploring Gusev Crater with Spirit: Review of science objectives and testable hypotheses, *J. Geophys. Res. Planets*, *108*(E12), doi:10.1029/2002JE002026.

Carlson, L., and U. Schwertmann (1980), Natural Occurrence of Feroxyhite (δ′-FeOOH), *Clays Clay Miner.*, *28*(4), 272–280, doi:10.1346/CCMN.1980.0280405.

Carr, M. H. (1976), The Volcanoes of Mars, *Sci. Am.*, *234*(1), 32–43, doi:10.1038/scientificamerican0176-32.

Carr, M. H., and J. W. Head III (2010), Geologic history of Mars, *Earth Planet. Sci. Lett.*, *294*(3–4), 185–203, doi:10.1016/j.epsl.2009.06.042.

Carr, M. H. et al. (1976), Preliminary Results from the Viking Orbiter Imaging Experiment, *Science*, *193*(4255), 766–776, doi:10.1126/science.193.4255.766.

Carr, M. H., R. Greeley, K. R. Blasius, J. E. Guest, and J. B. Murray (1977), Some Martian volcanic features as viewed from the Viking orbiters, *J. Geophys. Res.*, *82*(28), 3985–4015, doi:10.1029/JS082i028p03985.

Carr, M. J., M. D. Feigenson, and E. A. Bennett (1990), Incompatible element and isotopic evidence for tectonic control of source mixing and melt extraction along the Central American arc, *Contrib. Miner. Pet.*, *105*(4), 369–380, doi:10.1007/BF00286825.

Carr, M. J., I. Saginor, G. E. Alvarado, L. L. Bolge, F. N. Lindsay, K. Milidakis, B. D. Turrin, M. D. Feigenson, and C. C. S. Iii (2007), Element fluxes from the volcanic front of Nicaragua and Costa Rica, *Geochem. Geophys. Geosystems*, *8*(6), Q06001, doi:10.1029/2006GC001396.

Carter, J., F. Poulet, J.-P. Bibring, N. Mangold, and S. Murchie (2013), Hydrous minerals on Mars as seen by the CRISM and OMEGA imaging spectrometers: Updated global view, *J. Geophys. Res. Planets*, *118*(4), 831–858, doi:10.1029/2012JE004145.

Che, C., and T. D. Glotch (2012), The effect of high temperatures on the mid-to-far-infrared emission and near-infrared reflectance spectra of phyllosilicates and natural zeolites: Implications for martian exploration, *Icarus*, *218*(1), 585–601.

Chojnacki, M., and B. M. Hynek (2008), Geological context of water-altered minerals in Valles Marineris, Mars, *J. Geophys. Res.*, *113*, doi:200810.1029/2007JE003070.

Christensen, P. R., J. L. Bandfield, V. E. Hamilton, D. A. Howard, M. D. Lane, J. L. Piatek, S. W. Ruff, and W. L. Stefanov (2000a), A thermal emission spectral library of rock-forming minerals, *J. Geophys. Res. Planets*, *105*(E4), 9735–9739, doi:10.1029/1998JE000624.

Christensen, P. R. et al. (2000b), Detection of crystalline hematite mineralization on Mars by the Thermal Emission Spectrometer: Evidence for near-surface water, *J. Geophys. Res.*, *105*(E4), 9623–9642, doi:10.1029/1999JE001093.

Christensen, P. R. et al. (2001), Mars Global Surveyor Thermal Emission Spectrometer experiment: Investigation description and surface science results, *J. Geophys. Res. Planets*, *106*(E10), 23823–23871, doi:10.1029/2000JE001370.

Christensen, P. R. et al. (2003), Morphology and Composition of the Surface of Mars: Mars Odyssey THEMIS Results, *Science*, *300*(5628), 2056–2061, doi:10.1126/science.1080885.

Christensen, P. R., N. S. Gorelick, G. L. Mehall, and K. C. Murray (n.d.), THEMIS Public Data Releases, Planetary Data System node, [online] Available from: http://themis-data.asu.edu

Clark, B. C., A. K. Baird, R. J. Weldon, D. M. Tsusaki, L. Schnabel, and M. P. Candelaria (1982), Chemical composition of Martian fines, *J. Geophys. Res. Solid Earth*, *87*(B12), 10059–10067, doi:10.1029/JB087iB12p10059.

Clark, B. C. et al. (2005), Chemistry and mineralogy of outcrops at Meridiani Planum, *Earth Planet. Sci. Lett.*, *240*(1), 73–94, doi:10.1016/j.epsl.2005.09.040.

Clark, B. C. et al. (2007a), Evidence for montmorillonite or its compositional equivalent in Columbia Hills, Mars, *J. Geophys. Res. Planets*, *112*(E6), doi:10.1029/2006JE002756.

Clark, R. N. (1999), Chapter 1: Spectroscopy of Rocks and Minerals, and Principles of Spectroscopy, in *Manual of Remote Sensing*, vol. 3, Remote Sensing for the Earth Sciences, edited by A. N. Rencz, pp. 3–58, John Wiley and Sons, New York.

Clark, R. N., T. V. V. King, M. Klejwa, G. A. Swayze, and N. Vergo (1990), High spectral resolution reflectance spectroscopy of minerals, *J. Geophys. Res.*, *95*(B8), 12653–12,680, doi:10.1029/JB095iB08p12653.

Clark, R. N., G. A. Swayze, R. Wise, E. Livo, T. Hoefen, R. Kokaly, and S. J. Sutley (2007b), *USGS digital spectral library splib06a*, Digital Data Series, U.S. Geological Survey.

Cloutis, E. A. et al. (2006), Detection and discrimination of sulfate minerals using reflectance spectroscopy, *Icarus*, *184*(1), 121–157, doi:10.1016/j.icarus.2006.04.003.

Costard, F., F. Forget, N. Mangold, D. Mercier, and J. P. Peulvast (2001), Debris Flows on Mars: Analogy with Terrestrial Periglacial Environment and Climatic Implications, vol. 32, p. 1534.

Craddock, R. A., and A. D. Howard (2002), The case for rainfall on a warm, wet early Mars, *J. Geophys. Res. Planets*, *107*(E11), 21–1–21–36, doi:10.1029/2001JE001505.

Daly, T., P. Gavin, and V. Chevrier (2011), Effects of Thermal Alteration on the Near-Infrared and Mid-Infrared Spectra of Martian Phyllosilicates, in *Lunar and Planetary Institute Science Conference Abstracts*, vol. 42, p. 1164.

Dehouck, E., V. Chevrier, A. Gaudin, N. Mangold, P.-E. Mathé, and P. Rochette (2012), Evaluating the role of sulfide-weathering in the formation of sulfates or carbonates on Mars, *Geochim. Cosmochim. Acta*, *90*, 47–63, doi:10.1016/j.gca.2012.04.057.

Dohm, J. M. et al. (2009), New evidence for a magmatic influence on the origin of Valles Marineris, Mars, *J. Volcanol. Geotherm. Res.*, *185*(1–2), 12–27, doi:10.1016/j.jvolgeores.2008.11.029.

Drouet, C., and A. Navrotsky (2003), Synthesis, characterization, and thermochemistry of K-Na-H3O jarosites, *Geochim. Cosmochim. Acta*, *67*(11), 2063–2076, doi:10.1016/S0016-7037(02)01299-1.

Dundas, C. M., and S. Byrne (2010), Modeling sublimation of ice exposed by new impacts in the martian mid-latitudes, *Icarus*, *206*(2), 716–728, doi:10.1016/j.icarus.2009.09.007.

Eberl, D., and J. Hower (1975), Kaolinite synthesis: The role of the Si/A1 and (alkali)/(H+) ratio in hydrothermal systems, *Clays Clay Miner.*, *23*, 301–309.

Ece, Ö. I., P. A. Schroeder, M. J. Smilley, and J. M. Wampler (2008), Acid-sulphate hydrothermal alteration of andesitic tuffs and genesis of halloysite and alunite deposits in the Biga Peninsula, Turkey, *Clay Miner.*, *43*(2), 281–315.

Edwards, C. S., P. R. Christensen, and V. E. Hamilton (2008), Evidence for extensive olivine-rich basalt bedrock outcrops in Ganges and Eos chasmas, Mars, *J. Geophys. Res.*, *113*(E11), E11003, doi:10.1029/2008JE003091.

Ehlmann, B. L. et al. (2009a), Identification of hydrated silicate minerals on Mars using MRO-CRISM: Geologic context near Nili Fossae and implications for aqueous alteration, *J. Geophys. Res.*, *114*(E2), E00D08, doi:10.1029/2009JE003339.

Ehlmann, B. L. et al. (2009b), Identification of hydrated silicate minerals on Mars using MRO-CRISM: Geologic context near Nili Fossae and implications for aqueous alteration, *J Geophys Res*, *114*, 1–33.

Ehlmann, B. L., J. F. Mustard, R. N. Clark, G. A. Swayze, and S. L. Murchie (2011a), Evidence for Low-Grade Metamorphism, Hydrothermal Alteration, and Diagenesis on Mars from Phyllosilicate Mineral Assemblages, *Clays Clay Miner.*, *59*(4), 359–377, doi:10.1346/CCMN.2011.0590402.

Ehlmann, B. L., J. F. Mustard, S. L. Murchie, J.-P. Bibring, A. Meunier, A. A. Fraeman, and Y. Langevin (2011b), Subsurface water and clay mineral formation during the early history of Mars, *Nature*, *479*(7371), 53–60, doi:10.1038/nature10582.

Ehlmann, B. L., D. L. Bish, S. W. Ruff, and J. F. Mustard (2012), Mineralogy and chemistry of altered Icelandic basalts: Application to clay mineral detection and understanding aqueous environments on Mars, *J. Geophys. Res.*, *117*, doi:10.1029/2012JE004156.

Elkins, L. J., T. P. Fischer, D. R. Hilton, Z. D. Sharp, S. McKnight, and J. Walker (2006), Tracing nitrogen in volcanic and geothermal volatiles from the Nicaraguan volcanic front, *Geochim. Cosmochim. Acta*, *70*(20), 5215–5235, doi:10.1016/j.gca.2006.07.024.

Farrand, W. H., T. D. Glotch, J. W. Rice, J. A. Hurowitz, and G. A. Swayze (2009), Discovery of jarosite within the Mawrth Vallis region of Mars: Implications for the geologic history of the region, *Icarus*, *204*(2), 478–488.

Fassett, C. I., and J. W. Head III (2008a), The timing of martian valley network activity: Constraints from buffered crater counting, *Icarus*, *195*(1), 61–89, doi:10.1016/j.icarus.2007.12.009.

Fassett, C. I., and J. W. Head III (2008b), Valley network-fed, open-basin lakes on Mars: Distribution and implications for Noachian surface and subsurface hydrology, *Icarus*, *198*(1), 37–56, doi:10.1016/j.icarus.2008.06.016.

Fernández-Remolar, D. C., R. V. Morris, J. E. Gruener, R. Amils, and A. H. Knoll (2005), The Río Tinto Basin, Spain: Mineralogy, sedimentary geobiology, and implications for

interpretation of outcrop rocks at Meridiani Planum, Mars, *Earth Planet. Sci. Lett.*, *240*(1), 149–167, doi:10.1016/j.epsl.2005.09.043.

Fernández-Remolar, D. C., O. Prieto-Ballesteros, D. Gómez-Ortíz, M. Fernández-Sampedro, P. Sarrazin, M. Gailhanou, and R. Amils (2011), Río Tinto sedimentary mineral assemblages: A terrestrial perspective that suggests some formation pathways of phyllosilicates on Mars, *Icarus*, *211*(1), 114–138, doi:10.1016/j.icarus.2010.09.008.

Fialips, C.-I., S. Petit, A. Decarreau, and D. Beaufort (2000), Influence of synthesis pH on kaolinite "crystallinity" and surface properties, *Clays Clay Miner.*, *48*(2), 173–184.

Flahaut, J., C. Quantin, P. Allemand, P. Thomas, and L. Le Deit (2010), Identification, distribution and possible origins of sulfates in Capri Chasma (Mars), inferred from CRISM data, *J. Geophys. Res. Planets*, *115*(E11), doi:10.1029/2009JE003566.

Flahaut, J., J. F. Mustard, C. Quantin, H. Clenet, P. Allemand, and P. Thomas (2011), Dikes of distinct composition intruded into Noachian-aged crust exposed in the walls of Valles Marineris, *Geophys. Res. Lett.*, *38*(15), doi:10.1029/2011GL048109.

Flahaut, J., C. Quantin, H. Clenet, P. Allemand, J. F. Mustard, and P. Thomas (2012), Pristine Noachian crust and key geologic transitions in the lower walls of Valles Marineris: Insights into early igneous processes on Mars, *Icarus*, *221*(1), 420–435, doi:10.1016/j.icarus.2011.12.027.

Fueten, F., H. Racher, R. Stesky, P. MacKinnon, E. Hauber, P. C. McGuire, T. Zegers, and K. Gwinner (2010), Structural analysis of interior layered deposits in Northern Coprates Chasma, Mars, *Earth Planet. Sci. Lett.*, *294*(3–4), 343–356, doi:10.1016/j.epsl.2009.11.004.

Fueten, F., J. Flahaut, L. Le Deit, R. Stesky, E. Hauber, and K. Gwinner (2011), Interior layered deposits within a perched basin, southern Coprates Chasma, Mars: Evidence for their formation, alteration, and erosion, *J. Geophys. Res. Planets*, *116*(E2), doi:10.1029/2010JE003695.

Gavin, P., and V. Chevrier (2010), Thermal alteration of nontronite and montmorillonite: Implications for the martian surface, *Icarus*, *208*(2), 721–734, doi:10.1016/j.icarus.2010.02.027.

Gellert, R. et al. (2004), Chemistry of Rocks and Soils in Gusev Crater from the Alpha Particle X-ray Spectrometer, *Science*, *305*(5685), 829 –832, doi:10.1126/science.1099913.

Gendrin, A. et al. (2005), Sulfates in Martian Layered Terrains: The OMEGA/Mars Express View, *Science*, *307*(5715), 1587 –1591, doi:10.1126/science.1109087.

Gillespie, A. R., A. B. Kahle, and R. E. Walker (1986), Color enhancement of highly correlated images. I. Decorrelation and HSI contrast stretches, *Remote Sens. Environ.*, *20*(3), 209–235, doi:10.1016/0034-4257(86)90044-1.

Glotch, T. D., and A. D. Rogers (2007), Evidence for aqueous deposition of hematite- and sulfate-rich light-toned layered deposits in Aureum and Iani Chaos, Mars, *J. Geophys. Res. Planets*, *112*(E6), doi:10.1029/2006JE002863.

Glotch, T. D., J. L. Bandfield, P. R. Christensen, W. M. Calvin, S. M. McLennan, B. C. Clark, A. D. Rogers, and S. W. Squyres (2006), Mineralogy of the light-toned outcrop at Meridiani Planum as seen by the Miniature Thermal Emission Spectrometer and implications for its formation, *J. Geophys. Res. Planets*, *111*(E12), doi:10.1029/2005JE002672.

Glotch, T. D., J. L. Bandfield, L. L. Tornabene, H. B. Jensen, and F. P. Seelos (2010), Distribution and formation of chlorides and phyllosilicates in Terra Sirenum, Mars, *Geophys. Res. Lett.*, *37*(16), doi:10.1029/2010GL044557.

Golden, D. C., D. W. Ming, R. V. Morris, and S. A. Mertzman (2005), Laboratory-simulated acid-sulfate weathering of basaltic materials: Implications for formation of sulfates at Meridiani Planum and Gusev crater, Mars, *J. Geophys. Res.*, *110*, doi:200510.1029/2005JE002451.

Golden, D. C., D. W. Ming, R. V. Morris, and T. G. Graff (2008), Hydrothermal synthesis of hematite spherules and jarosite: Implications for diagenesis and hematite spherule formation in sulfate outcrops at Meridiani Planum, Mars, *Am. Miner.*, *93*(8-9), 1201–1214, doi:10.2138/am.2008.2737.

Gough, R. V., V. F. Chevrier, K. J. Baustian, M. E. Wise, and M. A. Tolbert (2011), Laboratory studies of perchlorate phase transitions: Support for metastable aqueous perchlorate solutions on Mars, *Earth Planet. Sci. Lett.*, *312*(3–4), 371–377, doi:10.1016/j.epsl.2011.10.026.

Grotzinger, J. P. et al. (2012), Mars Science Laboratory Mission and Science Investigation, *Space Sci. Rev.*, *170*(1-4), 5–56, doi:10.1007/s11214-012-9892-2.

Grotzinger, J. P. et al. (2013), Mars Science Laboratory: First 100 Sols of Geologic and Geochemical Exploration from Bradbury Landing to Glenelg, *Lpi Contrib.*, *1719*, 1259.

Gulick, V. C. (2001), Origin of the valley networks on Mars: a hydrological perspective, *Geomorphology*, *37*(3–4), 241–268, doi:10.1016/S0169-555X(00)00086-6.

Haberle, R. M. (1998), Early Mars Climate Models, *J. Geophys. Res. Planets*, *103*(E12), 28467–28479, doi:10.1029/98JE01396.

Hamilton, V. E., and P. R. Christensen (2005), Evidence for extensive, olivine-rich bedrock on Mars, *Geology*, *33*(6), 433–436, doi:10.1130/G21258.1.

Hamilton, V. E., R. V. Morris, J. E. Gruener, and S. A. Mertzman (2008), Visible, near-infrared, and middle infrared spectroscopy of altered basaltic tephras: Spectral signatures of phyllosilicates, sulfates, and other aqueous alteration products with application to the

mineralogy of the Columbia Hills of Gusev Crater, Mars, *J. Geophys. Res. Planets*, *113*(E12), doi:10.1029/2007JE003049.

Hecht, M. H. et al. (2009), Detection of Perchlorate and the Soluble Chemistry of Martian Soil at the Phoenix Lander Site, *Science*, *325*(5936), 64–67, doi:10.1126/science.1172466.

Hoch, A. R., M. M. Reddy, and J. I. Drever (1996), The effect of iron content and dissolved O2 on dissolution rates of clinopyroxene at pH 5.8 and 25° C: preliminary results, *Chem. Geol.*, *132*(1-4), 151–156.

Hoefen, T. M., R. N. Clark, J. L. Bandfield, M. D. Smith, J. C. Pearl, and P. R. Christensen (2003), Discovery of Olivine in the Nili Fossae Region of Mars, *Science*, *302*(5645), 627–630, doi:10.1126/science.1089647.

Hoke, M. R. T., and B. M. Hynek (2009), Roaming zones of precipitation on ancient Mars as recorded in valley networks, *J. Geophys. Res. Planets*, *114*(E8), doi:10.1029/2008JE003247.

Hoke, M. R. T., B. M. Hynek, and G. E. Tucker (2011), Formation timescales of large Martian valley networks, *Earth Planet. Sci. Lett.*, *312*(1–2), 1–12, doi:10.1016/j.epsl.2011.09.053.

Howard, A. D., J. M. Moore, and R. P. Irwin (2005), An intense terminal epoch of widespread fluvial activity on early Mars: 1. Valley network incision and associated deposits, *J. Geophys. Res. Planets*, *110*(E12), doi:10.1029/2005JE002459.

Hurowitz, J. A., S. M. McLennan, D. H. Lindsley, and M. A. A. Schoonen (2005), Experimental epithermal alteration of synthetic Los Angeles meteorite: Implications for the origin of Martian soils and identification of hydrothermal sites on Mars, *J. Geophys. Res.*, *110*, doi:200510.1029/2004JE002391.

Hynek, B. M., M. Beach, and M. R. T. Hoke (2010), Updated global map of Martian valley networks and implications for climate and hydrologic processes, *J. Geophys. Res. Planets*, *115*(E9), doi:10.1029/2009JE003548.

Hynek, B. M., T. M. McCollom, and K. L. Rogers (2011), Cerro Negro volcano, Nicaragua: An assessment of geological and potential biological systems on early Mars, *Geol. Soc. Am. Spec. Pap.*, *483*, doi:10.1130/2011.2483.

Hynek, B. M., T. M. McCollom, and K. L. Rogers (2012), Cerro Negro volcano, Nicaragua: An assessment of geological and potential biological systems on early Mars, in *Geological Society of America Special Papers*, vol. 483, pp. 279–285, Geological Society of America.

Hynek, B. M., T. M. McCollom, E. C. Marcucci, K. Brugman, and K. L. Rogers (submitted), Assessing Environmental Controls on Acid-Sulfate Alteration at Active Volcanoes in Nicaragua: Applications to Relic Hydrothermal Systems on Mars, *J. Geophys. Res.*

Irwin, R. P., A. D. Howard, R. A. Craddock, and J. M. Moore (2005), An intense terminal epoch of widespread fluvial activity on early Mars: 2. Increased runoff and paleolake development, *J. Geophys. Res. Planets*, *110*(E12), doi:10.1029/2005JE002460.

Jaeger, W. L., L. P. Keszthelyi, A. S. McEwen, C. M. Dundas, and P. S. Russell (2007), Athabasca Valles, Mars: A Lava-Draped Channel System, *Science*, *317*(5845), 1709–1711, doi:10.1126/science.1143315.

Johnson, J. R., J. F. B. Iii, E. Cloutis, M. Staid, W. H. Farrand, T. McCoy, M. Rice, A. Wang, and A. Yen (2007), Mineralogic constraints on sulfur-rich soils from Pancam spectra at Gusev crater, Mars, *Geophys. Res. Lett.*, *34*(13), L13202, doi:10.1029/2007GL029894.

Johnson, J. W., E. H. Oelkers, and H. C. Helgeson (1992), SUPCRT92: A software package for calculating the standard molal thermodynamic properties of minerals, gases, aqueous species, and reactions from 1 to 5000 bar and 0 to 1000°C, *Comput. Geosci.*, *18*(7), 899–947, doi:10.1016/0098-3004(92)90029-Q.

Jonckbloedt, R. C. L. (1998), Olivine dissolution in sulphuric acid at elevated temperatures—implications for the olivine process, an alternative waste acid neutralizing process, *J. Geochem. Explor.*, *62*(1–3), 337–346, doi:10.1016/S0375-6742(98)00002-8.

Kasting, J. F. (1991), CO2 condensation and the climate of early Mars, *Icarus*, *94*(1), 1–13, doi:10.1016/0019-1035(91)90137-I.

Knauth, L. P., D. M. Burt, and K. H. Wohletz (2005), Impact origin of sediments at the Opportunity landing site on Mars, *Nature*, *438*(7071), 1123–1128, doi:10.1038/nature04383.

Kounaves, S. P. et al. (2010), Soluble sulfate in the martian soil at the Phoenix landing site, *Geophys. Res. Lett.*, *37*(9), doi:10.1029/2010GL042613.

Lamb, M. P., A. D. Howard, W. E. Dietrich, and J. T. Perron (2007), Formation of amphitheater-headed valleys by waterfall erosion after large-scale slumping on Hawai ‘i, *Geol. Soc. Am. Bull.*, *119*(7-8), 805–822.

Lane, M. D., J. L. Bishop, M. D. Dyar, P. L. King, M. Parente, and B. C. Hyde (2008), Mineralogy of the Paso Robles soils on Mars, *Am. Miner.*, *93*(5-6), 728–739, doi:10.2138/am.2008.2757.

Lanz, J. K., and M. B. Saric (2009), Cone fields in SW Elysium Planitia: Hydrothermal venting on Mars?, *J. Geophys. Res. Planets*, *114*(E2), doi:10.1029/2008JE003209.

Leverington, D. W. (2004), Volcanic rilles, streamlined islands, and the origin of outflow channels on Mars, *J. Geophys. Res. Planets*, *109*(E10), doi:10.1029/2004JE002311.

Levy, J., J. Head, and D. Marchant (2009), Thermal contraction crack polygons on Mars: Classification, distribution, and climate implications from HiRISE observations, *J. Geophys. Res. Planets*, *114*(E1), doi:10.1029/2008JE003273.

Lichtenberg, K. A. et al. (2010), Stratigraphy of hydrated sulfates in the sedimentary deposits of Aram Chaos, Mars, *J. Geophys. Res.*, *115*, E00D17, doi:10.1029/2009JE003353.

Lodders, K. (1998), A survey of shergottite, nakhlite and chassigny meteorites whole-rock compositions, *Meteorit. Planet. Sci.*, *33*(S4), A183–A190, doi:10.1111/j.1945-5100.1998.tb01331.x.

Lucchitta, B. K., N. K. Isbell, and A. Howington-Kraus (1994), Topography of Valles Marineris: Implications for erosional and structural history, *J. Geophys. Res. Planets*, *99*(E2), 3783–3798, doi:10.1029/93JE03095.

Malin (2010), An overview of the 1985-2006 Mars Orbiter Camera science investigation, *Mars J.*, *5*, 1–60, doi:10.1555/mars.2010.0001.

Malin, M. C., and M. H. Carr (1999), Groundwater formation of martian valleys, *Nature*, *397*(6720), 589–591, doi:10.1038/17551.

Malin, M. C., and K. S. Edgett (2000), Evidence for Recent Groundwater Seepage and Surface Runoff on Mars, *Science*, *288*(5475), 2330–2335, doi:10.1126/science.288.5475.2330.

Malin, M. C., and K. S. Edgett (2001), Mars Global Surveyor Mars Orbiter Camera: Interplanetary cruise through primary mission, *J. Geophys. Res. Planets*, *106*(E10), 23429–23570, doi:10.1029/2000JE001455.

Malin, M. C., and K. S. Edgett (2003), Evidence for Persistent Flow and Aqueous Sedimentation on Early Mars, *Science*, *302*(5652), 1931–1934, doi:10.1126/science.1090544.

Malin, M. C., K. S. Edgett, L. V. Posiolova, S. M. McColley, and E. Z. N. Dobrea (2006), Present-Day Impact Cratering Rate and Contemporary Gully Activity on Mars, *Science*, *314*(5805), 1573–1577, doi:10.1126/science.1135156.

Malin, M. C. et al. (2007), Context Camera Investigation on board the Mars Reconnaissance Orbiter, *J. Geophys. Res. Planets*, *112*(E5), doi:10.1029/2006JE002808.

Manara, A., and G. Trinchieri (2011), Schiaparelli and his legacy, *Mem. Della Soc. Astron. Ital.*, *82*, 209.

Mangold, N., L. Roach, R. Milliken, S. Le Mouélic, V. Ansan, J. P. Bibring, P. Masson, J. F. Mustard, S. Murchie, and G. Neukum (2010), A Late Amazonian alteration layer related to local volcanism on Mars, *Icarus*, *207*(1), 265–276, doi:10.1016/j.icarus.2009.10.015.

Mangold, N. et al. (2013), Chemcam Analysis of Conglomerates at Bradbury Site, Mars, *Lpi Contrib.*, *1719*, 1267.

Marcucci, E. C., B. M. Hynek, T. M. McCollom, and K. L. Rogers (2010), Acid-Sulfate Weathering of Basalts at Cerro Negro Volcano, Nicaragua: An Early Mars Analog, in *Lunar and Planetary Institute Science Conference Abstracts*, vol. 41, p. 2167.

Marcucci, E. C. and B. M. Hynek (submitted), Laboratory simulations of acid-sulfate weathering in volcanic hydrothermal conditions: Implications for early Mars, *J. Geophys. Res.*

Marcucci, E. C., B. M. Hynek, K. S. Kierein-Young, and K. L. Rogers (submitted) Visible-near infrared spectroscopy of volcanic acid-sulfate alteration in Nicaragua: Analogs for early Mars, *J. Geophys. Res.*

Masursky, H. (1973), An overview of geological results from Mariner 9, *J. Geophys. Res.*, *78*(20), 4009–4030, doi:10.1029/JB078i020p04009.

McAdam, A., M. Zolotov, T. Sharp, and L. Leshin (2008), Preferential low-pH dissolution of pyroxene in plagioclase–pyroxene mixtures: Implications for martian surface materials, *Icarus*, *196*(1), 90–96, doi:10.1016/j.icarus.2008.01.008.

McCollom, T. M., and B. M. Hynek (2005), A volcanic environment for bedrock diagenesis at Meridiani Planum on Mars, *Nature*, *438*(7071), 1129–1131, doi:10.1038/nature04390.

McCollom, T. M., and J. S. Seewald (2001), A reassessment of the potential for reduction of dissolved CO2 to hydrocarbons during serpentinization of olivine, *Geochim. Cosmochim. Acta*, *65*(21), 3769–3778.

McCollom, T. M., E. Marcucci, and B. M. Hynek (2010), Combined Experimental and Theoretical Study of Acid-Sulfate Alteration of Basalt for Interpretation of Sulfate-rich Deposits on Mars, *Lunar Planet. Inst. Sci. Conf. Abstr.*, *41*, 1380.

McCollom, T. M., M. Robbins, B. Moskowitz, T. S. Berquó, N. Jöns, and B. M. Hynek (2013), Experimental Study of Acid-sulfate Alteration of Basalt and Implications for Sulfate Deposits on Mars, *J. Geophys. Res. Planets*, doi:10.1002/jgre.20044.

McCollom, T. M., B. M. Hynek, K. L. Rogers, B. Moskowitz, and T.S. Berquó (submitted), Chemical and Mineralogical Trends During Acid-Sulfate Alteration of Pyroclastic Basalt at Cerro Negro Volcano, and Implications for Early Mars, *J. Geophys. Res.*

McDowell, M. L., and V. E. Hamilton (2009), Seeking phyllosilicates in thermal infrared data: A laboratory and Martian data case study, *J. Geophys. Res. Planets*, *114*(E6), doi:10.1029/2008JE003317.

McEwen, A. S., M. C. Malin, M. H. Carr, and W. K. Hartmann (1999), Voluminous volcanism on early Mars revealed in Valles Marineris, *Nature*, *397*(6720), 584–586, doi:10.1038/17539.

McEwen, A. S. et al. (2007), Mars Reconnaissance Orbiter's High Resolution Imaging Science Experiment (HiRISE), *J. Geophys. Res. Planets*, *112*(E5), doi:10.1029/2005JE002605.

McEwen, A. S., L. Ojha, C. M. Dundas, S. S. Mattson, S. Byrne, J. J. Wray, S. C. Cull, S. L. Murchie, N. Thomas, and V. C. Gulick (2011), Seasonal Flows on Warm Martian Slopes, *Science*, *333*(6043), 740–743, doi:10.1126/science.1204816.

McLennan, S. M. et al. (2005), Provenance and diagenesis of the evaporite-bearing Burns formation, Meridiani Planum, Mars, *Earth Planet. Sci. Lett.*, *240*(1), 95–121, doi:10.1016/j.epsl.2005.09.041.

Mellon, M. T., and R. J. Phillips (2001), Recent gullies on Mars and the source of liquid water, *J. Geophys. Res. Planets*, *106*(E10), 23165–23179, doi:10.1029/2000JE001424.

Mellon, M. T. et al. (2009), Ground ice at the Phoenix Landing Site: Stability state and origin, *J. Geophys. Res. Planets*, *114*(E1), doi:10.1029/2009JE003417.

Milliken, R. E. et al. (2008), Opaline silica in young deposits on Mars, *Geology*, *36*(11), 847–850, doi:10.1130/G24967A.1.

Milliken, R. E., J. P. Grotzinger, and B. J. Thomson (2010), Paleoclimate of Mars as captured by the stratigraphic record in Gale Crater, *Geophys. Res. Lett.*, *37*(4), doi:10.1029/2009GL041870.

Ming, D. W. et al. (2006), Geochemical and mineralogical indicators for aqueous processes in the Columbia Hills of Gusev crater, Mars, *J. Geophys. Res. Planets*, *111*(E2), doi:10.1029/2005JE002560.

Moore, J. M., and A. D. Howard (2005), Large alluvial fans on Mars, *J. Geophys. Res. Planets*, *110*(E4), doi:10.1029/2004JE002352.

Morris, R. V., H. V. Lauer, Jr., C. A. Lawson, E. K. Gibson, Jr., G. A. Nace, and C. Stewart (1985), Spectral and other physicochemical properties of submicron powders of hematite (α-Fe2O3), maghemite (γ-Fe2O3), magnetite (Fe3O4), goethite (α-FeOOH), and lepidocrocite (γ-FeOOH), *J. Geophys. Res.*, *90*(B4), 3126–3144, doi:10.1029/JB090iB04p03126.

Morrison, D. A., L. D. Ashwal, W. C. Phinney, C.-Y. Shih, and J. L. Wooden (1983), Pre-Keweenawan anorthosite inclusions in the Keweenawan Beaver Bay and Duluth Complexes, northeastern Minnesota, *Geol. Soc. Am. Bull.*, *94*(2), 206–221, doi:10.1130/0016-7606(1983)94<206:PAIITK>2.0.CO;2.

Murchie, S. L. et al. (2009a), A synthesis of Martian aqueous mineralogy after 1 Mars year of observations from the Mars Reconnaissance Orbiter, *J. Geophys. Res. Planets*, *114*(E2), doi:10.1029/2009JE003342.

Murchie, S. L. et al. (2009b), Compact Reconnaissance Imaging Spectrometer for Mars investigation and data set from the Mars Reconnaissance Orbiter's primary science phase, *J Geophys Res*, *114*.

Mustard, J. F. et al. (2008), Hydrated silicate minerals on Mars observed by the Mars Reconnaissance Orbiter CRISM instrument, *Nature*, *454*(7202), 305–309, doi:10.1038/nature07097.

Mutch, T. A., R. E. Arvidson, A. B. Binder, E. A. Guinness, and E. C. Morris (1977), The geology of the Viking Lander 2 site, *J. Geophys. Res.*, *82*(28), 4452–4467, doi:10.1029/JS082i028p04452.

Nedell, S. S., S. W. Squyres, and D. W. Andersen (1987), Origin and evolution of the layered deposits in the Valles Marineris, Mars, *Icarus*, *70*(3), 409–441, doi:10.1016/0019-1035(87)90086-8.

Niles, P. B., and J. Michalski (2009), Meridiani Planum sediments on Mars formed through weathering in massive ice deposits, *Nat. Geosci.*, *2*(3), 215–220, doi:10.1038/ngeo438.

Nisbet, E. G., and N. H. Sleep (2001), The habitat and nature of early life, *Nature*, *409*(6823), 1083–1091, doi:10.1038/35059210.

Ori, G. G., and C. Mosangini (1998), Complex depositional systems in Hydraotes Chaos, Mars: An example of sedimentary process interactions in the Martian hydrological cycle, *J. Geophys. Res. Planets*, *103*(E10), 22713–22723, doi:10.1029/98JE01969.

Ori, G. G., L. Marinangeli, and A. Baliva (2000), Terraces and Gilbert-type deltas in crater lakes in Ismenius Lacus and Memnonia (Mars), *J. Geophys. Res. Planets*, *105*(E7), 17629–17641, doi:10.1029/1999JE001219.

Osterloo, M. M., V. E. Hamilton, J. L. Bandfield, T. D. Glotch, A. M. Baldridge, P. R. Christensen, L. L. Tornabene, and F. S. Anderson (2008), Chloride-Bearing Materials in the Southern Highlands of Mars, *Science*, *319*(5870), 1651–1654, doi:10.1126/science.1150690.

Palucis, M. C., W. E. Dietrich, A. G. Hayes, R. M. E. Williams, F. Calef, D. Y. Sumner, S. Gupta, C. J. Hardgrove, and M. S. L. Team (2013), Origin and Evolution of the Peace Vallis Fan System that Drains into the Curiosity Landing Area, Gale Crater, *Lpi Contrib.*, *1719*, 1607.

Parker, T. J., D. S. Gorsline, R. S. Saunders, D. C. Pieri, and D. M. Schneeberger (1993), Coastal geomorphology of the Martian northern plains, *J. Geophys. Res. Planets*, *98*(E6), 11061–11078, doi:10.1029/93JE00618.

Patino, L. C., M. J. Carr, and M. D. Feigenson (2000), Local and regional variations in Central American arc lavas controlled by variations in subducted sediment input, *Contrib. Miner. Pet.*, *138*(3), 265–283, doi:10.1007/s004100050562.

PDS Geosciences Node, and CRISM Spectral Library Working Group (n.d.), *CRISM Spectral Library*, Washington University in St. Louis.

Pelkey, S. M. et al. (2007), CRISM multispectral summary products: Parameterizing mineral diversity on Mars from reflectance, *J. Geophys. Res. Planets*, *112*(E8), doi:10.1029/2006JE002831.

Phillips, R. J. et al. (2001), Ancient Geodynamics and Global-Scale Hydrology on Mars, *Science*, *291*(5513), 2587–2591, doi:10.1126/science.1058701.

Poulet, F., and S. Erard (2004), Nonlinear spectral mixing: Quantitative analysis of laboratory mineral mixtures, *J. Geophys. Res. Planets*, *109*(E2), doi:10.1029/2003JE002179.

Poulet, F. et al. (2005), Phyllosilicates on Mars and implications for early martian climate, *Nature*, *438*(7068), 623–627, doi:10.1038/nature04274.

Poulet, F., C. Gomez, J.-P. Bibring, Y. Langevin, B. Gondet, P. Pinet, G. Belluci, and J. Mustard (2007), Martian surface mineralogy from Observatoire pour la Minéralogie, l'Eau, les Glaces et l'Activité on board the Mars Express spacecraft (OMEGA/MEx): Global mineral maps, *J. Geophys. Res. Planets*, *112*(E8), doi:10.1029/2006JE002840.

Poulet, F., N. Mangold, D. Loizeau, J.-P. Bibring, Y. Langevin, J. Michalski, and B. Gondet (2008a), Abundance of minerals in the phyllosilicate-rich units on Mars, *Astron. Astrophys.*, *487*(2), L41–L44, doi:10.1051/0004-6361:200810150.

Poulet, F., R. E. Arvidson, C. Gomez, R. V. Morris, J.-P. Bibring, Y. Langevin, B. Gondet, and J. Griffes (2008b), Mineralogy of Terra Meridiani and western Arabia Terra from OMEGA/MEx and implications for their formation, *Icarus*, *195*(1), 106–130, doi:10.1016/j.icarus.2007.11.031.

Rieder, R. et al. (2004), Chemistry of Rocks and Soils at Meridiani Planum from the Alpha Particle X-ray Spectrometer, *Science*, *306*(5702), 1746 –1749, doi:10.1126/science.1104358.

Roach, L. H., J. F. Mustard, M. D. Lane, J. L. Bishop, and S. L. Murchie (2010a), Diagenetic haematite and sulfate assemblages in Valles Marineris, *Icarus*, *207*(2), 659–674, doi:10.1016/j.icarus.2009.11.029.

Roach, L. H., J. F. Mustard, G. Swayze, R. E. Milliken, J. L. Bishop, S. L. Murchie, and K. Lichtenberg (2010b), Hydrated mineral stratigraphy of Ius Chasma, Valles Marineris, *Icarus*, *206*(1), 253–268, doi:10.1016/j.icarus.2009.09.003.

Robbins, S. J., G. D. Achille, and B. M. Hynek (2011), The volcanic history of Mars: High-resolution crater-based studies of the calderas of 20 volcanoes, *Icarus*, *211*(2), 1179–1203, doi:10.1016/j.icarus.2010.11.012.

Rogers, K. L., B. M. Hynek, and T. M. McCollom (2011), Photosynthesis within Mars' volcanic craters?: Insights from Cerro Negro Volcano, Nicaragua, *Agu Fall Meet. Abstr.*, *33*, 1768.

Roggensack, K., R. L. Hervig, S. B. McKnight, and S. N. Williams (1997), Explosive Basaltic Volcanism from Cerro Negro Volcano: Influence of Volatiles on Eruptive Style, *Science*, *277*(5332), 1639 –1642, doi:10.1126/science.277.5332.1639.

Ruesch, O., F. Poulet, M. Vincendon, J.-P. Bibring, J. Carter, G. Erkeling, B. Gondet, H. Hiesinger, A. Ody, and D. Reiss (2012), Compositional investigation of the proposed

chloride-bearing materials on Mars using near-infrared orbital data from OMEGA/MEx, *J. Geophys. Res. Planets*, *117*(E11), doi:10.1029/2012JE004108.

Ruff, S. W. et al. (2011), Characteristics, distribution, origin, and significance of opaline silica observed by the Spirit rover in Gusev crater, Mars, *J. Geophys. Res.*, *116*, doi:201110.1029/2010JE003767.

Schiffman, P., R. Zierenberg, N. Marks, J. L. Bishop, and M. D. Dyar (2006), Acid-fog deposition at Kilauea volcano: A possible mechanism for the formation of siliceous-sulfate rock coatings on Mars, *Geology*, *34*(11), 921–924, doi:10.1130/G22620A.1.

Schmidt, M. E. et al. (2009), Spectral, mineralogical, and geochemical variations across Home Plate, Gusev Crater, Mars indicate high and low temperature alteration, *Earth Planet. Sci. Lett.*, *281*(3–4), 258–266, doi:10.1016/j.epsl.2009.02.030.

Seelos, K. D., R. E. Arvidson, B. L. Jolliff, S. M. Chemtob, R. V. Morris, D. W. Ming, and G. A. Swayze (2010), Silica in a Mars analog environment: Ka'u Desert, Kilauea Volcano, Hawaii, *J. Geophys. Res. Planets*, *115*(E4), doi:10.1029/2009JE003347.

Skok, J. R., J. F. Mustard, B. L. Ehlmann, R. E. Milliken, and S. L. Murchie (2010), Silica deposits in the Nili Patera caldera on the Syrtis Major volcanic complex on Mars, *Nat. Geosci.*, *advance online publication*, doi:10.1038/ngeo990.

Smith, D. E. et al. (2001), Mars Orbiter Laser Altimeter: Experiment summary after the first year of global mapping of Mars, *J. Geophys. Res. Planets*, *106*(E10), 23689–23722, doi:10.1029/2000JE001364.

Smith, P. H. et al. (2009), H2O at the Phoenix Landing Site, *Science*, *325*(5936), 58–61, doi:10.1126/science.1172339.

Squyres, S. W. et al. (2004), In Situ Evidence for an Ancient Aqueous Environment at Meridiani Planum, Mars, *Science*, *306*(5702), 1709 –1714, doi:10.1126/science.1104559.

Squyres, S. W. et al. (2006a), Rocks of the Columbia Hills, *J. Geophys. Res. Planets*, *111*(E2), doi:10.1029/2005JE002562.

Squyres, S. W. et al. (2006b), Two Years at Meridiani Planum: Results from the Opportunity Rover, *Science*, *313*(5792), 1403 –1407, doi:10.1126/science.1130890.

Squyres, S. W. et al. (2007), Pyroclastic Activity at Home Plate in Gusev Crater, Mars, *Science*, *316*(5825), 738–742, doi:10.1126/science.1139045.

Squyres, S. W. et al. (2008), Detection of Silica-Rich Deposits on Mars, *Science*, *320*(5879), 1063 –1067, doi:10.1126/science.1155429.

Steefel, C. I., and P. Van Cappellen (1990), A new kinetic approach to modeling water-rock interaction: The role of nucleation, precursors, and Ostwald ripening, *Geochim. Cosmochim. Acta*, *54*(10), 2657–2677, doi:10.1016/0016-7037(90)90003-4.

Steiger, M., K. Linnow, H. Juling, G. Gülker, A. E. Jarad, S. Brüggerhoff, and D. Kirchner (2008), Hydration of MgSO4·H2O and Generation of Stress in Porous Materials, *Cryst. Growth Des.*, *8*(1), 336–343, doi:10.1021/cg060688c.

Swayze, G. A. et al. (2008), Discovery of the Acid-Sulfate Mineral Alunite in Terra Sirenum, Mars, Using MRO CRISM: Possible Evidence for Acid-Saline Lacustrine Deposits?, *Agu Fall Meet. Abstr.*

Tanaka, K. L. (1997), Sedimentary history and mass flow structures of Chryse and Acidalia Planitiae, Mars, *J. Geophys. Res. Planets*, *102*(E2), 4131–4149, doi:10.1029/96JE02862.

Thollot, P., N. Mangold, V. Ansan, S. Le Mouélic, R. E. Milliken, J. L. Bishop, C. M. Weitz, L. H. Roach, J. F. Mustard, and S. L. Murchie (2012), Most Mars minerals in a nutshell: Various alteration phases formed in a single environment in Noctis Labyrinthus, *J. Geophys. Res. Planets*, *117*(E4), doi:10.1029/2011JE004028.

Tiercelin, J.-J. et al. (1993), Hydrothermal vents in Lake Tanganyika, East African, Rift system, *Geology*, *21*, 499, doi:10.1130/0091-7613(1993)021<0499:HVILTE>2.3.CO;2.

Tosca, N. J., and A. H. Knoll (2009), Juvenile chemical sediments and the long term persistence of water at the surface of Mars, *Earth Planet. Sci. Lett.*, *286*(3–4), 379–386, doi:10.1016/j.epsl.2009.07.004.

Tosca, N. J., S. M. McLennan, D. H. Lindsley, and M. A. A. Schoonen (2004), Acid-sulfate weathering of synthetic Martian basalt: The acid fog model revisited, *J. Geophys. Res.*, *109*(E5), doi:10.1029/2003JE002218.

Tosca, N. J., S. M. McLennan, B. C. Clark, J. P. Grotzinger, J. A. Hurowitz, A. H. Knoll, C. Schröder, and S. W. Squyres (2005), Geochemical modeling of evaporation processes on Mars: Insight from the sedimentary record at Meridiani Planum, *Earth Planet. Sci. Lett.*, *240*(1), 122–148, doi:10.1016/j.epsl.2005.09.042.

Toulmin, P., A. K. Baird, B. C. Clark, K. Keil, H. J. Rose, R. P. Christian, P. H. Evans, and W. C. Kelliher (1977), Geochemical and mineralogical interpretation of the Viking inorganic chemical results, *J. Geophys. Res.*, *82*(28), 4625–4634, doi:10.1029/JS082i028p04625.

Treiman, A. H. (2003), Geologic settings of Martian gullies: Implications for their origins, *J. Geophys. Res. Planets*, *108*(E4), doi:10.1029/2002JE001900.

Walker, J. A., and M. J. Carr (1986), Compositional variations caused by phenocryst sorting at Cerro Negro volcano, Nicaragua, *Geol. Soc. Am. Bull.*, *97*(9), 1156 –1162, doi:10.1130/0016-7606(1986)97<1156:CVCBPS>2.0.CO;2.

Wang, A. et al. (2006), Evidence of phyllosilicates in Wooly Patch, an altered rock encountered at West Spur, Columbia Hills, by the Spirit rover in Gusev crater, Mars, *J. Geophys. Res. Planets*, *111*(E2), doi:10.1029/2005JE002516.

Weitz, C. M., J. L. Bishop, P. Thollot, N. Mangold, and L. H. Roach (2011), Diverse mineralogies in two troughs of Noctis Labyrinthus, Mars, *Geology*, *39*(10), 899–902, doi:10.1130/G32045.1.

Werner, S. C., S. van Gasselt, and G. Neukum (2003), Continual geological activity in Athabasca Valles, Mars, *J. Geophys. Res. Planets*, *108*(E12), doi:10.1029/2002JE002020.

Wetherill, G. W. (1975), Late heavy bombardment of the moon and terrestrial planets, vol. 6, pp. 1539–1561.

Williams, R. M. E. et al. (2013), Curiosity's Mastcam Images Reveal Conglomerate Outcrops with Water-Transported Pebbles, *Lpi Contrib.*, *1719*, 1617.

Wiseman, S. M. et al. (2008), Phyllosilicate and sulfate-hematite deposits within Miyamoto crater in southern Sinus Meridiani, Mars, *Geophys. Res. Lett.*, *35*(19), doi:10.1029/2008GL035363.

Witbeck, N. E., K. L. Tanaka, and D. H. Scott (1991), Geologic map of the Valles Marineris region, Mars,

Wood, L. J. (2006), Quantitative geomorphology of the Mars Eberswalde delta, *Geol. Soc. Am. Bull.*, *118*(5-6), 557–566, doi:10.1130/B25822.1.

Wray, J. J. (2013), Gale crater: the Mars Science Laboratory/Curiosity Rover Landing Site, *Int. J. Astrobiol.*, *12*(01), 25–38, doi:10.1017/S1473550412000328.

Wray, J. J., S. L. Murchie, S. W. Squyres, F. P. Seelos, and L. L. Tornabene (2009a), Diverse aqueous environments on ancient Mars revealed in the southern highlands, *Geology*, *37*(11), 1043–1046, doi:10.1130/G30331A.1.

Wray, J. J., E. Z. N. Dobrea, R. E. Arvidson, S. M. Wiseman, S. W. Squyres, A. S. McEwen, J. F. Mustard, and S. L. Murchie (2009b), Phyllosilicates and sulfates at Endeavour Crater, Meridiani Planum, Mars, *Geophys. Res. Lett.*, *36*(21), L21201, doi:10.1029/2009GL040734.

Wray, J. J., S. W. Squyres, L. H. Roach, J. L. Bishop, J. F. Mustard, and E. Z. Noe Dobrea (2010), Identification of the Ca-sulfate bassanite in Mawrth Vallis, Mars, *Icarus*, *209*(2), 416–421, doi:16/j.icarus.2010.06.001.

Wray, J. J. et al. (2011), Columbus crater and other possible groundwater-fed paleolakes of Terra Sirenum, Mars, *J. Geophys. Res. Planets*, *116*(E1), doi:10.1029/2010JE003694.

Yen, A. S. et al. (2008), Hydrothermal processes at Gusev Crater: An evaluation of Paso Robles class soils, *J. Geophys. Res. Planets*, *113*(E6), doi:10.1029/2007JE002978.

Zolotov, M. Y., and M. V. Mironenko (2007), Timing of acid weathering on Mars: A kinetic-thermodynamic assessment, *J. Geophys. Res.*, *112*, doi:200710.1029/2006JE002882.

Appendix A – Supplemental Geochemical Data for Chapter 3

Table A1. Model Percent Reaction Progress Represented in Experiments[1]

	Plagioclase	Pyroxene	Olivine	CN 99 cinders
65°C				
1:1	20	10	10	30
4:1	30	20	30	40
10:1	60	30	70	60
150°C				
4:1	50	10	30	n/a
200°C				
4:1	70	50	30	n/a

[1]Reaction progress is judged by comparing the actual, experimental sulfate depletion from precipitation of sulfate minerals with the predicted model depletion. For olivine, because sulfate minerals do not form, the accumulation of Mg^{2+} from dissolution was compared, since it is a conservative mineral.

Table A2. Mineralogy Results from Parameter Variation

	Plagioclase	Pyroxene	Olivine	CN 99 cinders
Fluid:rock ratio				
Size	Slightly bigger with greater ratio	Longer with greater ratio	--	--
Form	--	Changes in Mg-sulfate shape	--	Different gel
Abundance	Decrease with greater ratio	Increase with greater ratio	--	More gel with greater ratio
Duration				
Size	Increased with duration	Increased with duration	--	Increased with duration
Form	Changes in Ca-sulfate shape	Changes in Ca-sulfate shape	More defined	--
Abundance	Increased with duration	Increased with duration	--	--
Temperature				
Size	~ Same	Thicker Ca-sulfate at lower temperature	--	n/a
Form	--	Changes in Ca-sulfate shape	Purple coloring (reduction)	n/a
Abundance	Increased with temperature	~ Same	--	n/a

Table A3. Experimental Fluid Speciation for Pyroxene and Olivine experiments sampled after 12 days for fluid:rock weight 4:1, and 65°C[1]

	Pyroxene	Olivine
pH	0.157	3.325
HSO4-	836.7	6.24
Ca++	42.04	0.8592
Mg++	37.37	156.0
SO4--	25.96	171.8
Fe++	29.12	17.11
MgSO4(aq)	26.29	884
SiO2(aq)	5.597	3.696
CaSO4(aq)	5.352	0.9148
Al+++	5.887	--
Na+	3.25	0.235
K+	0.3439	--
Mn++	0.6169	0.4843
MnSO4(aq)	0.1631	1.071
KHSO4(aq)	0.01275	--
KSO4-	0.01032	--

[1]Units in mmolality

Table A4. Experimental Fluid Speciation for Plagioclase and Cerro Negro 99 cinders experiments sampled after 12 days from fluid:rock weight 4:1, and 65°C[1]

	Plagioclase	Cerro Negro 99 cinders
pH	3.016	3.054
SO4--	723.1	456.3
Al+++	439.1	258.4
SiO2(aq)	18.12	4.476
Na+	72.71	2.706
HSO4-	27.18	17.93
AlOH++	31.92	19.2
CaSO4(aq)	10.77	8.147
MgSO4(aq)	5.931	176.2
Fe++	4.63	33.53
Ca++	4.206	4.883
Mg++	0.3818	17.84
Al(OH)2+	0.1473	0.09965
MnSO4(aq)	0.07492	1.093
Mn++	0.01408	0.3156

[1]Units in mmolality

Table A5. Mineral Saturation Indices[1] for Pyroxene and Olivine (corresponding to Table A3)

	Pyroxene	**Olivine**
Quartz	1.1506	0.9704
Tridymite	0.9995	0.8193
Chalcedony	0.9116	0.7313
Cristobalite(alpha)	0.6782	0.4980
Coesite	0.4302	0.2500
Cristobalite(beta)	0.3223	0.1421
Anhydrite	0.2663	-0.5009
SiO_2(am)	0.1103	-0.0699
Gypsum	0.0733	-0.6939
Bassanite	-0.3778	-1.1450
Hexahydrite	-2.4579	-0.9312
Epsomite	-2.5308	-1.0041
Kieserite	-2.9258	-1.3992

[1]Saturation index (SI) is defined as the log(Q/K), where Q is the activity product of the fluid and K is the equilibrium constant for a given mineral reaction. SI = 0 means the fluid and solids products are in equilibrium; SI = negative means the fluid is undersaturated; SI = positive means the fluid is supersaturated.

Table A6. Mineral Saturation Indices[1] for Plagioclase and Cerro Negro 99 cinders (corresponding to Table A4)

	Plagioclase	Cerro Negro 99 cinders
Natroalunite	13.0746	10.6907
Pyrophyllite	10.2508	7.4805
Beidellite-H	10.2028	7.5765
Beidellite-Ca	9.9075	7.2977
Beidellite-Mg	9.8640	7.5172
Beidellite-Na	9.7936	6.6954
Montmorillonite-Mg	6.8592	4.9974
Montmorillonite-Ca	6.8042	4.7206
Paragonite	7.7609	3.997
Montmorillonite-Na	6.8730	4.1772
Kaolinite	8.2026	6.6468
Mordenite	5.1124	1.3918
Mesolite	3.3944	0.3256
Albite	2.6976	-0.725
Albite_low	2.6976	-0.725
Laumontite	1.7321	-0.9387
Albite_high	1.6072	-1.8154
Scolecite	1.6099	-0.4536
Kyanite	2.6641	1.7156
Andalusite	2.4830	1.5345
Sillimanite	2.1863	1.2377
Diaspore	2.7266	2.5560
Quartz	1.6608	1.0536
Analcime	1.0278	-1.7478
Tridymite	1.5097	0.9024
Boehmite	2.3848	2.2142
Chalcedony	1.4218	0.8145
Corundum	2.4279	2.0866
Cristobalite(alpha)	1.1884	0.5811
Gibbsite	2.0028	1.8322
Coesite	0.9404	0.3331
Cristobalite(beta)	0.8325	0.2253
SiO_2(am)	0.6205	0.0132
Anhydrite	0.5701	0.4488
Gypsum	0.3772	0.2558
Bassanite	-0.0740	-0.1953
Margarite	-0.1271	-1.9246
Jadeite	-0.5961	--
Natrolite	-0.9250	--
Wairakite	-1.5533	--
Lawsonite	-2.2401	--
Hexahydrite	--	-1.6318
Epsomite	--	-1.7047
Kieserite	--	-2.0997
Hercynite	--	-2.8465

[1]See footnote of Table A5